Analysis of Multidimensional Phase Space Hamiltonian Dynamics: Methods and Applications

A Thesis
Presented to
The Academic Faculty

by

Elena Y. Shchekinova

In Partial Fulfillment
of the Requirements for the Degree
Doctor of Philosophy

School of Physics
Georgia Institute of Technology
May 2006

Analysis of Multidimensional Phase Space Hamiltonian Dynamics: Methods and Applications

Approved by:

Dr. Turgay Uzer, Advisor
School of Physics
Georgia Institute of Technology

Dr. John Wood
School of Physics
Georgia Institute of Technology

Dr. Kurt Wiesenfeld,
School of Physics
Georgia Institute of Technology

Dr. Mustafa M. Aral
School of Civil Engineering
Georgia Institute of Technology

Dr. Ray Flannery
School of Physics
Georgia Institute of Technology

Date Approved: 15^{th} March 2006

To my daughter and my parents

ACKNOWLEDGEMENTS

I would like to thank my parents. Their enormous help and constant support allowed me to advance in my work and to bring it to its completion.

I am very grateful to my advisor, Tugay Uzer, who initiated our collaboration and introduced me to the original ideas of research presented in this thesis. For almost four years of our joined work he always helped to advance my research in the right direction. I greatly benefited from his broad scientific culture, and I would like to thank him for taking the time to discuss with me some of the problems that I encountered.

Part of this work was developed in collaboration with Cristel Chandre, whom I would like to thank for many stimulating discussions and his constructive criticism that helped me to improve substantially the quality of my work. Our collaboration provoked many interesting ideas that are at the basis of this work.

I also spent several memorable years at the Center of Nonlinear Science and would like to specially thank the leader of the Center, Predrag Cvitanović, for creating a friendly and stimulating scientific atmosphere and for providing me and other students with all the facilities of the Center. He made our work here an enjoyable experience.

I would like to acknowledge Andrew Zangwill, who, as a graduate coordinator, inexhaustibly assisted me with all the problems and questions. Like many of his students I greatly benefited from his unforgettable class of Elecromagnetism, which provided a very good background for my preparation for the comprehensive examination.

My warmest thanks goes to Helmut Biriz, the former graduate coordinator, for giving me this wonderful opportunity to join the School of Physics the starting point when I turned from math to physics.

I would like to express my sincere gratitude to all members of the reading committee, who agreed to examine this work and provided a useful comments for its improvement.

At last, I would like to thank all my friends and mates who made my time as a student

memorable and enjoyable.

TABLE OF CONTENTS

LIST OF TABLES

LIST OF FIGURES

SUMMARY

Many diverse complex phenomena that are found in fundamental problems of atomic physics and chemistry can be understood in the framework of nonlinear theory. Most of simple atomic and chemical systems are classically described by the Hamiltonian models of dimension three and higher. The behavior of these systems manifests itself in the intrinsic character of the classical phase space dynamics. To give an example, non–statistical relaxation dynamics of polyatomic molecules and the ionization mechanism of atoms inside electromagnetic fields are relevant to a non–uniform structure of the classical phase space of both systems. The essential features of the dynamics of these systems are defined by the stability structures of their phase space, such as periodic and quasiperiodic motions. Recent progress in nonlinear dynamics theory provides a strong background for studying complex multidimensional systems, which are the classical models of simple chemical and atomic systems.

In this work we report the results of an extensive numerical analysis for two multidimensional Hamiltonian models: a planar model of the chemical system of the carbonyl sulphide molecule, and a two–dimensional model of the atomic system of hydrogen, driven by non–stationary electromagnetic fields.

The intramolecular relaxation dynamics of the carbonyl sulphide molecule is studied for different excitation regimes: from the low–energy regime to the high–energy regime, near and at the dissociation threshold. We study multidimensional phase space dynamics by applying the method of fast Lyapunov indicators and time–frequency wavelet analysis. The first method identifies the zones of regular and chaotic behavior within the multidimensional phase space. The results of the fast Lyapunov indicator stability analysis are used as a starting point to study important resonances and the mechanism of chaotic diffusion in the phase space of the system by means of the time–frequency wavelet analysis.

The ionization dynamics of the classical two–dimensional hydrogen atom in a strong elliptically polarized microwave field is studied for different parameters of the electromagnetic field. The fast Lyapunov stability analysis pictures phase space structures and its relevance to the classical ionization dynamics of the system. It allows to estimate the dependence of ionization probabilities on the parameters of the field, such as amplitude and polarization. We show that application of the fast Lyapunov indicator method can be potentially important for control of ionization of Rydberg states performed in the experiment.

Our results provide insight into the characteristic features of phase space dynamics of two multidimensional Hamiltonian systems. The application of the methods shown in this work can lead to a better understanding of many intrinsic phenomena observed in chemical and atomic systems that were not well–explained in the framework of traditional theories.

CHAPTER I

INTRODUCTION

The dynamics of multidimensional Hamiltonian systems features many interesting phenomena that have not been so far well–understood. A good example is the phenomenon of Arnold diffusion (stochastic diffusion along resonances) that has been observed for the Hamiltonian systems of dimension three and higher [1]. The study of a complex high–dimensional phase space dynamics is important in many fundamental problems of modern physics, as is found in problems of chemical physics [2, 3], celestial mechanics [4], molecular dynamics [5, 6], particle accelerators [7], and atomic physics [8]. Advances in dynamical system theory offers a variety of techniques for mining high–dimensional data for any underlying phase space structures. For the Hamiltonian systems of dimension two, the phase space dynamics can be visualized via Poincaré surfaces of section. They picture chaotic and regular regions of the phase space and provide an efficient tool for understanding important transitions in the global dynamics of the system. Analyzing the dynamics of higher–dimensional Hamiltonian systems by extrapolating this technique is not straightforward, since the Poincaré section has dimension four for systems with three degrees of freedom. Instead, we discuss the application of two alternative methods that permit to uncover important phase space stability structures.

The first technique is the fast Lyapunov indicator (FLI) method that has been proposed in [9] as an efficient diagnostic of regular and chaotic motions for the Hamiltonian systems. The main idea of the method is to measure the degree of chaoticity for each trajectory from phase space. For two regular trajectories with initial conditions chosen in a small neighborhood, the separation distance grows at most linearly with time, and the tangent vector to the flow shows at most linear growth. For two chaotic trajectories initially close to each other, the separation distance grows exponentially with time and the tangent vector grows exponentially along the flow. The FLI method is based on the computation of the

evolution of a set of tangent vectors along the Hamiltonian flow. This method is analogous to characteristic Lyapunov exponent calculations [10, 11]. The largest Lyapunov exponent as an infinite time quantity requires a long–time integration for reliable prediction of dynamics. In contrast, the fast Lyapunov indicator technique allows the distinction of different types of dynamical behaviors after a short–time interval. The second technique is the time–frequency wavelet analysis [12] and is similar to the windowed Fourier transform method [13, 14]. It allows study of the dynamics of a single trajectory by viewing its instantaneous frequency evolution with time. By monitoring the time–variation of instantaneous frequencies of the trajectories, it is easy to identify the important resonances of the system and chaotic transport of trajectories across the phase space. In this study, we present the application of both methods to vibrational dynamics of planar carbonyl sulphide (OCS) molecule and the classical ionization dynamics of hydrogen atom in elliptically polarized microwave fields.

Over the past decades the mechanism of an intramolecular energy relaxation for the highly excited OCS molecule has been the subject of much controversy in the physics and chemistry communities [15, 16]. The vibrational dynamics of the planar and collinear model of the OCS demonstrates evidence of a nonstatistical energy relaxation behavior. Despite the fact that the classical model of the OCS shows strong coupling between vibrational modes of the system, it has been observed that for a given initial energy distribution within vibrational modes of the system, relaxation to the average statistical distribution occurs after a time much longer than the expected relaxation time [15]. Although the pioneering work of Carter and Brumer [15] was the first to relate intramolecular energy relaxation to classical phase space dynamics, Davis [16] was the first to explain the long–time rates of energy relaxation by studying the underlying phase space structures of the classical collinear model of the OCS. Davis argued that the phase space invariant tori act like partial barriers to the fast diffusion of trajectories across the phase space of the system. In this way, a long–time energy redistribution among vibrational modes of the molecule for the collinear OCS model is related to the trappings of chaotic trajectories in the vicinity of the phase space invariant tori.

In comparison to the collinear OCS model the planar OCS model has a high dimensionality that is expected to result in much more complex phase space dynamics. Indeed, for the planar model the effective phase space of the system is five–dimensional, and the invariant tori are at most three–dimensional structures. The mechanism of the long–time energy redistribution for the high–dimensional system of the planar OCS is attributed to the long–time trappings of chaotic trajectories in the vicinity of the invariant tori. In order to study the intrinsic dynamics of phase space trajectories in the vicinity of invariant tori, time–frequency analysis has been employed. By looking at the evolution of instantaneous frequencies for a chaotic trajectory, one can identify the interval of trapping and the frequencies of the invariant object, around which the trajectory is trapped. We identify the main resonances in the system by applying FLI stability analysis in conjunction with time–frequency analysis for the energies of the system below and at the dissociation threshold. For energies that are far below the dissociation threshold, the system is in a near–to–integrable regime, and for the energies near and at the dissociation the system is in a non–integrable regime. Application of these methods for all the regimes of the system allows us to view evolution of the phase space structures with the increase of the vibrational excitation in the system.

Much of our understanding of the complex details of classical ionization mechanism of hydrogen atom driven by non–stationary electromagnetic fields depends on an adequate knowledge of the full multidimensional dynamics of the system. The problem of ionization of hydrogen atom in a strong elliptically polarized microwave field is known to exhibit complex features that are not observed for the case of ionization by the circularly and linearly polarized fields. Specifically, the existing experimental data reveal high sensitivity of ionization dynamics to the small changes of field polarization. Due to absence of the integrals of motion (energy and angular momentum are not conserved) the classical model of this quantum system does not allow a reduction in dimensionality of the system. The ellipticity of the applied field destroy the underlying symmetries of the system, which prevents the simplification of the system's dynamics. We study phase space dynamics using finite time stability analysis rendered by the fast Lyapunov indicators technique. The concept of the

zero–velocity surface is used to initialize calculations and visualize the dynamics. Our analysis brings forth the maps of stability calculated for two different configurations of the initial energies subspace. We qualitatively estimate the behavior of ionization thresholds versus parameters of the applied field, such as polarization and scaled amplitude. The non–monotonic increase of ionization yields is linked with the stabilization and collapse of the resonant tori structures near the maximum of the zero–velocity surface.

The main advantage of the FLI method and the time-frequency analysis method is that they provide a complete description of the phase space dynamics of the system. The methods allows identification of the main chaotic and resonant zones and description of the important features of transport of chaotic trajectories across the phase space. In the case of the generic polyatomic molecule, both methods can give information about the intramolecular energy redistribution and indicate the main resonances and their importance in the relaxation dynamics of the system. Applying fast Lyapunov Indicators analysis to classical hydrogen in elliptically polarized microwave fields reveals significant variations in the phase space stability structures and ionization dynamics that occur with the change of field amplitude and polarization.

This thesis is organized in five chapters. In Chapter 2 the basic definitions and concepts of the fast Lyapunov indicator method and the time–frequency wavelet analysis are introduced. Application of both methods to integrable and near–to–integrable Hamiltonian systems are discussed.

In Chapter 3 the classical model of a highly excited OCS molecule is studied. We describe the classical phase space structures including main resonant and chaotic regions in terms of the fast Lyapunov indicator stability plots. The results are compared with the time–frequency analysis results for several values of the energies below and at the dissociation threshold. In addition, the qualitative behavior of the system near to dissociation threshold is discussed.

In Chapter 4 the classical ionization dynamics of hydrogen atoms inside elliptically polarized microwave fields is studied. The system is time–dependent and is in a non–integrable regime. We apply the FLI method together with the time-frequency analysis

for initial conditions corresponding to energies above and below the Stark saddle point. We picture phase space structures and their correspondence to the ionization probability thresholds computed for different values of the polarization and amplitude of the electric field.

Finally, Chapter 5 concludes with a discussion of the main results and directions for the future research.

CHAPTER II

NUMERICAL METHODS

2.1 Fast Lyapunov Indicator Method

The phase space of a non–integrable Hamiltonian system is divided into regular and chaotic regions of dynamics. In order to characterize the global stability structures of the phase space of multidimensional system, one would look for a method that provides a clear representation of the chaotic and regular regions in the phase space, similarly to the representation obtained with Poincaré surface of section (SOS). However, for the three– and higher–dimensional systems the construction and use of the SOS might be very complicated. Another possibility to study multidimensional dynamics is to define an indicator of chaoticity for each trajectory from a given subspace of the system's phase space. Various successful diagnostics for different types of dynamical behaviors can be adopted from the dynamical systems literature; an indicator can be defined as characteristic Lyapunov exponent [10, 11], strength of diffusion of instantaneous frequency in the frequency space [17], measure of complexity of the Fourier spectrum [18] and other useful predictive tools of dynamics [19, 20]. The most common technique is the method of characteristic Lyapunov exponents (CLE). The method is based on the computation of the eigenvectors of the linearized flow of the system at each time step and averaging the results over long interval of time. The method serves as an accurate measure of regularity of dynamics from a theoretical point of view, however, long–time calculations require big computational efforts and are impractical for large and complex systems. In addition, one should expect to obtain a reliable prediction of the dynamics over time interval smaller than the Lyapunov time defined as $\tau = 1/\Lambda$, where Λ is the largest characteristic Lyapunov exponent. The reason is that with the increase of integration time the computational error increases resulting in significant error in determination of the CLE. As a short–term predictive tool a method of the fast Lyapunov indicators (FLI) was used recently in [9] to study asteroidal motions.

This technique is analogous to the method of the Finite-Time Lyapunov Exponents method adopted for the finite–time flows found in atmospheric data studies [21, 22]. The method of characteristic Lyapunov exponents determines the chaoticity of trajectory from measuring the degree of divergence of two nearby trajectories. The FLI method estimates the chaoticity of an analyzed trajectory by calculating the tangent vector growth along it. For each initial condition from the phase space of multidimensional system the FLI is defined as the maximum of the norm of tangent vector attained over the finite interval of time. It will be shown later in this section that the tangent vector grows exponentially for chaotic trajectories and linearly for regular trajectories. Therefore, by measuring the maximum of the norm of tangent vector along the flow it is possible to distinguish chaotic from a regular behavior already after a short integration period. Another advantage of the FLI method is that it is independent on the dimension of investigated system. Hence, it can be used for predicting chaotic and regular dynamics of multidimensional complex systems that do not permit the use of any other numerical and analytical techniques.

The FLI method was used previously in several applications: study of coupled standard map dynamics, asteroidal motion [23, 24], celestial mechanics problems [25] and vibrational dynamics of the polyatomic system [26]. In this work we demonstrate for the first time the application of the method to atomic system (see Chapter 4). In Chapter 3 we provide the FLI results for the chemical system of the carbonyl sulphide molecule.

In this section we present a brief description of the fast Lyapunov indicator method. All the details and analytical results related to the application of the method to near–to–integrable Hamiltonian systems can be found in [23].

2.1.1 Definition

The fast Lyapunov indicator method was proposed by Froeschlé *et al* in [9] to study weak chaos in high–dimensional systems. The main idea of the method is to obtain a fast and reliable diagnostic of the stability properties of numerical solution on a short–time interval.

Let us consider a d-dimensional flow

$$\frac{d\mathbf{x}}{dt} = \mathbf{f}(\mathbf{x}) \ , \tag{2.1}$$

where $\mathbf{x} = (x_1, x_2, \ldots, x_d)$ is a vector of the d–dimensional flow and $\mathbf{f}(\mathbf{x}) \in \mathrm{R}^d \times \mathrm{R}^d$ is a velocity field matrix. The system of equations for the tangent vector $\mathbf{v}$ results

$$\frac{d\mathbf{v}}{dt} = Df(\mathbf{x}) \cdot \mathbf{v} \ , \tag{2.2}$$

where Df is a matrix with elements $\{Df\}_{ij} = \partial f_i / \partial x_j$. We integrate the above systems starting with initial conditions $\mathbf{x}_0$ and initial tangent vector $\mathbf{v}_0$. In principle, one should integrate the system of equations given by $d \times d$ Jacobian matrix $J(t)$

$$\frac{dJ}{dt} = Df(\mathbf{x})J \ , \tag{2.3}$$

where the columns of the Jacobian matrix J are the tangent vectors $\mathbf{v}(t)$ of the flow. In practice, in order to reduce the computational efforts we only integrate the equations for $\mathbf{v}(t)$ starting with a given $\mathbf{v}_0$ fixed for all the sampled trajectories at the same amplitude and direction. Any tangent vector $\mathbf{v}(t)$ of the flow will eventually converge to the direction of the unstable manifold of the flow, unless the initial vector $\mathbf{v}_0$ is chosen to be exactly on the stable manifold.

Definition. *The Lyapunov indicator is defined for every initial condition* $\mathbf{x}_0$ *of system* (2.1) *as the following dynamical quantity:*

$$\phi(t; \mathbf{x}_0) = \max_{0 \le t' \le t} \log \|\mathbf{v}(t'; \mathbf{x}_0)\|, \tag{2.4}$$

where $\mathbf{v}(t'; \mathbf{x}_0)$ *is a tangent vector from a tangent space of the flow defined at time* t' *for a trajectory with initial conditions* $\mathbf{x}_0$.

The Lyapunov indicator $\phi(t; \mathbf{x}_0)$ is a monotonically increasing function of time. In the following subsections the behavior of the Lyapunov indicator defined in (2.4) is discussed in details for the case of an integrable and near –to–integrable Hamiltonian system.

2.1.2 The Case of an Integrable Hamiltonian System

According to the results of the Liouville–Arnold theorem [1] it is possible to find a transformation to the canonical action–angle variables in order to express an integrable Hamiltonian in terms of actions coordinates alone [1]. Let us assume that for d–dimensional Hamiltonian system a set of action–angle coordinates is found $(\mathbf{I}, \phi) \in \mathrm{R}^d \times \mathrm{T}^d$, where T^d is an

d–dimensional torus. Then, the Hamiltonian, written as $H = H_0(\mathbf{I})$, depends exclusively on actions. The Hamiltonian equations of motion can be written as follows:

$$\frac{d\mathbf{I}}{dt} = \mathbf{0}, \qquad \frac{d\phi}{dt} = \frac{\partial H_0}{\partial \mathbf{I}} = \omega(\mathbf{I}). \tag{2.5}$$

The system of equation for the tangent flow defined in (2.2) results

$$\frac{d\mathbf{v}}{dt} = \begin{pmatrix} 0 & 0 \\ \omega'(\mathbf{I}) & 0 \end{pmatrix} \cdot \mathbf{v}, \tag{2.6}$$

where $\omega'(\mathbf{I})$ is a $d \times d$ matrix with the elements $\{\partial\omega_i/\partial I_j\}_{i,j=1,d}$, and $\mathbf{v} = (v_I, v_\phi) \in \mathrm{R}^{2d}$ is a tangent vector along the flow. Since $\mathbf{I} = (I_1, I_2 \ldots, I_d)$ is a constant set of actions along trajectory, the solution for any initial tangent vector (v_I, v_ϕ) is

$$v_I(t) = v_I(0), \qquad v_\phi(t) = v_\phi(0) + \omega'(\mathbf{I}(\mathbf{0}))v_I(0)t \ . \tag{2.7}$$

It follows that for any solution $(\mathbf{I}, \phi)$ of integrable Hamiltonian $H = H_0(\mathbf{I})$ the norm of the tangent vector $\mathbf{v}(t)$ evolves at most linearly with time:

$$\|v_I(t)\| = \|v_I(0)\|, \qquad \|v_\phi(t)\|^2 = \|v_\phi(0)\|^2 + \|\omega'(\mathbf{I}(\mathbf{0}))v_I(0)\|^2 t^2 \ . \tag{2.8}$$

Then the fast Lyapunov indicator defined in (2.4) evolves like logarithmic function of time $\phi(t) \simeq \log(t)$.

2.1.3 The Case of a Near–to–integrable Hamiltonian System

The celebrated Kolmogorov stability theorem [27, 28, 29] states that a weak perturbation of Hamiltonian system leads to only small deformations of the tori with the incommensurate frequency ratios. These tori are called the Kolmogorov–Arnold–Moser (KAM) tori. It was shown in [23] that for any solution on the KAM torus fast Lyapunov indicator up to a small order term evolves like for a solution on the unperturbed torus of an integrable system.

For the ϵ–perturbed Hamiltonian of the form:

$$H_\epsilon(I, \phi) = H_0 + \epsilon f(\mathbf{I}, \phi) \ , \tag{2.9}$$

where ϵ is a small parameter and $H_0 = H_0(\mathbf{I})$, the set of equations for the tangent vector $\mathbf{v}^\epsilon = (v_I^\epsilon, v_\phi^\epsilon)$ yields:

$$\begin{aligned} \frac{dv_{I_j}^\epsilon}{dt} &= \sum_{i=1}^{d} \frac{\partial {dH_0}^2}{\partial I_j \partial I_i} v_{I_i} + \epsilon \sum_{i=1}^{d} \frac{\partial f^2}{\partial I_i \partial I_j} v_{I_i} + \epsilon \sum_{i=1}^{d} \frac{\partial f^2}{\partial I_j \partial \phi_i} v_{\phi_i}, \\ \frac{dv_{\phi_j}^\epsilon}{dt} &= \epsilon \sum_{i=1}^{d} \frac{\partial f^2}{\partial \phi_j \partial I_i} v_{I_i} - \epsilon \sum_{i=1}^{d} \frac{\partial f^2}{\partial \phi_i \partial \phi_j} v_{\phi_i} \ . \end{aligned} \tag{2.10}$$

For $\epsilon = 0$ the solution of the system (2.10) is reduced to the solution in (2.7). It was proven in [23] that the following result holds true.

Theorem. *Suppose that perturbed Hamiltonian system in* (2.9) *satisfies hypotheses of the KAM theorem. Then the norm* $\|v^\epsilon(t)\|$ *of tangent vector* $v^\epsilon(t)$ *satisfies the following estimate:*

$$\|v^\epsilon(t)\| = \|\frac{\partial {H_0}^2}{\partial I^2}(\mathbf{I}(0)) v_I(0)\| t + \mathcal{O}(\epsilon^\alpha t) + \mathcal{O}(1) \ , \tag{2.11}$$

where $\alpha > 0$ *is a constant.*

This theorem is a direct consequence of the KAM theorem, since it assures that the dynamics on the KAM torus corresponds to the dynamics given by the integrable Hamiltonian H_0 that is ϵ–close to the perturbed Hamiltonian in (2.9). Therefore, for any solution on the KAM torus the fast Lyapunov indicator evolves up to a small order term like for a solution on an unperturbed torus for a Hamiltonian H_0.

2.1.4 Application to the Chirikov Map

In order to demonstrate the analysis of dynamics by FLI method we show the application of the method to a well–known Chirikov map [30] given by the following set of equations:

$$\begin{aligned} x_{n+1} &= x_n + K \sin y_n, \ \mathrm{mod}\ 2\pi, \\ y_{n+1} &= y_n + x_{n+1}, \ \mathrm{mod}\ 2\pi, \end{aligned} \tag{2.12}$$

where $K \in \mathrm{R}$ is the stochasticity parameter and $(x_n,\ y_n)$ are the sequence of iteration points. This map has been traditionally used in the dynamical system community as a test ground for examining general nonlinear phenomena, such as transitions from regular to chaotic dynamics.

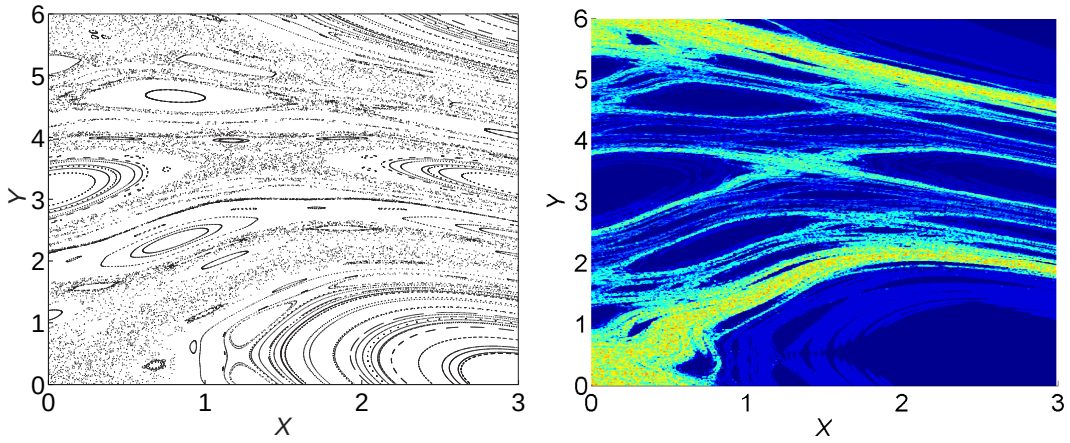

Figure 2.1: (Left) The Poincaré surface of section and (right) FLI plot for the Chirikov map. $K = 0.999$.

In Figure 4.5 the Poincaré surface of section and the FLI plot are shown for the parameter of the Chirikov map $K = 0.999$. It can be observed from the Poincaré surface (left panel) that at this value of the parameter the system is non–integrable and the phase space consists of resonant zones and thin chaotic layers represented by the chaotic spread of points between the non–resonant tori structures. On the FLI contour plot (right panel) the color assignment corresponds to the maximum value of the FLI attained over the integration period for every point from a mesh of initial points on the $x - y$ plane. Every chaotic layer on the Poincaré surface is associated with the high values of the FLI. The dark blue islands correspond to the resonant zones, and the highlighted areas correspond to the chaotic zones. Obviously, both methods provide a clear description of the phase space dynamics in terms of chaotic and resonant structures. Unlike the Poincaré technique, the application of the FLI stability analysis method is easily implemented for high dimensional systems.

2.1.5 FLI Method versus Characteristic Lyapunov Exponent Method

The Lyapunov Indicator defined in the expression (2.4) serves as an efficient diagnostic tool of chaoticity for every analyzed trajectory in the system. Similarly to the method of the CLE defined over the finite interval of time, the FLI procedure supply the information about the dynamical behavior of trajectory. Indeed, the characteristic Lyapunov exponent is defined as the quantity $\lambda = \lim_{t\to\infty} \ln \|\mathbf{v}(\mathbf{t})\|/t$. The CLE is zero for any periodic or

quasiperiodic trajectory, and it is positive for any chaotic trajectory. The growth of the tangent vector along the flow evaluated by integration of equations (2.1) and (2.2) is proportional to the growth of initial separation distance between the two neighboring trajectories in a phase space. In fact, the evolution of the tangent vector computed for weakly chaotic and chaotic trajectories obeys an exponential law. At the same time the growth of the tangent vector for regular trajectories follow the linear behavior. Already after a short interval of time it is possible to distinguish clearly between two different behaviors of trajectories by looking at the maximum value attained by the FLI. This is the advantage of the method in comparison with the method of characteristic Lyapunov exponents. In some cases the Lyapunov exponent calculation does not allow making a clear distinction between different dynamical behaviors over the finite interval of time. It happens when the rate of decrease of the Lyapunov exponent with time is very slow and even at large times the Lyapunov exponent approaches a very small value but remains positive. In this situation one sees the advantage of applying FLI technique, which can discriminate regular from chaotic motions over a relatively short–time period.

In the method of CLE the local tangent vectors are computed and renormalized at each integration step in order to avoid the overflow. In contrast, the fast Lyapunov indicator takes advantage of the evolution of the tangent vectors renormalizing them only after period of time when the norm of the vectors reaches some control value. This period of time can be used as an indicator of the chaoticity. Another variation of the method would be to fix the control interval of time and to look at the final maximum value attained by the norm of the largest tangent vector. We demonstrate the application of the latter method in Chapters 3 and 4.

2.2 Continuous Wavelet Analysis

In this section time–frequency method is considered as an alternative method for analyzing dynamics of multidimensional Hamiltonian systems. Unlike other methods (the Poincaré surface of section or the fast Lyapunov indicator analysis) that are used to study a phase space dynamics the time–frequency analysis does not require integration of a large number

of trajectories from a phase space of a system in order to explore the invariant stability structures inside it. The main idea of the method is to study the dynamics of a single trajectory in the time–frequency space by looking at evolution of its frequencies with time. While a chaotic trajectory is wandering inside the phase space from one resonant area to another its instantaneous frequencies evolve inside the time–frequency space. One can study chaotic dynamics and resonant structures by viewing the time evolution of instantaneous frequencies of a single trajectory. This kind of analysis is feasible for a Hamiltonian system of any dimension.

2.2.1 Introduction to Wavelets

Time–frequency wavelet decomposition has been used in different fields of science and engineering to analyze the non–stationary time signals. Successful applications of it can be found in signal processing, data compression, and telecommunications [12, 14, 31]. A precise multi–scale resolution provided by the wavelets is used in analyzing many complex and nonlinear signals including cardiac activity time series [32], seismic trace signals [33], and North Atlantic oscillation dynamics [34]. Recently wavelet decomposition was used for the turbulent flow modelling and denoising in [35] and for chaos control and synchronization of a nonlinear system of chaotic oscillators in [36]. Another useful application can be found for the low–dimensional dissipative systems [37]. In general, there exist a variety of wavelet methods used for the time–frequency decomposition of nonlinear signals arising in different applications of science. For the Hamiltonian systems studied here we applied the Morlet–Grossmann wavelet decomposition. Unlike the Fourier transform method that decomposes time series by using functions localized in frequency space and completely delocalized in time, the Morlet–Grossmann wavelet transform provides very sharp localization in time–frequency space [14]

The idea of a local "windowed" frequency analysis of non–stationary signals was proposed at the beginning of the last century. It was realized that many complex signals can not be analyzed by the stationary frequency analysis. The new method that will allow to follow the fast instantaneous frequency variations by performing a local "windowed" Fourier

decomposition of the analyzed signal was discussed actively in the literature. In fact, the notion of "instantaneous spectra" was proposed first by Sommerfeld in 1890 in his doctoral thesis. Later Gabor [13] in 1946 introduced the idea of decomposition of a signal into time–frequency "atoms" inside the time–frequency domain. Such time–frequency atoms are represented by Gaussian functions obtained from an elementary gaussian by translation in time. The elementary wavelet is chosen to be a Gaussian function: $g(t) = e^{-t^2/2\sigma^2}/(\sigma^2\pi)^{1/4}$.

The family of Gabor wavelets is defined as a parametric set of $\mathbf{L}^2(\mathrm{R})$ integrable functions $\{\phi_\gamma\}_{\gamma\in\Gamma}$, where γ is a multi–index parameter. The $\mathbf{L}^2(\mathrm{R})$ norm of each function ϕ_γ is chosen to be equal to one. For a given signal $f(t) \in \mathbf{L}^2(\mathrm{R})$ the Gabor transform is defined as follows:

$$Sf(u,\xi) = \int_{-\infty}^{+\infty} f(t) g^*_{\xi,u}(t) dt, \tag{2.13}$$

where $g_{\xi,u}(t)$ is a modulated Gaussian wavelet atom obtained from an original Gaussian wavelet by modulation with frequency and translation in time:

$$g_{\xi,u}(t) = e^{i\xi t} g(t-u). \tag{2.14}$$

The notion of time–frequency "atoms" in signal processing is analogous to the concept of canonical coherent states introduced in quantum mechanics by Schrödinger [38] in 1926 for quantizing harmonic oscillator. Similarly to the restriction in resolution of position and momenta imposed by the Uncertainty Principle in quantum mechanics, the time–frequency "atoms" can not be completely localized in time–frequency space. For example, for a Gaussian window the time variance measured around a point (u,ξ) is:

$$\sigma_t(u,\xi) = \left(\int_{-\infty}^{+\infty} (t-u)^2 |g_{u,\xi}(t)|^2 dt \right)^{1/2}. \tag{2.15}$$

It is independent of u and ξ and is equal to $\sigma/\sqrt{2}$. Similarly, the frequency variance around a point (u,ξ) is calculated :

$$\sigma_{fr}(u,\xi) = \left(\frac{1}{2\pi} \int_{-\infty}^{+\infty} (\omega-\xi)^2 |\widehat{g}_{u,\xi}(\omega)|^2 d\omega \right)^{1/2}, \tag{2.16}$$

and σ_{fr} is equal to $1/(\sigma\sqrt{2})$ for a Gaussian wavelet. It follows from the estimates (2.15) and (2.16) that the time–frequency uncertainty for a Gaussian wavelet is: $\sigma_t\sigma_{fr} = \frac{1}{2}$. It shows that gaussian functions have the property of minimal time–frequency resolution [14].

Therefore, time–frequency domain for each analyzed signal is discretized by the Heisenberg boxes of area larger than or equal to $\frac{1}{2}$. By attempting to get a high–frequency resolution of a signal one necessarily loses localization of it in time and vice versa. The value of parameter σ can be adjusted in order to get the required time–frequency resolution. In practice, one can chose discretization of the time–frequency plane by knowing a priori the character of the analyzed signal.

However the Gabor analysis does not provide a reliable resolution for non-stationary signals with rapid frequency variations. The Gabor wavelet decomposition uses an a priori fixed width of the wavelet and any events happening on scale smaller than the width are missed by such decomposition. Another method was proposed by Grossmann and Morlet [33] in 1984. It distinguishes the rapid transitions that happen in time–frequency content of a signal by adjusting the length of the wavelet window. By developing high–frequency resolution methods for seismic data analysis Grossmann have used the family of wavelets obtained from an elementary Gaussian wavelet by translation in time and dilation in frequency and in time. This family of wavelets are referred in the literature as Morlet–Grossmann (MG) wavelets or continuous wavelets. The continuous wavelet transform for the $\mathbf{L}^2(\mathrm{R})$ integrable function $f(t)$ is defined as an inner product in $\mathbf{L}^2(\mathrm{R})$:

$$Wf(u,s) = \int_{-\infty}^{+\infty} f(t)\phi_{u,s}(t)dt, \tag{2.17}$$

where the wavelet $\phi_{u,s}(t)$ is a modulated Gaussian wavelet translated by u and dilated by s in time :

$$\phi_{u,s}(t) = \frac{1}{\sqrt{s}(\sigma^2\pi)^{1/4}} e^{i\frac{\eta}{s}(t-u)} e^{-(t-u)^2/2\sigma^2 s^2}. \tag{2.18}$$

The time–frequency resolution of a MG wavelet transform does not depend on the central time u of the wavelet but depends on the scale s. The time spread around a point $(u, \xi = \eta/s)$ in the time–frequency plane is :

$$\sigma_t(u,s) = \left(\int_{-\infty}^{+\infty} (t-u)^2 |\phi_{u,s}(t)|^2 dt \right)^{1/2} \tag{2.19}$$

and is equal to $\sigma s/\sqrt{2}$. The frequency spread around $\xi = \frac{\eta}{s}$ is defined as:

$$\sigma_{fr}(u,s) = \left(\frac{1}{2\pi} \int_{-\infty}^{+\infty} \left(\omega - \frac{\eta}{s}\right)^2 |\widehat{\phi}_{u,s}(\omega)|^2 d\omega \right)^{1/2} \tag{2.20}$$

is independent of u and equal to $1/(\sigma s\sqrt{2})$. The time–frequency uncertainty for a MG wavelet is $\sigma_t \sigma_{fr} = \frac{1}{2}$. The continuous wavelet transform adjusts the width of the wavelet according to the frequency of the analyzed signal at time u. For the high frequencies it uses a short–time interval and for the low frequencies it uses a long–time interval. This adjustment allows to follow rapid transitions for highly chaotic non-stationary signals.

2.2.2 Frequency Analysis for the Hamiltonian Systems

2.2.2.1 Frequency space for integrable Hamiltonian systems

The phase space dynamics of an n–dimensional Hamiltonian system consist of chaotic structures and various stable structures of dimension less or equal to n, such as periodic orbits, invariant tori and their stable and unstable manifolds. For an integrable Hamiltonian system there exist as many integrals of motion as the numbers of degrees of freedom. In terms of the action–angle variable the hamiltonian equations of motion can be written in the form:

$$\dot{I}_j = 0, \qquad \dot{\theta}_j = \frac{\partial H_0(I)}{\partial I_j} = \nu_j(I), \qquad j = 1, \ldots, n \tag{2.21}$$

Solutions of this system move along the invariant tori. Each torus is a product of true circles with constant radii I_j and a uniquely assigned frequency vector $\nu = (\nu_1, \nu_2, \ldots, \nu_n)$. Resonant tori are described by the frequencies that are linearly dependent:

$$m_1\nu_1 + m_2\nu_2 + \ldots + m_n\nu_n = 0, \tag{2.22}$$

where $m = (m_1, m_2, \ldots, m_n)$ is an integer vector. If the frequency condition (2.10) is not satisfied for any integer vector m then the torus is non-resonant. Any trajectory moving along the torus is a quasiperiodic function and can be expressed in the finite series form as follows:

$$f(t) = \sum_{m \in Z^n}^{n} a_m e^{i<m,\omega>}, \tag{2.23}$$

where $< m, \omega >= m_1\omega_1 + m_2\omega_2 + \ldots + m_n\omega_n$ and m is an integer vector.

2.2.2.2 Frequency space for a near–to–integrable Hamiltonian system.

For a near–to–integrable system derived from an unperturbed integrable system by introduction of a small ϵ order perturbation term the dynamics is described by the following

perturbed Hamiltonian:

$$H = H_0(I) + \epsilon H_1(I, \phi), \tag{2.24}$$

expressed in terms of action-angle variables $I \in \mathrm{R}^n$ and $\phi \in \mathrm{T}^n$. The H_0 term is an integrable Hamiltonian expressed in terms of action variables only. if the perturbation is small the Kolmogorov set of tori remain essentially unchanged. Each torus in this set is described by the same frequency vector as that of the unperturbed torus. A complement set of the Kolmogorov set of tori has measure, which tends to zero as the magnitude of the perturbation decreases to zero $\epsilon \to 0$. Trajectories moving on the Kolmogorov tori are quasiperiodic motions that can be expressed in the form (2.23). Any solution with initial conditions ϵ–close to the invariant torus will stay in the ϵ vicinity of this torus for a large finite intervals of time of the order $1/\epsilon$. In fact, the following theorem due Nekhoroshev [39] states:

Theorem. *Given Hamiltonian H_0 which satisfies steepness condition of the form:*

$$|\nabla(H_0|_\lambda)|_{\widetilde{I}}| > Cd^\alpha, \tag{2.25}$$

where $\widetilde{I}$ is the point of the plane $\lambda \in \mathrm{R}^n$ of actions. For $0 < \epsilon < \epsilon_0$ sufficiently small any solution $(I(t), \phi(t))$ of the perturbed system (2.12) satisfies the following exponential estimate:

$$|I(t) - I_0(t)| < \epsilon^b \tag{2.26}$$

for all $t \in [0, T]$, where

$$T = \frac{1}{\epsilon} \exp\left(\frac{1}{\epsilon^a}\right), \tag{2.27}$$

and a and b are the positive integers.

According to the Nekhoroshev theorem for any solution of a near–to–integrable system an accurate quasiperiodic approximation of it can be given on a finite–time interval satisfying the exponential estimate (2.27). Such quasiperiodic approximations were used to study near–to–integrable dynamics of the planetary systems by Laskar [40] in 1990. Laskar [17, 40] proposed to define a characteristic of each motion by looking at the evolution of its time–varying frequencies inside the frequency space. The general idea of Laskar's method

is to define for any solution of the form (2.23) its quasiperiodic approximation $\widetilde{f}(t)$ on a large but finite time interval $[t-T, t+T]$ in the following form:

$$\widetilde{f}(t) = \sum \widetilde{a}_j e^{i\widetilde{\omega}_j t}, \tag{2.28}$$

where the coefficients $\widetilde{a}_j$ are given in a decreasing order $|\widetilde{a}_1| \geq |\widetilde{a}_2| \geq \ldots |\widetilde{a}_j| \geq \ldots$. The first frequency component $\widetilde{\omega}_1$ can be retrieved by determining the maximum over σ of the scalar product:

$$\psi(\sigma) =< f(t), e^{i\sigma t} >= \frac{1}{2T}\int_{-T}^{T} f(t)e^{-i\sigma t}\chi(t/T)dt, \tag{2.29}$$

where $\chi(t/T) = 1 + cos(\pi t)$ is a Hanning window filter. The first frequency component $\widetilde{\omega}$ is defined as the fundamental frequency corresponding to the largest amplitude $|\widetilde{a}_1|$. The second frequency component $\widetilde{\omega}_2$ is obtained iteratively from the maximum of the following scalar product $< f_1(t), e^{i\sigma t} >$, where $f_1(t) = f(t) - \widetilde{a}_1 e^{i\widetilde{\omega}_1 t}$. Since the basis $e^{i\widetilde{\omega}_k t}$ is not orthogonal for the scalar product $< \cdot, \cdot >$, at each step of the iteration a Gramm-Schmidt orthogonalization procedure is performed on sequence $e^{i\widetilde{\omega}_k t}$. In this way, a frequency vector $\omega(t) = (\omega_1(t), \omega_2(t), \ldots, \omega_n(t))$ is defined for each fixed time t on a finite–time interval $[t-T, t+T]$. The algorithm allows to determine a frequency vector for a quasiperiodic solution with an accuracy of order T^{-4} [41]. This is much better approximation than the one obtained with the fast Fourier transform, which gives an accuracy of order T^{-1}.

For a weakly chaotic trajectory the quasiperiodic approximation proposed by Laskar can be used on a finite time intervals. The solutions that can be studied with the Laskar frequency analysis should belong to the class of stable or "marginally stable" solutions that satisfy the exponential estimates of Nekhoroshev given in (2.26) and (2.27). An example of a near–to–integrable system studied by Laskar is the Solar system [40, 42]. The evidence of a large scale chaos was found for the planets and asteroids of the Solar system. Although for a times of several millions of years the motion of the planets in the Solar system does show only very weak variations, for a times over a billion of years strong chaotic variations occur in the Solar dynamics. In this case the Solar dynamics can be studied by the frequency analysis on a time scale of several millions of years. The method of Laskar has been applied successfully to study global dynamics of the planetary and asteroidal systems [4, 43] as

well as the particle accelerator dynamics [7].

2.2.3 Wavelet Transform Algorithm

There is a large class of Hamiltonian systems, for which the theory developed for near–to–integrable Hamiltonian systems can not be applied. Indeed, by going to far–from–integrable limit one finds strong chaos and rapid transitions in the time series of the observed chaotic trajectories. In a strong perturbative regime Nekhoroshev results are no longer valid. Many resonant structures inside a phase space are destroyed and large chaotic zones where chaotic trajectories diffuse rapidly are present. The use of the quasiperiodic approximations proposed by Laskar [40] can give wrong information about the frequencies of an analyzed sequence. For such systems the application of the feedback time–frequency methods is becoming well accepted in the literature [5, 44]. One of them is the wavelet method. It automatically adjusts the length of time window resolution to fit rapid temporal variations of an analyzed signal.

In this subsection a brief description of the MG wavelet transform algorithm for extracting instantaneous frequencies is given.

2.2.3.1 Extraction of instantaneous frequencies

We will study the extraction algorithm originally developed by Delprat, Escudié *et al* in [45] to analyze musical sounds. The instantaneous frequency of a signal is defined as the maximum of the energy density function in the time–frequency domain. The energy density is equal to the scaled modulus of a continuous wavelet transform and is written as follows:

$$P_W f\left(u, \xi = \frac{\eta}{s}\right) = \frac{1}{s}|Wf(u,s)|^2. \tag{2.30}$$

The energy density function introduced here is also called the normalized scalogram, and it is symmetric with respect to $\xi = 0$ axis.

Definition. *At time $t = u$ the instantaneous frequency $\xi(u)$ of an analyzed signal $f(t)$ is obtained by calculating local maxima of the normalized scalogram* (2.30) *from the following two conditions:*

$$\frac{\partial}{\partial \xi} P_W f(u,\xi)|_{\xi=\xi(u)} = 0, \qquad \frac{\partial^2}{\partial^2 \xi} P_W f(u,\xi)|_{\xi=\xi(u)} = 0. \tag{2.31}$$

For a simple periodic signal of the form $f(t) = e^{i\omega t}$ the normalized scalogram is defined as:

$$P_W f(u,\xi) = 2\sigma\sqrt{(\pi)}e^{-\sigma^2\eta^2(\omega/\xi-1)^2} \tag{2.32}$$

and the instantaneous frequency is constant and is equal to ω.

In general, for a non–periodic signal at each fixed moment of time several maxima can be found on the time–frequency plane. The following theorem [14] provides an explicit form of the wavelet transform for a signal of the form:

$$f(t) = a(t)e^{\phi(t)}, \tag{2.33}$$

where $a(t), \phi(t)$ are time–dependent amplitude and phase of a signal respectively.

Theorem 2.2.3 *Given a signal $f(t)$ of the form* (2.33) *its continuous wavelet transform at point (u,ξ) can be written as follows :*

$$Wf(u,s) = \sqrt{2s\sigma}\pi^{1/4}a(u)e^{i\phi(u)}\left[e^{-(\eta-\phi'(u)s)^2s^2\sigma^2/2} + \epsilon\right], \tag{2.34}$$

where ϵ is a small term whenever amplitude $a(t)$ and phase $\phi(t)$ of a signal $f(t)$ vary slowly over the interval of time smaller or equal to the time resolution of the wavelet.

For the MG wavelet the time resolution interval is equal to $[-\delta/2, \delta/2]$, where $\delta = \sigma s/\sqrt{2}$. If the ϵ term in the sum is small then the instantaneous frequency of a signal $f(t)$ in (2.33) is $\xi = \phi'(t)$. Detailed derivation of the above result is given in Appendix A.

In the applications to multidimensional Hamiltonian systems one often encounters multi–component signals of the form:

$$f(t) = \sum_{i=1}^{N} a_k(t)e^{i\phi_k(t)}, \tag{2.35}$$

where $a_k(t), \phi_k(t)$ are the time–dependent amplitudes and phases of a multi–component signal $f(t)$. The results of the Theorem 2.2.3 could be applied to each single component $a_k(t)e^{i\phi_k(t)}$ of a signal $f(t)$ assuming that $a_k(t)$ and $\phi_k(t)$ vary slowly over the time window resolution of the wavelet localized on the time–frequency plane around a point $(u, \xi = \frac{\eta}{s})$. This means that for every k the following estimates must hold:

$$s\sigma\frac{|a_k'(t)|}{|a_k(t)|} \ll 1, \qquad s^2\sigma^2\frac{|a_k''(t)|}{|a_k(t)|} \ll 1, \qquad s^2\sigma^2\|\phi_k''(t)| \ll 1, \tag{2.36}$$

over the time interval $t \in [u - \delta/2, u + \delta/2]$. The wavelet transform for a multi–component signal is a sum of wavelet transforms of each single component of a signal. This is the consequence of the linearity property of the transform. The normalized scalogram can be written up to the lower order correction terms (see Appendix A) as follows:

$$\begin{aligned}\frac{\sqrt{\pi}}{2\pi\sigma}P_f(u,s) &= \sum_{j=1,n}|a_j(u)|^2 e^{(\eta-\phi_j'(u)s)^2\sigma^2} \\ &+ 2\sum_{j,k=1,n}|a_j(u)||a_k(u)|\cos(\phi_j(u)-\phi_k(u)) \\ &\times e^{-\{[\eta-\phi_j'(u)s]^2\sigma^2\}/2}e^{-\{[\eta-\phi_k'(u)s]^2\sigma^2\}/2}. \end{aligned} \tag{2.37}$$

The normalized scalogram at each point (u, s) is represented by the sum of peaks localized near the instantaneous frequencies $\phi_k'(u)$ and the interference terms. At time $t = u$ two frequencies can be distinguished on the time–frequency plane if the distance between each of them is greater than the bandwidth of the wavelet at time $t = u$:

$$|\phi_k'(u) - \phi_j'(u)| \geq \frac{\sigma_{fr}}{s}. \tag{2.38}$$

Substituting the value of the frequency resolution $\sigma_{fr} = 1/(\sigma s\sqrt{2})$ and the scale $s = \eta/\xi$ in (2.38) one obtains the bandwidth condition for the MG wavelet:

$$\frac{|\phi_k'(u) - \phi_j'(u)|}{|\phi_k'(u)^2|} \geq \frac{1}{\eta^2\sigma\sqrt{2}}. \tag{2.39}$$

Two spectral components $\phi_k'(u), \phi_j'(u)$ do not interfere with each other if both of them satisfy the bandwidth condition at each point (u, s). In order to satisfy simultaneously conditions (2.36) and (2.39) one has to chose a proper resolution of the wavelet in the time–frequency domain by adjusting free parameters σ and η. In our calculations we have used $\sigma = 10$ and $\eta = 6$.

2.2.3.2 Discrete wavelet transform algorithm

In practice wavelet transform is calculated for a discrete signal $x(t_k), k = 1, \ldots, N$, where $N = 2^m$. The frequencies scales are discretized using the dyadic sampling $s_{i,j} = 2^{i+j/n}$, where $i = 1, \ldots, m$ and $j = 1, \ldots, n$. Integers m and n are the discretization parameters similar to the number of octaves and the number of voices used for the analysis of musical

sounds [45]. Thus, we consider the discretization of a time–frequency plane defined by $2^m \times m \times n$ boxes. A relative error for the calculation of frequencies is $\Delta\omega/\omega = 1 - 2^{-1/n}$, and it is made small by choosing large number of voices n. The finer is the discretization of the time–frequency plane the better is the localization of the energy density.

The first step for the wavelet transform calculation is to compute its Fourier components, which are given for each frequency scale by the following expression:

$$\widehat{W}f(\omega, s) = \sqrt{s}\widehat{f}(\omega)\widehat{\phi}(s\omega). \tag{2.40}$$

In the next step the wavelet transform $Wf(u, s)$ can be recovered by the application of an inverse fast Fourier transform (FFT) algorithm. The total number of steps required to compute the discreet wavelet transform at every time $t = u$ is equal to the total number of scales $m \times n$ multiplied by the number of operations used for the FFT $O(2^m log_2 2^m)$. Hence, to calculate the wavelet transform for a discrete signal $x(t_k)$ one needs the total number of steps is of the order $O(nm^2 2^m)$ [14].

The wavelet method does not depend on dimension of an analyzed system. Therefore, it a very useful tool for studying multidimensional phase space structures that can not be recovered with the other existing methods, such as Poincaré surface of section. It can be used for periodic orbit search by localizing periodic and quasiperiodic structures in phase space of a system.

CHAPTER III

VIBRATIONAL DYNAMICS OF THE HIGHLY EXCITED PLANAR OCS MOLECULE

3.1 Introduction

Over the past decades the studies of classical dynamics of a highly excited planar carbonyl sulphide (OCS) molecule have let to a longstanding controversy in the community of chemical physicists. The main point of the controversy is the intrinsic mechanism of the intramolecular energy exchange. Traditional statistical theories, such as RRKM theory [46], fail to provide a realistic estimate on the intramolecular energy relaxation time. The classical model of the collinear and planar OCS systems was first studied by Carter and Brumer in [15]. These authors have found classically the evidence of a long–time energy redistribution among the vibrational modes of the system. These findings did not fit the theoretical predictions derived from the RRKM theory. The qualitative features of dynamics were studied by utilizing the nonlinear techniques for different energy regimes: from the low energies up to dissociation energies. By using Lyapunov exponent calculations for the microcanonical ensemble of phase space trajectories the authors in [15] discovered that chaotic behavior in the system dominates for the energy regimes close to dissociation.

In subsequent work, Davis *et al* [16] studied the classical dynamics in the phase space of collinear version of the OCS molecule. The long–time energy correlations were accounted for the trappings of chaotic trajectories in the vicinity of the unbroken invariant tori. These tori can serve as a partial barriers to the chaotic diffusion across the phase space of the collinear molecule. These are the tori with the most irrational frequency ratios that, as we know from the results of KAM–theorem [47], remain intact under a small perturbation of the Hamiltonian system. With the increase of perturbation some of the resonant tori in the vicinity of the KAM tori break up. Their broken structure creates sticky porous layers that

can serve as partial barriers for diffusion of chaotic trajectories across them.

According to the arguments given by Martens *et al* in [48, 49] for the planar OCS model the problem of intramolecular energy transfer is also related to the phase space resonant and non–resonant structures. Although many studies have been devoted to the intrinsic transport of chaotic trajectories in the phase space and its relevance to the intramolecular energy relaxation dynamics, the main question still remains open: What are the structures in the phase space of classical model of the planar OCS system that play a role of partial barriers to the diffusion of chaotic trajectories?

The classical model of the planar OCS is a three–dimensional Hamiltonian system. It is non–integrable for a highly excited energy regimes close to dissociation threshold. Apart from the energy integral there are no other integrals or intrinsic symmetries that would allow reduction of system's dimension. The phase space of a non–integrable Hamiltonian system represent a mixture of chaotic and regular regions. The study of a high–dimensional phase space is complicated since up till now there are very few numerical techniques known that can provide a complete qualitative view of the dynamics of the multidimensional system.

In the previous studies of the planar OCS model [49] the Local Frequency analysis was used to study chaotic transport and resonant structures. However, this technique does not allow following rapid transitions of the instantaneous frequencies, which are typical for the highly excited regimes of the system. The time–frequency analysis method based on wavelet decomposition was applied in [50]. In this work we propose to use time–frequency analysis in conjunction with the fast Lyapunov indicator method.

The results of this chapter are organized as follows. The classical model of the planar vibrational OCS is described in Section 3.2. Section 3.3 is devoted to the FLI stability analysis of the phase space structures of the planar OCS at energies below and at dissociation. We provide maps of stability that picture the global structure of the phase space at different energy regimes as well as classify the important stable structures, such as resonant regions and periodic orbits. We also discuss the characteristic features of system's behavior at the dissociation threshold. The application of the wavelet time–frequency analysis is discussed

in Section 3.4. We identify the important resonances and their role in the intramolecular energy exchange by studying spectral information obtained with the application of the wavelet analysis. Finally, the main conclusions are presented in Section 3.5.

3.2 The Hamiltonian

The classical model of the planar (rotationless) carbonyl sulfide OCS molecule has been studied in details in [15, 16, 48, 49]. The coordinates of this system are two interatomic distances $R_1 = d(C,S)$, $R_2 = d(C,O)$, the bending angle of the molecule $\alpha = \angle(O,C,S)$, and three momenta P_1, P_2, P_α which are respectively conjugate to R_1, R_2 and α. We notice that the third interatomic distance $R_3 = d(O,S)$ can be expressed as a function of R_1, R_2 and α:

$$R_3 = \left(R_1^2 + R_2^2 - 2R_1R_2\cos\alpha\right)^{1/2}. \tag{3.1}$$

The Hamiltonian for this system is written

$$H(R_1,R_2,\alpha,P_1,P_2,P_\alpha) = T(R_1,R_2,\alpha,P_1,P_2,P_\alpha) + V(R_1,R_2,\alpha), \tag{3.2}$$

where T is the kinetic part of the Hamiltonian and V is the potential part. The kinetic part has the form [15]

$$\begin{aligned} T &= \frac{\mu_1}{2}P_1^2 + \frac{\mu_2}{2}P_2^2 + \mu_3 P_1P_2\cos\alpha \\ &\quad + P_\alpha^2\left(\frac{\mu_1}{2R_1^2} + \frac{\mu_2}{2R_2^2} - \frac{\mu_3\cos\alpha}{R_1R_2}\right) - \mu_3 P_\alpha\sin\alpha\left(\frac{P_1}{R_2} + \frac{P_2}{R_1}\right), \end{aligned}$$

where μ_i are the reduced masses. The analytic expression of the potential has been proposed in [51] based on existing experimental data and is of the form:

$$V(R_1,R_2,\alpha) = \sum_{i=1}^{3} V_i(R_i) + V_I(R_1,R_2,R_3), \tag{3.3}$$

where V_i are Morse potentials for each diatomic pair

$$V_i(R) = D_i\left(1 - e^{-\beta_i(R-R_i^*)}\right)^2,$$

and V_I is the interaction potential of the Sorbie–Murrell form [15] given explicitly

$$V_I = P(R_1,R_2,R_3)\prod_{i=1}^{3}\left(1 - \tanh\gamma_i(R_i - R_i^{(0)})\right),$$

where $R_i^{(0)}$ are the equilibrium distances of the planar OCS, which is a collinear ($\alpha = \pi$) configuration: $R_1^{(0)} = 2.9508$ (in atomic units) $R_2^{(0)} = 2.2030$ and $R_3^{(0)} = R_1^{(0)} + R_2^{(0)}$. The function P is a quartic polynomial in each of its variables. All the coefficients of the potential can be found in [15].

The planar OCS is an example of a general triatomic molecule with three strongly coupled modes: CO and CS stretching modes, represented by the $R_1(t)$ and $R_2(t)$ interatomic distances, and a bending mode, represented by angle $\alpha(t)$. The Sorbie–Murrell interaction term and Morse potential introduce a strong coupling between all three modes. In fact, any perturbation introduced in one of the modes will be quickly redistributed among the two other modes. It was shown in Reference [15] that dynamics of the planar OCS system is irregular at energies close to the dissociation threshold at $E = 0.1$ (in atomic units).

3.3 Application of the Fast Lyapunov Indicator Method

3.3.1 Phase Space Structures via FLI Stability Plots

In order to examine the classical dynamics of the planar OCS model we chose an ensemble of initial conditions from the two–dimensional subspace of the phase space of the system. We chose the initial conditions subspace to be defined by the zero momenta condition $P_1 = P_2 = P_\alpha = 0$. The bending angle α can then be expressed from the energy integral of motion $E = V(R_1, R_2, \alpha)$. We have integrated Hamiltonian equations of motion together with the variational equations for a time $t = [0,\ 1]$ (the unit of time is one picosecond). The interval of time is chosen long enough for a system to show its characteristic dynamics. The integration was carried out using a standard variable order Runge–Kutta integrator. For our algorithm we use the definition of the fast Lyapunov Indicator given in Section 2.1 in equation (2.4). The equations of motion (2.1) were integrated along with the equations for the tangent vector of the flow (2.2). The results for the FLI curves evolution are shown in Figure 3.1 for four types of trajectories: strongly chaotic, weekly chaotic, quasiperiodic and periodic. All four trajectories are shown on Figure 3.2. It is seen from Figure 3.1 that after a short time of integration $t = [0,\ 1]$ all types of dynamical behaviors can be distinguished clearly. The FLI curve behaves almost linearly with time for chaotic trajectories (a) and

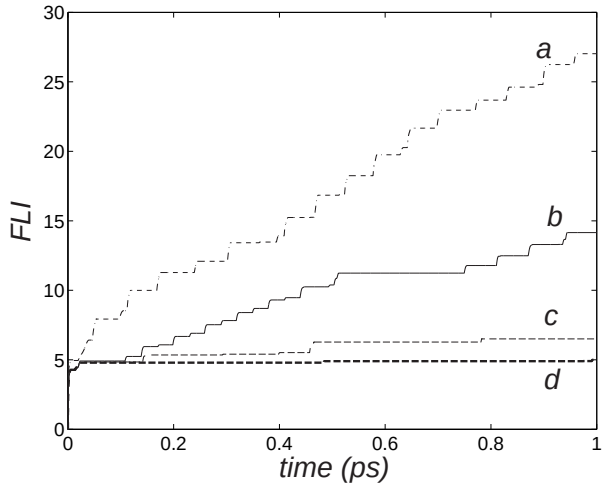

Figure 3.1: FLI curves versus time for the OCS for initial conditions in the configuration space with energy $E = 0.09$: for (a) a chaotic trajectory $(R_1, R_2) = (2.762, 1.911)$, (b) a weakly chaotic trajectory $(R_1, R_2) = (3.67, 2.307595)$, (c) a quasiperiodic trajectory $(R_1, R_2) = (3.65, 2.307595)$, (d) a periodic trajectory $(R_1, R_2) = (3.615178, 2.307595)$.

(b), and it shows logarithmic growth for quasiperiodic and periodic trajectories (c) and (d). This shows the power of the FLI method: not only it distinguishes between regular and chaotic behaviors but also between weakly and strongly chaotic trajectories after a short interval of time. In fact, for the periodic orbit shown in Figure 3.2 (d) with the period $T = 0.063$, the integration time $t = 1$ correspond to about 15 periods of oscillation of the molecule. By sampling a large number of trajectories from a given configuration subspace for different values of energies we found the maximum value of the FLI achieved over the interval of time $t \in [0,\ 1]$ is $\phi(1) < \phi_c, \phi_c = 10$ for regular trajectories sampled. At the same time the maximum value of the FLI is $\phi(1) \geq \phi_c$ for chaotic trajectories. This finding introduces an easy classification of the types of orbits studied. By knowing the final value of the FLI for each initial condition we can identify if a trajectory comes from chaotic or regular region of the phase space.

In order to obtain information about the global stability structures of the phase space the FLI calculations were carried out on a grid of $n \times m$ initial conditions from the zero–momentum subspace of configuration space. The subspace is spanned by two interatomic distances $R_1^i, i = 1, \ldots, n$ and $R_2^j, j = 1, \ldots, m$. Each trajectory from a grid of initial

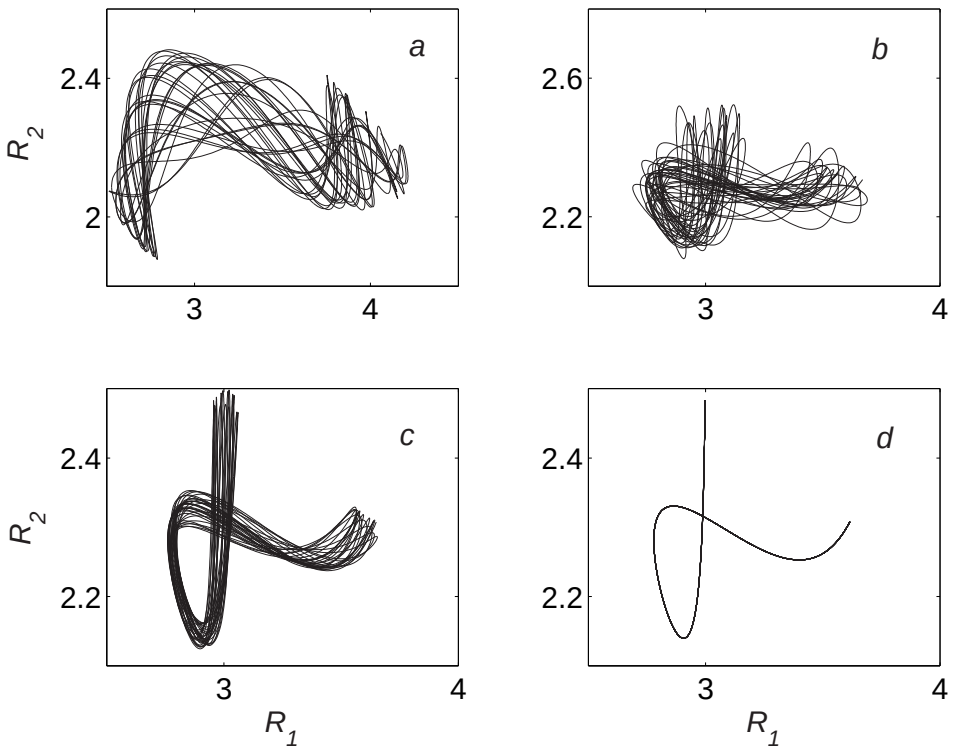

Figure 3.2: Trajectories in the configuration space for four initial conditions used in Figure 3.1. Trajectories (b) and (c) are chosen in the vicinity of the periodic orbit (d). Integration time $t = 1$.

conditions $(R_1^i(0), R_2^j(0), \alpha^{i,j}, 0, 0, 0)$ was integrated on time interval $t \in [0, 1]$. For every trajectory the evolution of tangent vector along the flow was calculated as well. We carried out FLI calculations for six different values of energy from the interval $[0.05,\ 0.1]$. The results are reproduced on Figure 3.3. The maximum values of FLI for each initial condition are color coded. Our calculations map a set of values of FLI on the $(R_1,\ R_2)$ plane. The blue color on Figure 3.3 represents initial conditions corresponding to regular trajectories and low values of the FLI. The yellow and red colors represent initial conditions corresponding to chaotic and strongly chaotic trajectories and high values of the FLI. From the FLI plots in Figure 3.3 we can observe the evolution of the global stability of the system as the energy is increased up to dissociation limit. The color scale is chosen the same for all the plots in order to see in a more clearer way the changes that occur in the dynamics of the system. For energy $E = 0.05$ the FLI field on (a) panel consists of the large dark region in the center that is associated with the resonant zone $\omega_1/\omega_\alpha = 2, \omega_2/\omega_\alpha = 2$, where ω_1, ω_2 and ω_α are the main frequencies of the signals $R_1(t) + iP_1(t), R_2(t) + iP_2(t)$, and $\alpha(t) + iP_\alpha(t)$, respectively. Most of the configuration space at this energy is constituted of quasiperiodic and periodic trajectories and the system is in a near–to–integrable regime. As energy is increased to $E = 0.06$ some regular motions lose stability and chaotic motions appear. This is seen on Figure 3.3 (b). We can notice the appearance of highlighted ridges surrounding the main resonance zone. They correspond to hyperbolic periodic orbits and indicate thin layers of chaoticity surrounding these orbits. These layers separate the main resonance zone from other higher order resonant zones. These plots do not provide the precise determination of all the intrinsic structures of the phase space due to finite resolution of the grid that we used. Choosing a higher-resolution grid one can get a very sharp determination of the corresponding structures in a given subspace of the phase space.

For the energies $E = 0.07$ and $E = 0.08$ the dynamics looks even more chaotic. It is seen on Figure 3.3 (c) and 3.3 (d) that the number of points with higher values of the FLI (the value of FLI reaches 22 for E=0.08) is increased. It can be seen that for energies $E > 0.07$ the central resonant island on (c) panel is split into two zones. These two stable zones correspond to resonance $\omega_1 : \omega_2 : \omega_3 = 1 : 4 : 1$. They remain stable for higher energies,

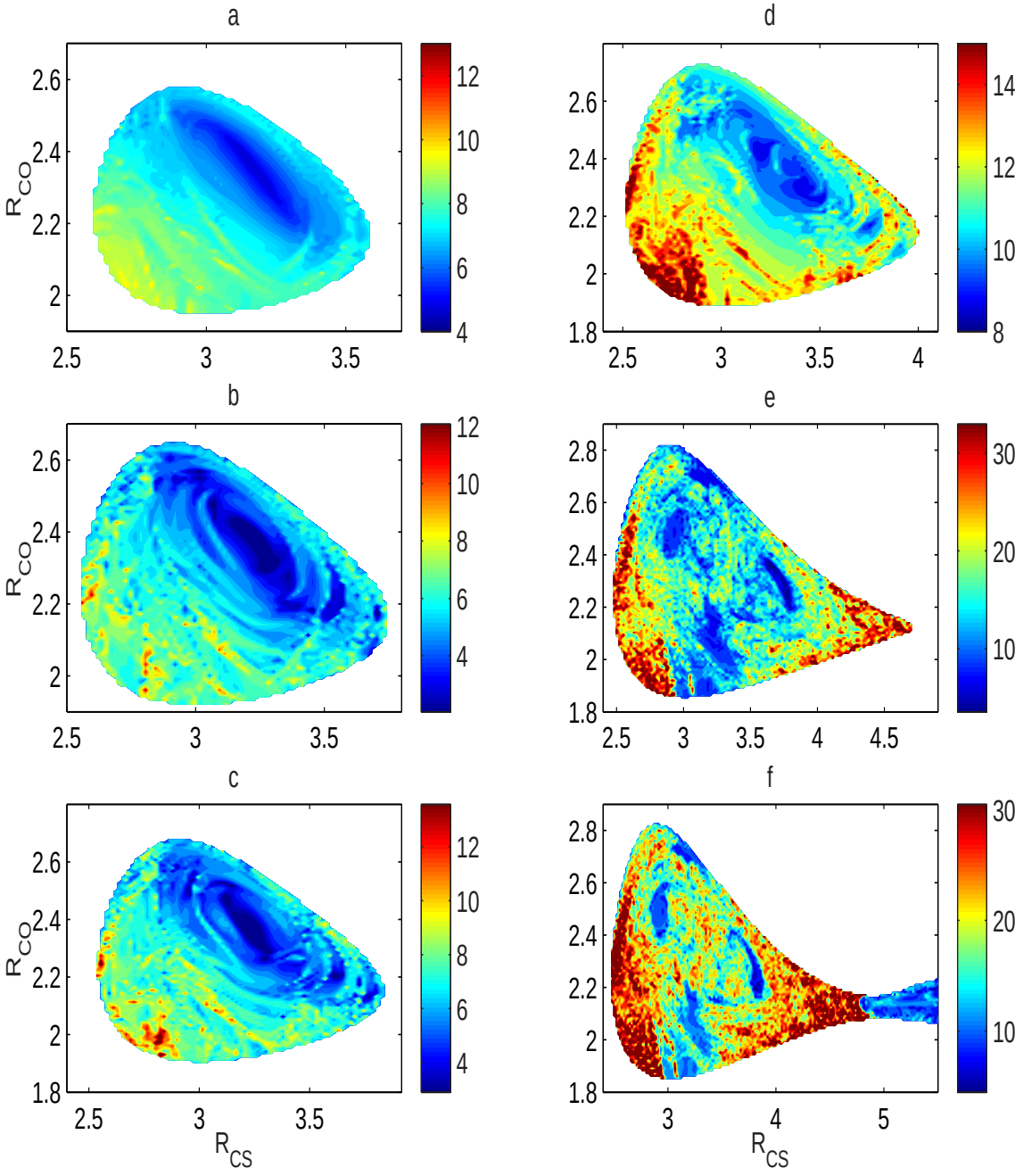

Figure 3.3: FLI plots for energies: a) 0.05, b) 0.06, c) 0.07, d) 0.098, e) 0.1

however, the size of the zones decrease substantially for these energies.

For energy $E = 0.098$ only a few regular regions inside the phase space survive (see Figure 3.3 (e)). They are surrounded by a large set of initial conditions corresponding to chaotic motions. All the surviving resonances can be identified by using time–frequency analysis described in Section 2.2. Since most of the trajectories within regular parts of the phase space are quasiperiodic, the time–frequency method guarantees an accurate determination of all the main frequencies of trajectories from a given resonance zone. The results of the time–frequency analysis are presented in Section 3.4.

It is easy to observe that at the energy equal to dissociation $E = 0.1$ (see Figure 3.3 (f)) most of the configuration space is filled with initial conditions corresponding to strongly chaotic trajectories. The main feature of this plot is the existence of stable structures at dissociation energy where the system's behavior is predominantly chaotic. Our calculations at energy $E = 0.1$ shows that the values of the FLI computed for chaotic trajectories in most cases exceed 16 and percentage of regular trajectories is below 13%.

3.3.2 Periodic Orbits Analysis

An extensive research of multidimensional Hamiltonian systems carried out over the past decades [3, 9, 19, 41, 44] shows that much of the phase space dynamics is determined by stable invariant structures, such as resonant tori, periodic orbits and stable and unstable manifolds of these invariant objects.

We perform the periodic orbit search for the planar OCS system by using a variational method proposed by Lan and Cvitanović in [52]. Its purpose is to provide a very robust determination of the periodic orbits even for high dimensional deterministic systems. In this section we briefly describe the method and present the results for the periodic orbits search for different energy regimes of the OCS system.

To insure a good convergence of the algorithm described here one needs to initiate the search by picking a point from the configuration space that is close enough to the periodic trajectory. In this way, the results of the stability obtained with the FLI calculations in the previous Subsection 3.3.1 can guide the search for the periodic solutions: by choosing initial

condition inside one of the regular resonant zones indicated on the FLI plots in Figure 3.3 one can obtain an initial orbit close enough to the periodic solution sought.

We initialize the search by choosing a point from the configuration subspace and integrating the system of Hamiltonian equations for the planar OCS system. We take $R_1 = 3$ to be our Poincaré section by noticing that most of the time the orbit intersects this hyperplane. The flow becomes a map on the Poincaré section. As the symbolic dynamics is yet unexplored, to obtain cycles of different topological length, we look for the near recurrence of the map on the section for one iteration, two iterations, three iterations, etc. The resulting orbit segment is represented by a discrete set of points and its frequency components are obtained by a Fast Fourier Transform. After removing the high–frequency part, we transform the data back to the phase space and obtain a closed smooth loop. This serves as our starting guess for a periodic orbit. A Newton descent flow will drive the orbit towards a genuine periodic orbit by penalizing the discrepancy between the approximate flow and the true flow along the loop [52]. Table 1 lists several of the elliptic periodic orbits that have been obtained using the method for energy $E = 0.09$: for each periodic orbit two projections are given, one on the plane (R_1, P_1) and the other on the plane (R_2, P_2), the period T in picosecond and the frequency ratio $m : n : k$. By using the time–frequency analysis method (see Section 2.2) three main frequencies ω_1, ω_2 and ω_3 of the signals $z_1(t) = R_1 + iP_1$, $z_2(t) = R_2 + iP_2$ and $z_3 = \alpha + iP_\alpha$ were computed. The integers m, n, k are the ratio between the frequencies such that $\omega_1/\omega_2 = m/n$, $\omega_2/\omega_3 = n/k$. Most of the identified periodic orbits intersect the configuration space (R_1, R_2) at two points. We mark their intersection on the FLI plot on Figure 3.4 with crosses and circles according to stability properties of the orbit: elliptical periodic orbits are marked with circles and hyperbolic orbits are marked with crosses. Most of the elliptical periodic orbits are located in the center of configuration space inside the stable zones indicated by the low values of FLI. Most of the hyperbolic periodic points are located at the boundary of the configuration space and in the regions of the phase space where the FLI values are above the critical ϕ_c value. These results demonstrate a good sensitivity of the FLI method. It is able to distinguish well narrow layers of stochasticity surrounding the hyperbolic points in the phase space of the system. The

Table 1: Characteristics of the main elliptic periodic orbits: two projections on the planes (R_1, P_1) and (R_2, P_2) are given. We also provide the period T expressed in picoseconds and the two points which are the intersections of the orbits with the configuration space.

Name	Projection (R_1, P_1) and (R_2, P_2)	T (ps)	(R_1, R_2)	$m : n : k$
O_a	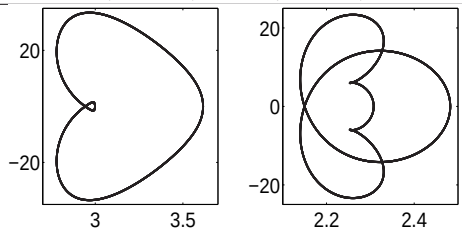	0.063	(3.615178, 2.307595) (2.998235, 2.482408)	1 : 1 : 1
O_b	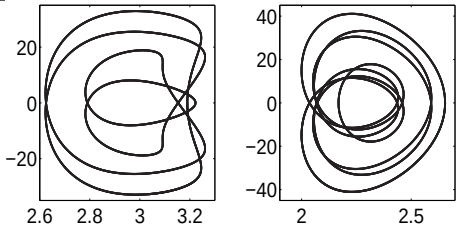	0.122	(3.189711, 2.654841) (3.222491, 2.168308)	2 : 3 : 1
O_c	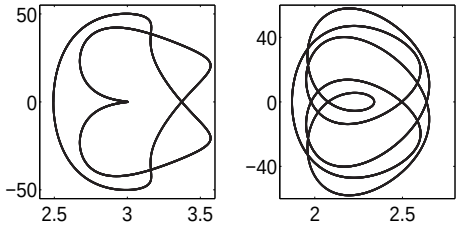	0.087	(2.493375, 2.339454) (3.002806, 1.869968)	2 : 2 : 1
O_d	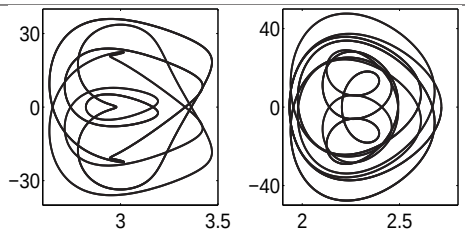	0.195	(2.821580, 2.714920) (2.978729, 2.203665)	4 : 11 : 3
O_e	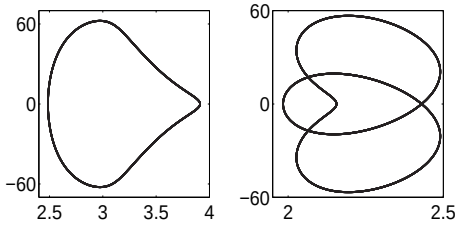	0.049	(3.911413, 1.983623) (2.485514, 2.155984)	1 : 1 : 0

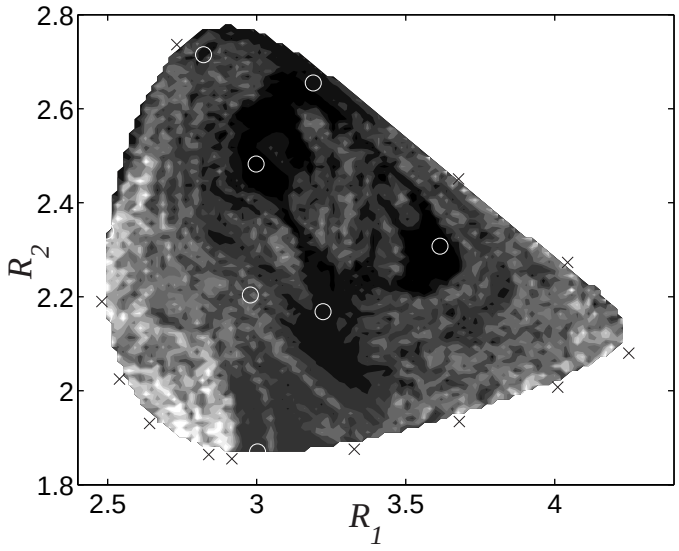

Figure 3.4: Intersections of the main periodic orbits marked on the FLI plot for the energy $E = 0.09$.

hyperbolic orbits that are situated at the boundary of the configuration space are collinear orbits: α bending mode is fixed ($\alpha = \pi, P_\alpha = 0$) and CO and CS stretching modes vibrate at the same frequency.

3.3.3 Dynamics near the Dissociation Threshold

It is apparent from the FLI plot for dissociation energy on Figure 3.3 (f) that around the interval $R_1 = [4.7,\ 4.8]$ the region with high values of the FLI is sharply jointed to the region with low values of the FLI. This abrupt variation in the FLI values is found near the saddle point ($R_1 = 4.9786,\ R_2 = 2.1689,\ \alpha = \pi,\ P_1 = P_2 = P_\alpha = 0$) in the vicinity of transition to dissociation region. The intrinsic topology of this region determines a high dimensional subspace that separates bounded motions from the motions close to dissociation. The projection of this subspace on the $x - y$ plane is visible on the FLI plot and is indicated by the sharp change in the FLI values across it. Trajectories chosen from the left side (red zone) of the dividing surface are strongly chaotic whereas trajectories with initial conditions chosen from the right side of dividing surface (dark blue zone) behave almost regularly and the FLI value are very low for this region of the configuration space. In particular, there are two types of trajectories that one can find on the right side of the dividing surface in

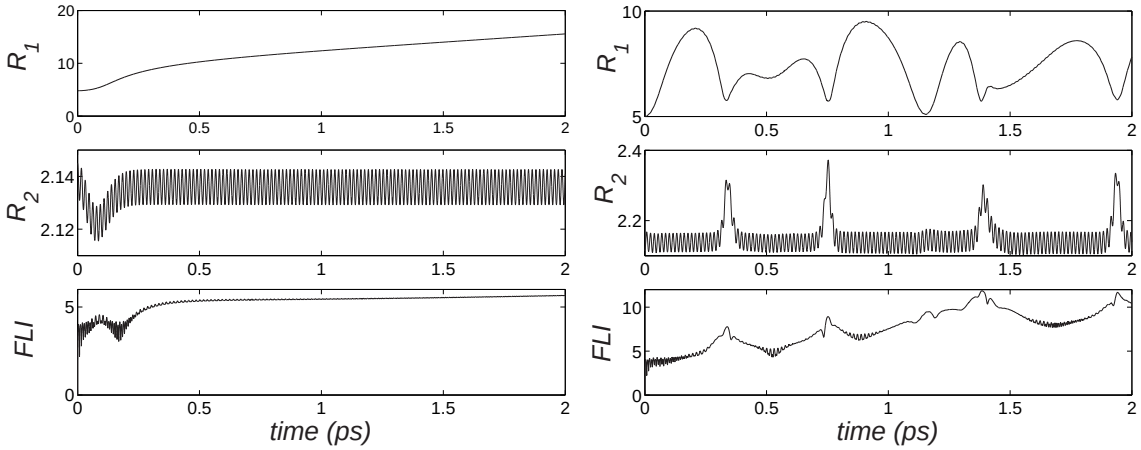

Figure 3.5: (Left) Time series for R_1, R_2 and FLI evolution for a trajectory at dissociation energy $E = 0.1$. Initial condition from the configuration space: $R_1 = 4.8, R_2 = 2.145$. (Right) The same for trajectory with initial conditions $R_1 = 5.02, R_2 = 2.11$.

the configuration space. To explain these two types of behaviors we reproduce the time series and FLI evolution for trajectories initiated from both sides of the dividing surface. The time series for R_1 and R_2 together with the FLI evolution for the dissociating motion are shown on the left panel of Figure 3.5 on the left panel. As the S atom moves away from the CO bond. For large R_1 the interaction term in the potential energy expression (3.3) corresponding to CS and SO interaction is small. As a consequence the remaining C and O atoms vibrate only under the influence of the CO Morse potential $V_2(R_2)$. In this case the dynamics of the system is regular and the FLI curve follows almost logarithmic growth with time. It results in the low value of the maximum of the FLI attained over the integration period $t = [0, 1]$.

Another type of dynamical behavior for trajectories chosen from the left side of the dividing surface ($R_1 > 4.8$) is shown on the right panel of Figure 3.5. Here the time–series for R_1 and R_2 distances demonstrate an intermittent behavior. During intervals of time, when the distance R_1 is large and the S atom is far away from the CO bond the dynamics looks regular and the FLI evolution shows almost logarithmic behavior with time. The intervals of regular behavior are interrupted by high amplitude peaks seen on the right panel in Figure 3.5 for the R_2 time series. These peaks occur at moments of time when the S atom approaches the CO bond. The evolution of the FLI shows an intermittent behavior

as well. The fast growth of the indicator is observed at the moments of time when R_1 decreases whereas almost logarithmic growth is seen when the behavior of the system is regular. As a result the maximum value of the FLI attained over the integration interval $t = [0,\ 2]$ is low as in the case of dissociation.

The dissociation energy regime is a non–integrable limit of the classical system of the planar OCS model. The phase space at dissociation threshold is predominantly chaotic, and stochastic diffusion of bounded chaotic motions is mediated by the resonant structures that remain stable. For the motions near to dissociation region the behavior is defined by the intrinsic topology of the transition state. Choosing initial condition from the region with the high values of FLI (left side of the dividing surface) we obtain bounded motion that corresponds to chaotic interaction of the three strongly coupled vibrational modes of the OCS molecule. Initial conditions chosen from the region with the low values of FLI (right side of the dividing surface) lead either to dissociation of the molecule or to the intermittent regime. The intermittent regime is characterized by small amplitude regular vibration in the CO mode interrupted by short–time irregular vibrations accompanied with the contraction of the CS bond. In the phase space this intermittent behavior corresponds to the recrossing of transition to dissociation state.

A good knowledge of the dynamics at the transition state is potentially important for understanding of the mechanism of chemical dissociation. The detailed study of the transition state is not within the scope of the results presented here and we plan to develop it in our future work.

3.4 Application of the Time–Frequency Wavelet Analysis

3.4.1 Time–frequency Planes

The Morlet–Grossman wavelet analysis was first applied to molecular dynamics in [5, 50]. The resonance structure of the highly excited planar OCS system was studied by analyzing instantaneous frequency of the phase space trajectories. For a given trajectory the instantaneous frequency was found by locating the local maxima of the scalogram obtained with the MG wavelet transform (see Section 2.2.3). The intervals, where the set of instantaneous

frequencies of the three vibrational modes remain almost constant, indicate the trappings of trajectory near to some resonant zone. In [5, 50] the important transitions and trappings of trajectories were localized using spectral information provided by calculation of the main frequency only. However, for a highly chaotic system one can not restrict the calculations to only one main frequency; this results in misleading information about the resonance transitions for strongly chaotic trajectories as well as in the loss of the other important spectral information for a trajectory. Recently another approach to study chaotic Hamiltonian dynamics was used by Chandre *et al* in [44]. Chaotic dynamics was characterized by identifying all the local maxima or "ridges" of time–frequency landscape given by the normalized scalogram. The MG wavelet algorithm was applied for the Standard map [30] and the classical model of the hydrogen atom inside elliptically polarized fields. By studying variations of the instantaneous frequency curves on time–frequency plane for various types of trajectories the long–time trappings were detected and the degree of chaoticity for every trajectory at each moment of time was characterized. Based on the results of the time–frequency analysis the authors in [44] concluded that strongly chaotic behavior is characterized by a number of multiple short ridges on time–frequency plane meanwhile local resonant trappings are characterized by a single ridge or a few ridges that are almost constant over the interval of trappings. Thus, the time–frequency information obtained from the wavelet decomposition of a single trajectory can reveal all the invariant phase space structures visited by this trajectory and characterize the type of trajectory behavior.

Our main interest in the application of time–frequency wavelet analysis to the OCS system is to locate the invariant structures within the phase space that can serve as partial barriers to the chaotic transport across them. We use time–frequency algorithm proposed in [44]. Our calculations confirm the results presented in [50] energy of 90% of dissociation energy. In addition, we carry out time–frequency analysis for the other energies of the OCS system. Time–frequency wavelet analysis was applied to a set of quasiperiodic, weakly chaotic and chaotic trajectories of the planar OCS at the energies $E = \{0.08;\ 0.09;\ 0.1\}$. It was shown in Section 3.2 that system's dynamics becomes more chaotic as the energy approaches the dissociation threshold. For the energy $E = 0.08$ the resonant structures

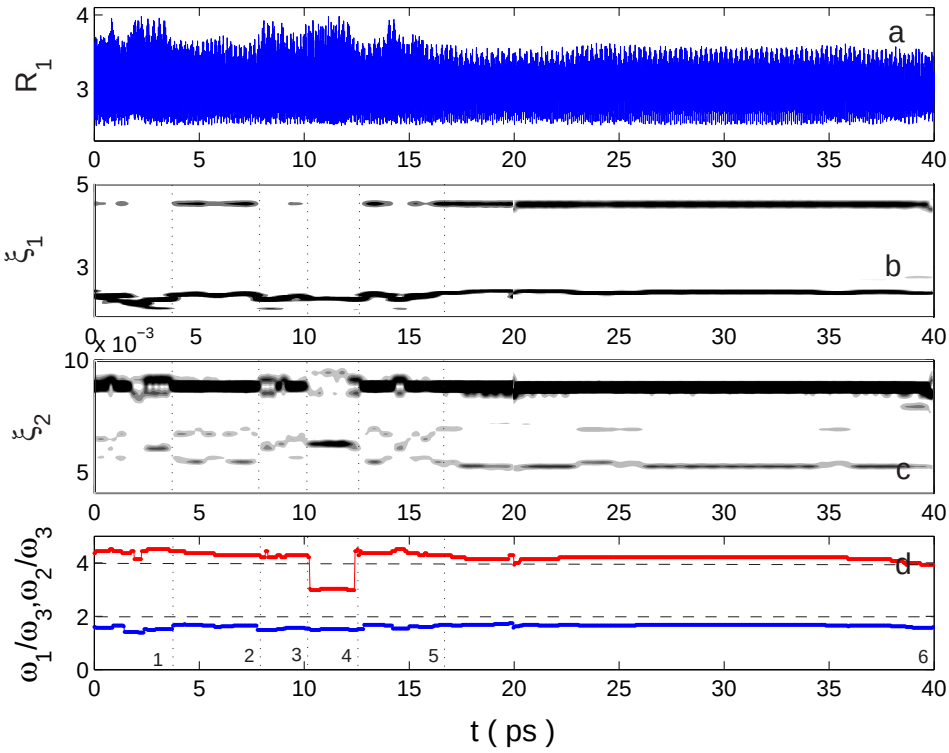

Figure 3.6: Time–frequency decomposition for a chaotic trajectory. Initial conditions are: $R_1 = 2.8,\ R_2 = 1.93$. $E = 0.08$. On (d) panel red color curve is plotted for frequency ratio ω_2/ω_3 and blue color curve is plotted for frequency ratio ω_1/ω_3.

occupy large part of the phase space and the remaining part of the phase space is chaotic. For the energy $E = 0.09$ stable resonant zones are isolated in the phase space. They are surrounded by the large chaotic area. The phase space of the system at dissociation energy $E = 0.1$ is predominantly chaotic. We view dynamics on the time–frequency domain and characterize the behavior of the instantaneous frequencies of chaotic trajectories at different energy regimes of the system.

For each of the studied trajectories the magnitude of the normalized scalogram $P_w f(t, s)$ was computed on a mesh of points $(t_n,\ s_m)$, where t_n is time and s_m is the scale of a discreet MG wavelet transform. The resulting matrix $n \times m$ was presented on time–frequency plane defined by the sets of points $(t_n,\ \xi_m = \eta/s_m)$. Time–frequency wavelet transform was carried out for each vibrational mode of the OCS system.

In Figure 3.6 we present results for time–frequency decomposition of a weakly chaotic trajectory of the OCS system at the energy $E = 0.08$. On the upper panel (a) the time

series for the CS distance is plotted. The integration time is an interval $t = [0,\ 40]$ ps. The time–frequency decompositions for CS and CO vibrational modes are pictured on (b) and (c) panels. The locations of the instantaneous frequencies on time–frequency planes are indicated by a set of dark lines, which are called ridges or maxima of the normalized scalogram. Several ridges of different intensities can be present at the same time. The darker ridges indicate high magnitude of the scalogram computed at the location of the ridges while the lighter ridges indicate small magnitude of the scalogram. By calculating the maximum of the normalized scalogram at each fixed moment of time we find the fundamental frequencies $\omega_1,\ \omega_2,\ \omega_3$ for all the vibrational modes. The ratios of the fundamental frequencies versus time are shown on (d) panel. From Figure 3.6 it is easy to notice that the trajectory is weakly chaotic during the interval of time $t = [0,\ 17]$ and is almost regular for $t > 17$. The trajectory stays most of the time inside the region surrounding the resonance $\omega_1 : \omega_2 : \omega_3 = 25 : 63 : 15$. At the time $t \simeq 10$ ps it undergoes short passage to the resonant zone $8 : 15 : 5$, and at time $t \simeq 13$ jumps back into the resonant zone $25 : 63 : 15$. On time–frequency plane resonant trapping of the trajectory is indicated by a finite set of ridges that do not change during the interval of trapping. It follows that instantaneous frequencies of the trajectory remain constant during the interval of trapping. For example, in Figure 3.6 (d) there are several regions where frequencies remains nearly constant. From (b) panel one observes the splitting and overlapping of parallel ridges that happen at the subsequent transitions along the intervals: from 2 to 3, from 3 to 4, and from 4 to 5. On each interval of time there are three distinct ridges. As trajectory passes from interval 3 to 4 the dark ridge splits into two light ridges. The opposite transition happens when trajectory passes from interval 4 to 5. Two ridges are seen to emerge at time $t = 12.5$. This behavior of the ridges results from the passages of chaotic trajectory inside the phase space from the primary resonant torus to the secondary tori that are spiraling around it.

Another example of time–frequency decomposition is shown in Figure 3.7. There is a weakly chaotic trajectory that starts within the resonant zone given by the frequency ratios: $18 : 45 : 10$. As can be seen from time–frequency planes, trajectory remains most of the time inside the zone except during short intervals of time when trajectory diffuse to the nearby

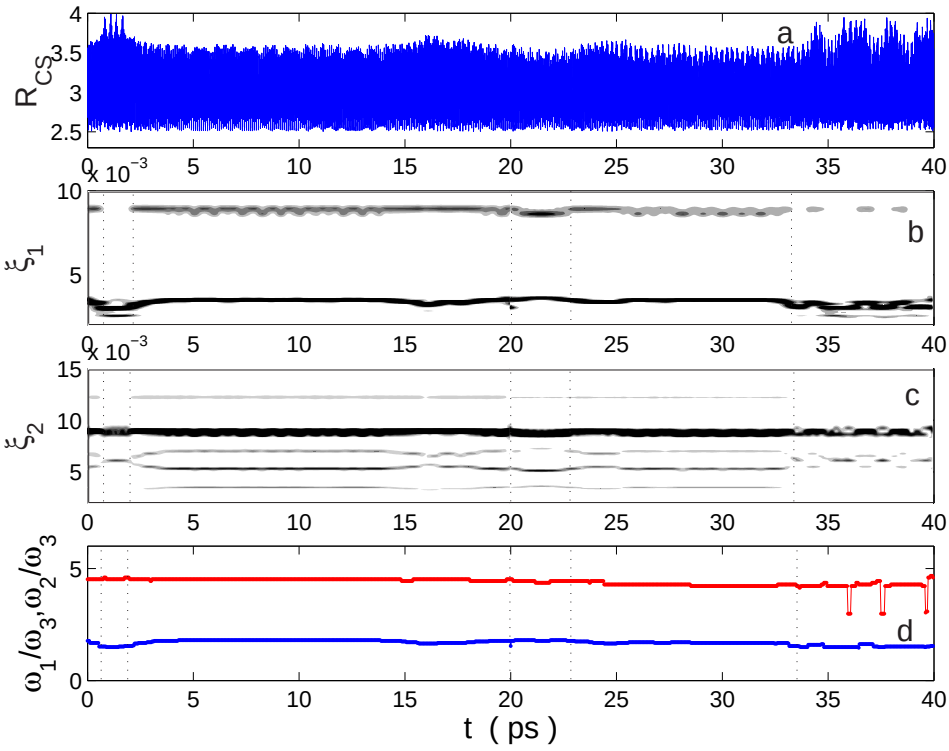

Figure 3.7: Time–frequency decomposition for a weakly chaotic trajectory. Initial conditions are: $R_1 = 2.9,\ R_2 = 1.91.\ E = 0.08$.

resonances. The passages to the neighboring resonant zone $25 : 63 : 15$ happens at times $t = 2$ and $t = 33$. Another fast transition can be observed at time $t = [20,\ 23]$. The behavior of trajectory during the intervals corresponding to the resonant trappings is regular. In Figure 3.8 the trajectory starts within the resonance $2 : 2 : 1$ and undergoes sequence of transitions to the following in dynamics resonant zones. The first transition, from $2 : 2 : 1$ to $4 : 7 : 2$ resonance, happens along the resonance channel; one of the frequency ratios remains constant during the transition. From Figure 3.8 (d) one observes a sequence of transitions along the resonance channel over the interval of time $t = [25,\ 40]$. Meanwhile the ω_1/ω_3 frequency ratio curve (blue color) remains fixed around 1.34, the ω_2/ω_3 frequency ratio curve (red color) exhibits several jumps over the interval considered. An interesting feature of the frequency dynamics can be observed from time–frequency planes for CS and CO vibrations (b and c panels). The ridges corresponding to the instantaneous frequencies for the CS mode vary smoothly with time and show slow variations in the slope and in the magnitude. A very different behavior of the ridges is observed from time–frequency plane

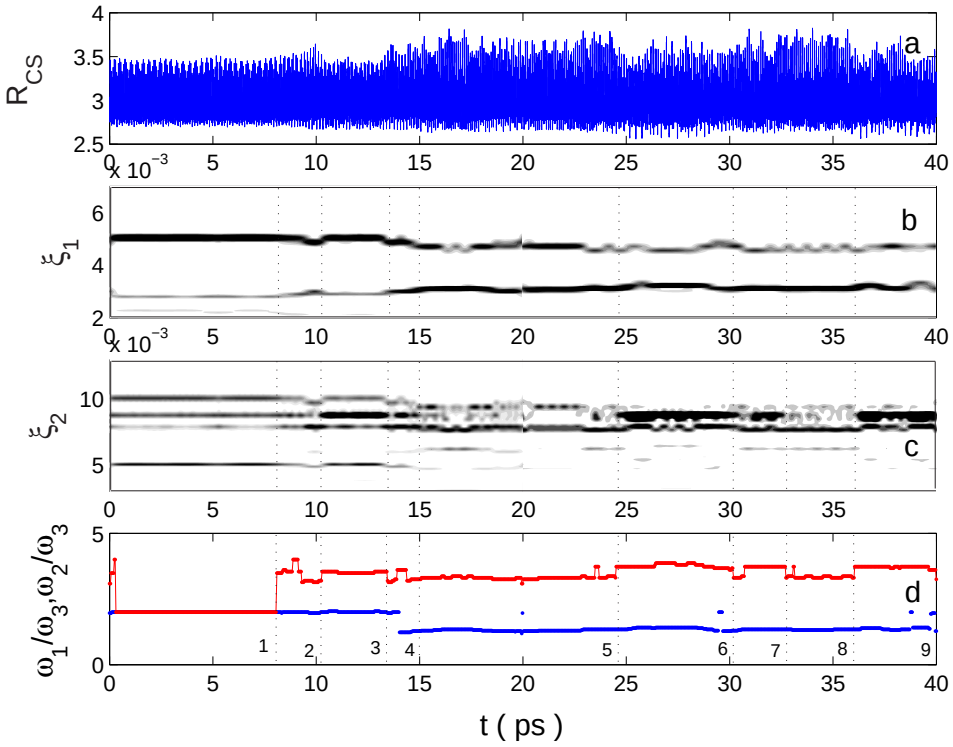

Figure 3.8: Time–frequency decomposition for a weakly chaotic trajectory. Initial conditions are: $R_1 = 3,\ R_2 = 2.54.\ E = 0.08$.

((c) panel) for the CO mode. The amplitude of the normalized scalogram along the ridges show significant variations from one trapping interval to the other. The dynamics of the system in this case is governed by the chaotic excitations within the CO vibrational mode.

From the data presented in Figures 3.6–3.8 we observe that time–frequency plane for a weakly chaotic trajectories consists of a finite set of ridges. Each ridge corresponds to a single frequency component of an analyzed trajectory and varies smoothly with time. The number of ridges is equal to the number of frequencies associated with the resonant zones where trajectory is trapped. The amplitude of the normalized scalogram computed along the ridge is also a function of time. If a trajectory is trapped around a resonance then its instantaneous frequencies remain constant or fluctuate around constant value during the interval of trapping. On time–frequency plane ridges of scalogram might vanish and appear according to the variation of the amplitude of normalized scalogram at the points along the ridges.

The following examples demonstrate time–frequency decomposition data for trajectories

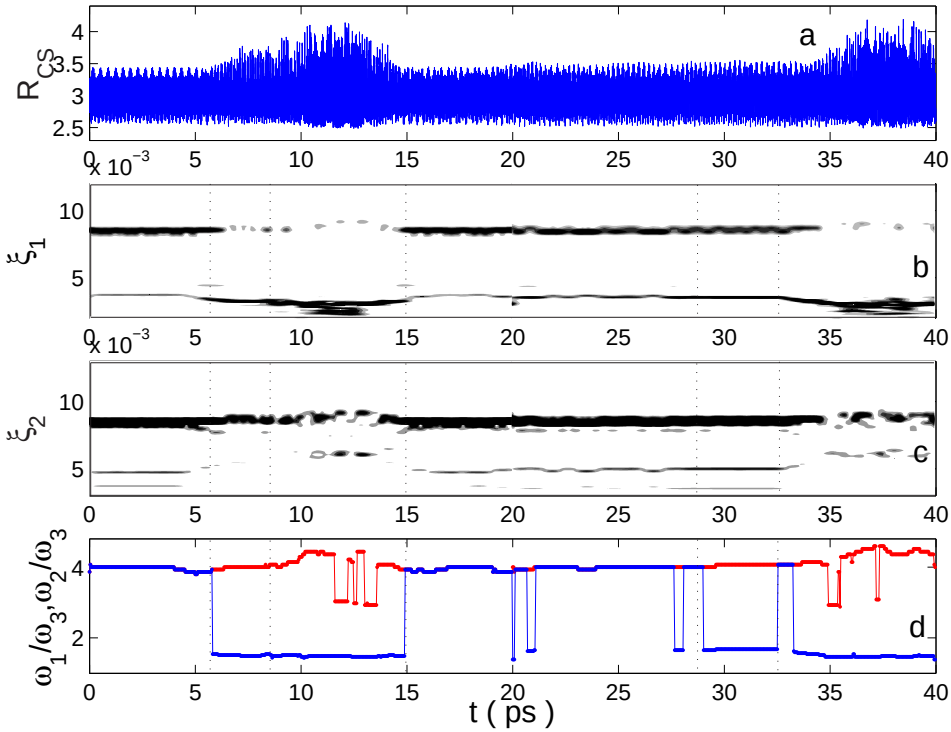

Figure 3.9: Time–frequency decomposition for a weakly chaotic trajectory. Initial conditions are: $R_1 = 3.2,\ R_2 = 1.98.\ E = 0.09$.

at energy $E = 0.09$ with different stability properties. We chose initial conditions from different regions of the phase space corresponding to different dynamical behaviors (see FLI plots in Figure 3.3). One example of time–frequency decomposition for a trajectory chosen from a chaotic zone of the phase space is presented on Figure 3.9. In this case all the transitions happen between three zones: two resonant zones and one chaotic zone. Chaotic regions can be distinguished on time–frequency planes for CS and CO modes (b and c panels) by the appearance of multiple short ridges that exhibit rapid temporal variations. The trajectory starts initially inside the resonance $4:4:1$. At time $t \simeq 5$ ps it enters the resonance $3:8:2$, where it stays for a short time and exits to a chaotic region at time $t \simeq 10$ ps, where it undergoes subsequent rapid transitions. At time $t = 15$ trajectory enters resonance $4:4:1$ and remains trapped there for almost 14 ps. Later at time $t \simeq 29$ trajectory jumps again to $3:8:2$ resonant zone and diffuses to chaotic zone at $t = 35$.

Another interesting example of time–frequency decomposition for a chaotic trajectory is shown on Figure 3.10. In the first half of the integration interval trajectory undergoes

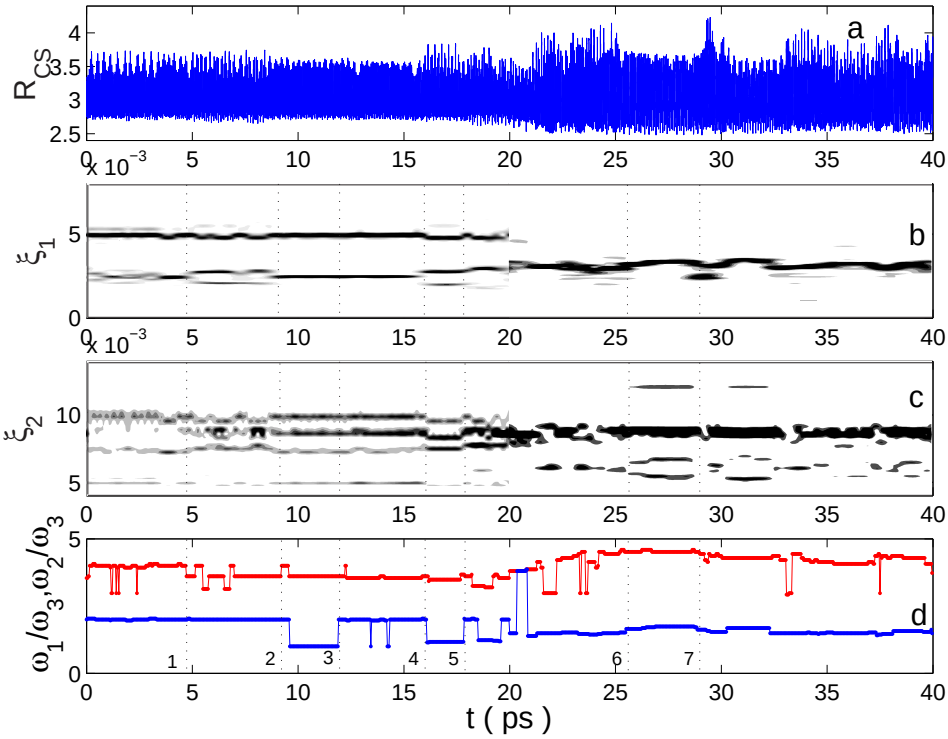

Figure 3.10: Time–frequency decomposition for a weakly chaotic trajectory. Initial conditions are: $R_1 = 3.28, R_2 = 2.4$. $E = 0.09$.

successive transitions between the following three resonant zones marked on (d) panel as follows: 1) $2:4:1$, 2) $10:18:5$, 3) $5:18:5$. At time $t \simeq 17$ trajectory enters a chaotic zone: its instantaneous frequency curves show very irregular behavior. One does not observe smooth behavior of ridges typical for the regular trajectories: a set of ridges appear and disappear abruptly and the magnitude of the normalized scalogram for each ridge changes fast with time. In this case the Theorem 2.2.3 is not applicable. The reason is, that during the time interval when trajectory is inside strongly chaotic region of the phase space, its instantaneous frequencies are not well defined and spectral changes happen much faster than the time–resolution of the wavelet.

In Figures 3.11 and 3.12 time–frequency decompositions are presented for two trajectories with initial conditions located in the nearby resonant zones inside the phase space. The first trajectory depicted on Figure 3.11 is a quasiperiodic with the frequency ratios $4:4:1$. It has two instantaneous frequencies for the CS and CO vibrational modes which are constant over the integration time interval. The second trajectory shown on Figure 3.12

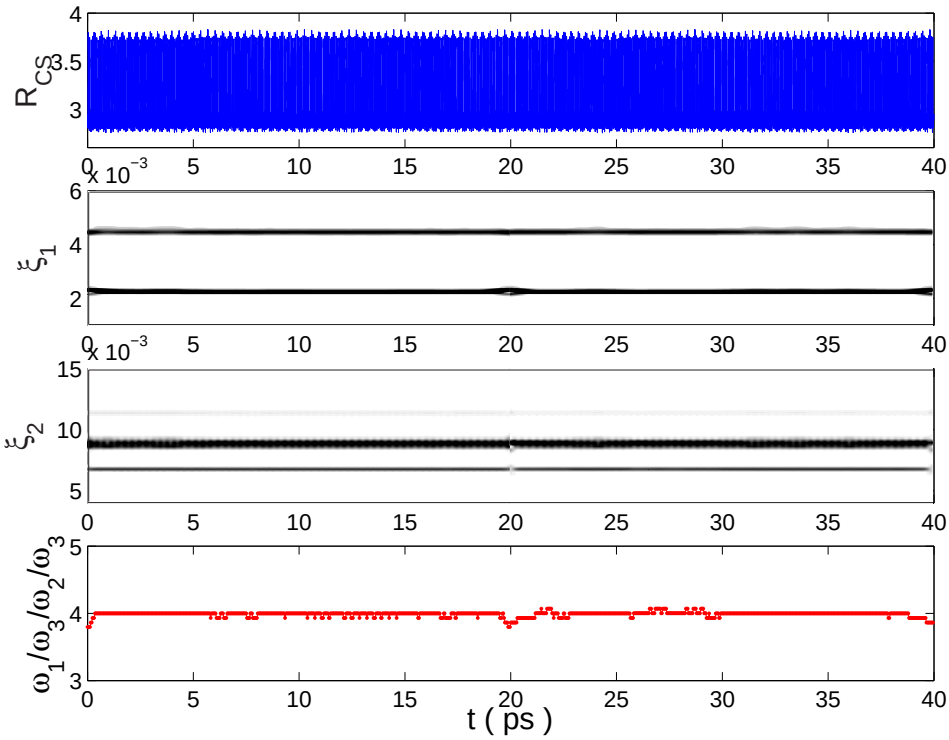

Figure 3.11: Time–frequency decomposition for a quasiperiodic trajectory. Initial conditions are: $R_1 = 2.95, R_2 = 2.4$. $E = 0.1$.

is a chaotic trajectory. It begins inside the resonant region $1:4:1$ and remains trapped in the vicinity of this resonance during the time interval $t = [0,\ 19]$. Upon exiting from the resonant zone at $t \simeq 20$ trajectory enters chaotic region. On (b) and (c) panels of Figure 3.12 chaotic zone is indicated by rapidly changing ridges.

The results of time–frequency decompositions for all examples discussed above are listed in Table 2. The approximate values of the instantaneous frequencies are calculated for all the important resonant trappings that are found on time–frequency planes. In the Section 2.2 it was pointed out that the MG wavelet decomposition determines frequencies with a relative error $\Delta\omega/\omega = 1 - 2^{-1/n}$, which depends on discretization parameter n of time–frequency plane. The ratios of the frequencies presented in the table are determined up to a constant δ due to an error in defining the exact frequencies. In fact, the frequency ratios satisfy the following inequality:

$$|\omega_1/\omega_3 - m/k| < \delta, \qquad |\omega_2/\omega_3 - n/k| < \delta, \tag{3.4}$$

where $\delta = 0.01$, m,n,and k are integer numbers.

Table 2: Table of resonances. Data are given in atomic units. The frequency ratios satisfy the conditions: $|\omega_1/\omega_3 - m/k| < 0.01,\ |\omega_2/\omega_3 - n/k| < 0.01$.

Energy	(R_1, R_2)	$\omega_1 \times 10^3$	$\omega_2 \times 10^3$	$\omega_3 \times 10^3$	$m : n : k$
0.08	$(3, 2.54)$	5.05	5.05	2.525	$2 : 2 : 1$
		5	8.75	2.500	$4 : 7 : 2$
		3.1	7.8	2.364	$13 : 33 : 10$
		3.2	8.88	2.370	$27 : 75 : 20$
	$(2.9, 1.91)$	3.6	9	2.000	$18 : 45 : 10$
		3.5	8.8	2.100	$25 : 63 : 15$
	$(2.8, 1.93)$	3.5	8.8	2.100	$25 : 63 : 15$
		3.4	6.2	2.100	$8 : 15 : 5$
0.09	$(3.2, 1.98)$	8.5	8.5	2.125	$4 : 4 : 1$
		3.5	8.5	2.060	$3 : 8 : 2$
	$(3.26, 2.63)$	5	8.6	2.460	$4 : 7 : 2$
		2.8	8.3	2.300	$6 : 18 : 5$
	$(3.4, 2.15)$	8.5	8.5	2.125	$4 : 4 : 1$
		4.8	8.7	2.400	$10 : 18 : 5$
		2.85	8.6	2.400	$6 : 18 : 5$
	$(3.28, 2.4)$	5	10	2.500	$2 : 4 : 1$
		5	9	2.500	$10 : 18 : 5$
		2.5	9	2.500	$5 : 18 : 5$
		2.8	8.4	2.400	$12 : 35 : 10$
		3.5	8.6	2.050	$17 : 42 : 10$
		3.2	8.6	2.150	$3 : 8 : 2$
0.1	$(2.95, 2.4)$	2.225	8.9	2.225	$1 : 4 : 1$
	$(2.93, 2.4)$	8.5	8.5	2.125	$4 : 4 : 1$

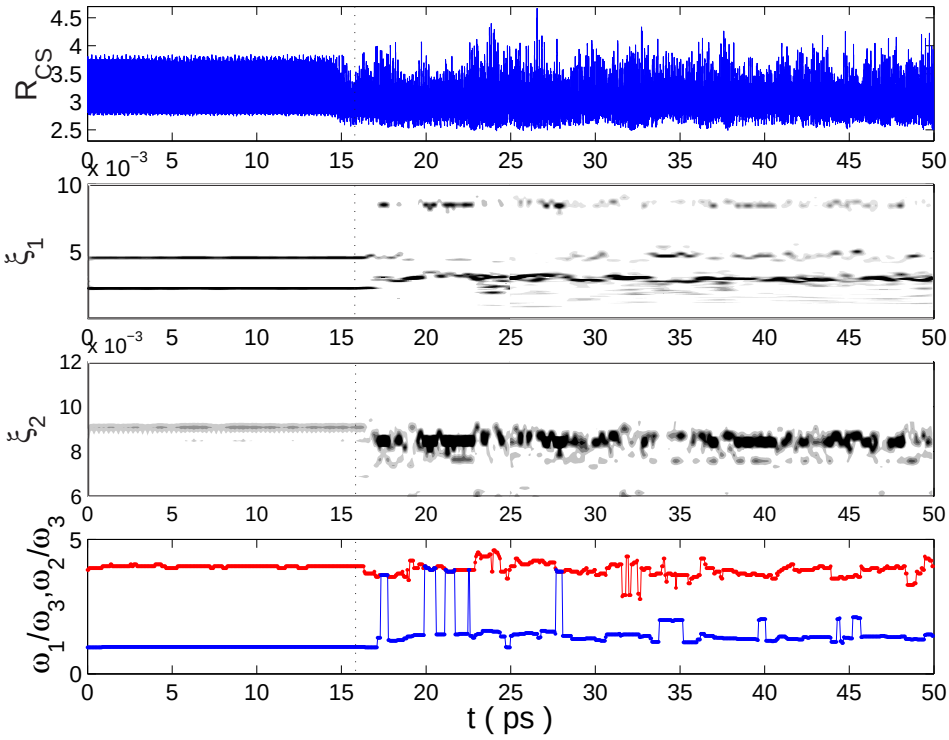

Figure 3.12: Time–frequency decomposition for a chaotic trajectory. Initial conditions are: $R_1 = 2.93, R_2 = 2.4$. $E = 0.1$.

Time–frequency decomposition plots presented in Figures 3.6 (d)–3.12 (d) include the information about temporal variation of the ratios of main frequencies $\omega_1, \omega_2, \omega_3$ defined by the maximum of the normalized scalogram for each vibrational mode. By looking at this information one can refer to the particular region of trapping of trajectories. However, it should be noticed that by considering only main frequencies of a quasiperiodic or chaotic signal one might lose the remaining important spectral information. Moreover, the evolution of the ratios of main frequencies shows discontinuous behavior with time that does not reflect the actual dynamics. From the plots of the maximum of normalized scalogram we observe that the ridges corresponding to different frequency components evolve smoothly with time even for chaotic trajectories. The exception is the intervals where a trajectory enters strongly chaotic region in the phase space as shown in Figure 3.12.

3.4.2 Phase Space Structures via Diffusion of Frequency Maps

The network of resonances represents a communication infrastructure inside the phase space and determines the most important paths for stochastic transport and diffusion of chaotic trajectories from one part of phase space to the other. With the increase of perturbation the dynamics of Hamiltonian system departures from its integrable limit, and some resonant tori lose stability and break up. The resulting phase space represents a mixture of stable resonant structures and chaotic areas. An intrinsic topology around the KAM invariant tori prevents chaotic trajectories to escape fast from vicinities of tori; trajectories can stay in the vicinity of invariant tori for a long time before escaping to other regions of phase space.

For the molecular system of the planar OCS at highly excited regimes the presence of the invariant tori can explain the slow rate of the intramolecular energy relaxation. A crucial role of resonances and invariant structures for chaotic transport was observed in [48] for the collinear OCS model. For the same model Davis [16] found the evidence of long–time trappings of trajectories near the vicinity of the broken golden mean torus (torus with frequency ratio $\gamma = (\sqrt{5} - 1)/2$) that serves as a partial barrier for diffusion of trajectories across it. In this section the intramolecular dynamics of a highly excited planar OCS system is studied by means of time–frequency analysis. By studying spectral decomposition of trajectories from the phase space of the system a number of important resonances were obtained in [50] for the energy $E = 0.9E_{diss}$ of the planar OCS system. These resonances play an essential role in the chaotic transport inside phase space of the system and redistribution of energies within vibrational modes of the molecule. In this section we will complete the previous observations presented in [50] by including the energies much below and at the dissociation threshold.

We observed from the results of the FLI calculations presented in Section 3.3 that the onset of chaoticity and loss of stability for a large number of regular motions for the planar OCS system happens within the range of energies $0.06 < E < 0.08$. Below this range the system is in a near–to–integrable regime. For the energy at dissociation the phase space is constituted mostly by initial conditions corresponding to strongly chaotic trajectories. However, even at the highly excited regime of energy the system dynamics is determined by

the network of resonances that remain stable for this regime. In this subsection we elucidate on these findings by time–frequency analysis of trajectories at different energy regimes of the system.

In our calculations we have used a slightly modified version of the time–frequency algorithm proposed in [5, 50]. The details of the numerical algorithm are given in the subsection 2.2.3 of the previous chapter. Similarly to the FLI method we define an indicator of chaoticity that is based on the notion of diffusion in frequency space. In short, the more chaotic is the trajectory the larger are the variations on its instantaneous frequencies with time and the value of diffusion of frequency coefficient. This notion allows to classify different dynamical behaviors in the same way as the FLI notion establishes the classification of dynamics into regular and chaotic regions.

3.4.2.1 Definition of diffusion coefficient

The original idea to use diffusion of instantaneous frequencies of an analyzed trajectory as an indicator of its dynamical behavior belongs to Laskar [17]. In his work he studied multidimensional dynamics by looking at the time variation of frequencies curves of the corresponding motions. The notion of diffusion of frequency was introduced for the near–to–integrable Hamiltonian systems. In general, there is no unique way to define instantaneous frequencies for strongly chaotic trajectories and the application of different time–frequency algorithms might result in different instantaneous frequency curves. We use the definition of diffusion of frequencies given in [50]. We find this definition to be the most appropriate for the system studied here. In addition, it brings results that are in a good agreement with the results of the FLI stability analysis given in Section 3.3.

For a given n–dimensional trajectory $\mathbf{x}(t) = (x_1(t), x_2(t) \ldots, x_n(t))$ the main instantaneous frequency for each k–coordinate is defined as the maximum of the scalogram as in (2.31). It is a parametric curve $\omega_k(t)$ defined on a finite time interval $t = [0,\ T]$.

Definition. *The diffusion coefficient is determined as the deviation from the mean value* $\widetilde{\omega}_k$ *of the main instantaneous frequency* ω_k *as follows:*

$$diff = \frac{1}{T} \sum_k \left(\int_0^T (\omega_k(t) - \widetilde{\omega}_k) dt \right)^2 , \tag{3.5}$$

where $[0, T]$ *is the time interval analyzed.*

From Subsection 3.4.1 we have seen that time–frequency decomposition for a periodic trajectory consists of a set of constant frequency curves. The main instantaneous frequency curve does not vary in time, and its diffusion coefficient is zero. For a quasiperiodic trajectory each instantaneous frequency curve given on time–frequency domain evolves as a quasiperiodic function of time. To insure that coefficient of diffusion is low one have to chose a large time window in the equation (3.2). For a chaotic trajectory time–frequency domain consists of a set of instantaneous frequencies that vary rapidly in time. In this case the value of the diffusion coefficient is large.

3.4.2.2 Results

Similarly to the FLI analysis we carried out calculations of diffusion coefficient for the main instantaneous frequencies for trajectories. Each trajectory from the $(R_1,\ R_2)$ plane was integrated over the time $t = [0,\ 10]$ ps. We chose the same initial condition subspace as the one considered for the FLI calculations (see Section 3.3). The main instantaneous frequency curves are calculated for each vibrational mode of the system. We obtain the diffusion coefficient strength using the definition given in equation (3.2) for every trajectory from the subspace of initial conditions. The resulting data are mapped out on the $(R_1,\ R_2)$ plane in Figure 3.13 for four different energies: for near–to–integrable regime at the energy $E = 0.05$, for the onset of irregularity regime at the energy $E = 0.08$, for near to dissociation regime at $E = 0.09$, and for non–integrable regime at the dissociation energy $E = 0.1$. The color code is assigned according to the diffusion coefficient magnitude. The periodic and quasiperiodic trajectories are characterized by the low value of the diffusion coefficient whereas chaotic trajectories are characterized by the high values of the diffusion coefficient. At first sight, these plots resemble the FLI stability plots structures in Figure 3.3. In fact, for the energies $E = 0.09$ and $E = 0.1$ the regions with the low values of the FLI correspond to the regions with the low values of diffusion coefficient. Under detailed inspection one observes that at the lower energies the maps of diffusion strength provide more detailed information than the FLI plots. From Figures 3.13 (a) and 3.3 (a) one observes that the

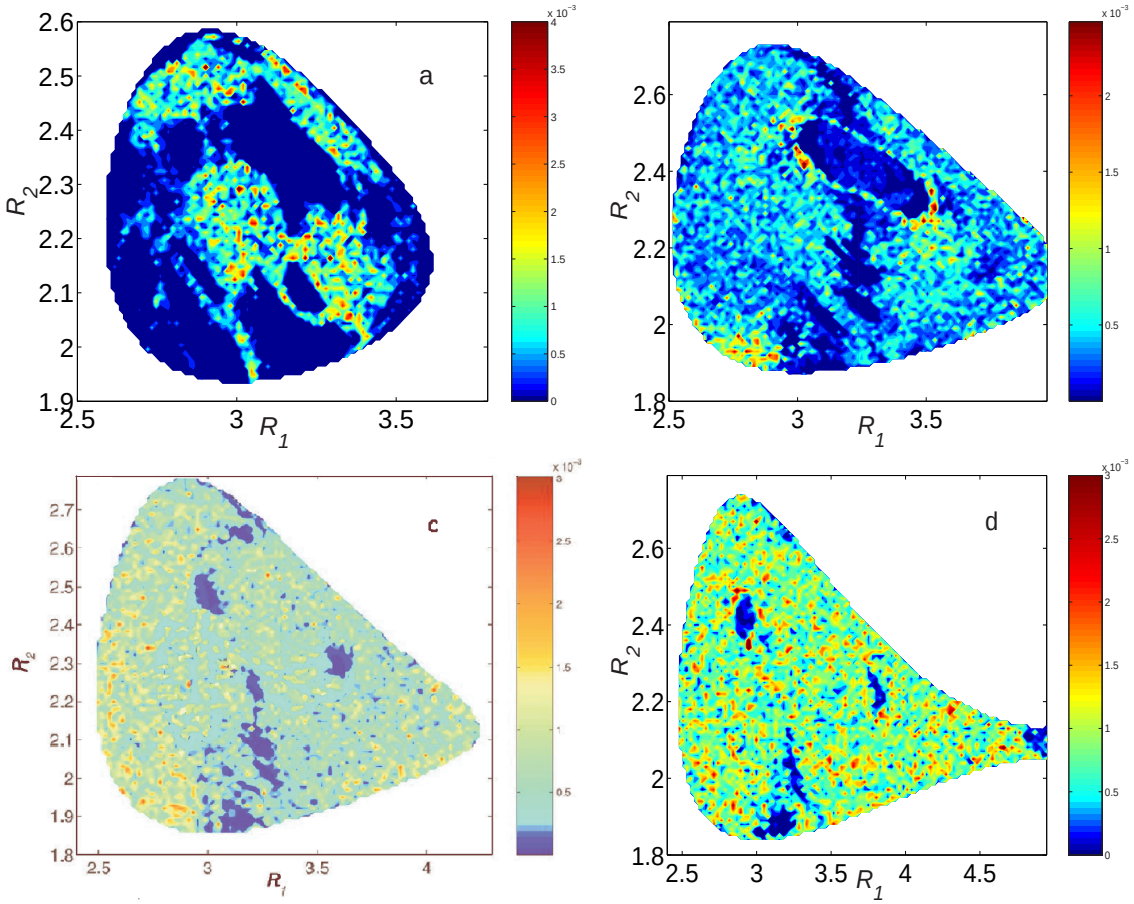

Figure 3.13: Contour plots for diffusion of frequency strength for the planar OCS. Energies are: a) 0.05, b) 0.08, c) 0.09, d) 0.1.

stability regions on the FLI plot correspond to resonant zones characterized by different values of the diffusion coefficients. On Figure 3.13 (b) for the energy $E = 0.08$ more chaotic motions begin to appear and the islands of stability look more localized. The diffusion coefficient contour plot in Figure 3.13 (b) gives more precise determination of the resonant zones than the corresponding FLI plot in Figure 3.3 (b). In Figures 3.13 (c) and 3.13 (d) we observe that few resonant structures remain stable even for energies near to dissociation threshold. However, their size is substantially smaller than the size of the resonant zones for the lower energy regimes. Moreover, the structures of stability are surrounded with strongly chaotic motions characterized by rapid variations of instantaneous frequencies in the time–frequency space. An example of time–frequency decomposition for a chaotic motion is presented in Figure 3.12. Therefore, at energies close to dissociation large part of the phase space is filled with strongly chaotic motions with high values of the diffusion coefficient.

3.4.3 Atlases of Resonances

In Figures 3.13 each stable island marked by the low values of the diffusion coefficients corresponds to some resonant zone. In order to identify all the resonances we have calculated the main frequencies for all three vibrational modes. Our calculations show that periodic and quasiperiodic trajectories originated inside each island have frequency ratios that differ only by a small constant. In fact, the following condition holds:

$$\left| \frac{\omega_k}{\omega_j} - \frac{p}{q} \right| \leq \varepsilon, \tag{3.6}$$

where ε is a small constant. In our calculations $\varepsilon = 0.01$.

In Figures 3.14 and 3.15 the important resonant zones are shown on a mesh of points on (R_1, R_2) plane. These plots are called the atlases of resonances. They were calculated for the same values of energies as were used for the diffusion of frequency plots in Figure 3.13. From Figure 3.14 (a) one observes that the phase space at energy $E = 0.05$ is filled with various resonant zones identified by one or two frequency conditions. For example, resonance $\omega_1 : \omega_2 : \omega_3 = 1 : 1 : 4$ is located in the lower and in the upper part of the configuration space. Another resonant zone, identified by the frequency ratios $\omega_1 : \omega_2 = 1$, is situated in the center of the configuration space. It is apparent, that the structure of contour plot in

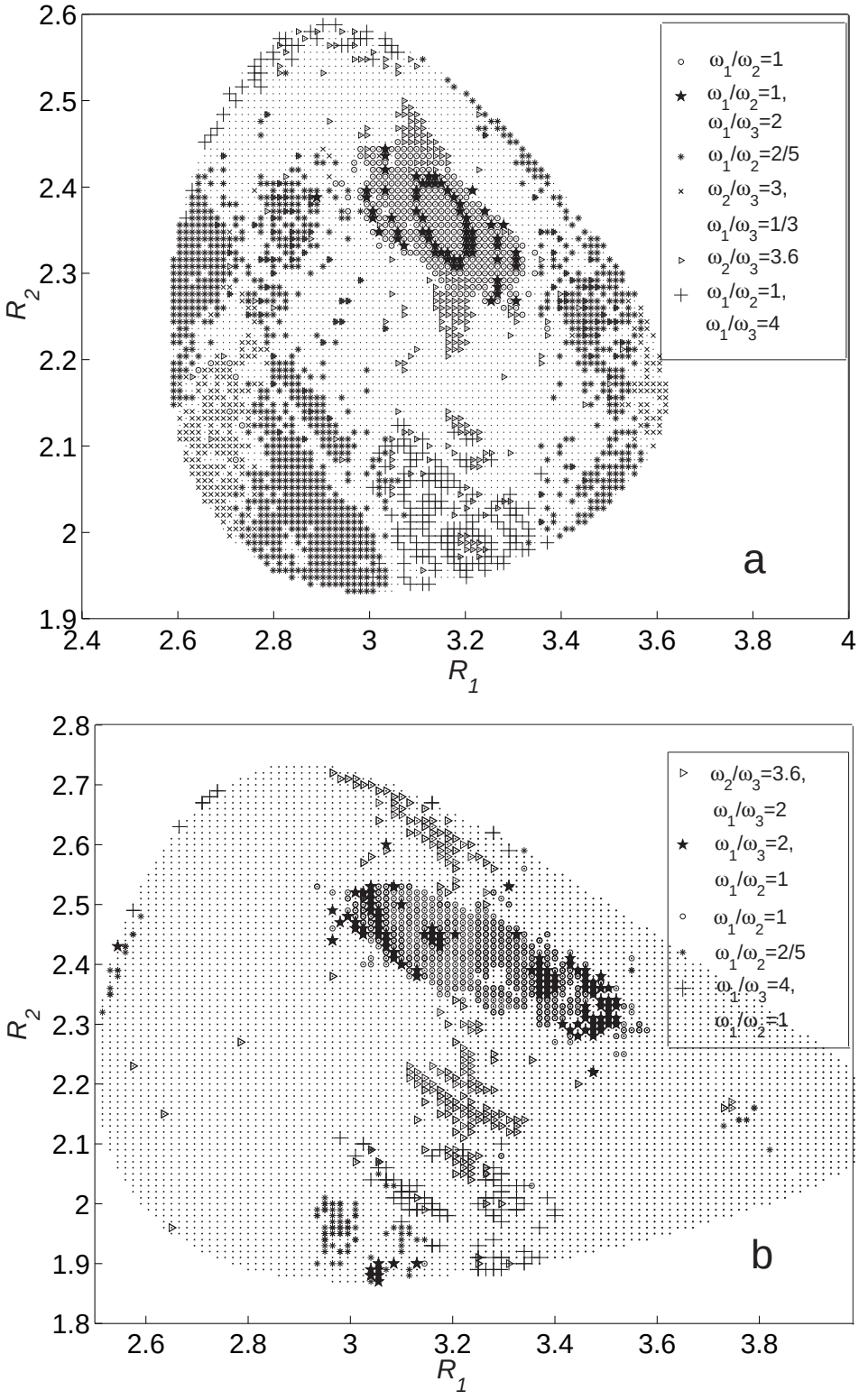

Figure 3.14: Atlases of resonances for two different energy regimes of the planar OCS molecule: a) $E = 0.05$, b) $E = 0.08$.

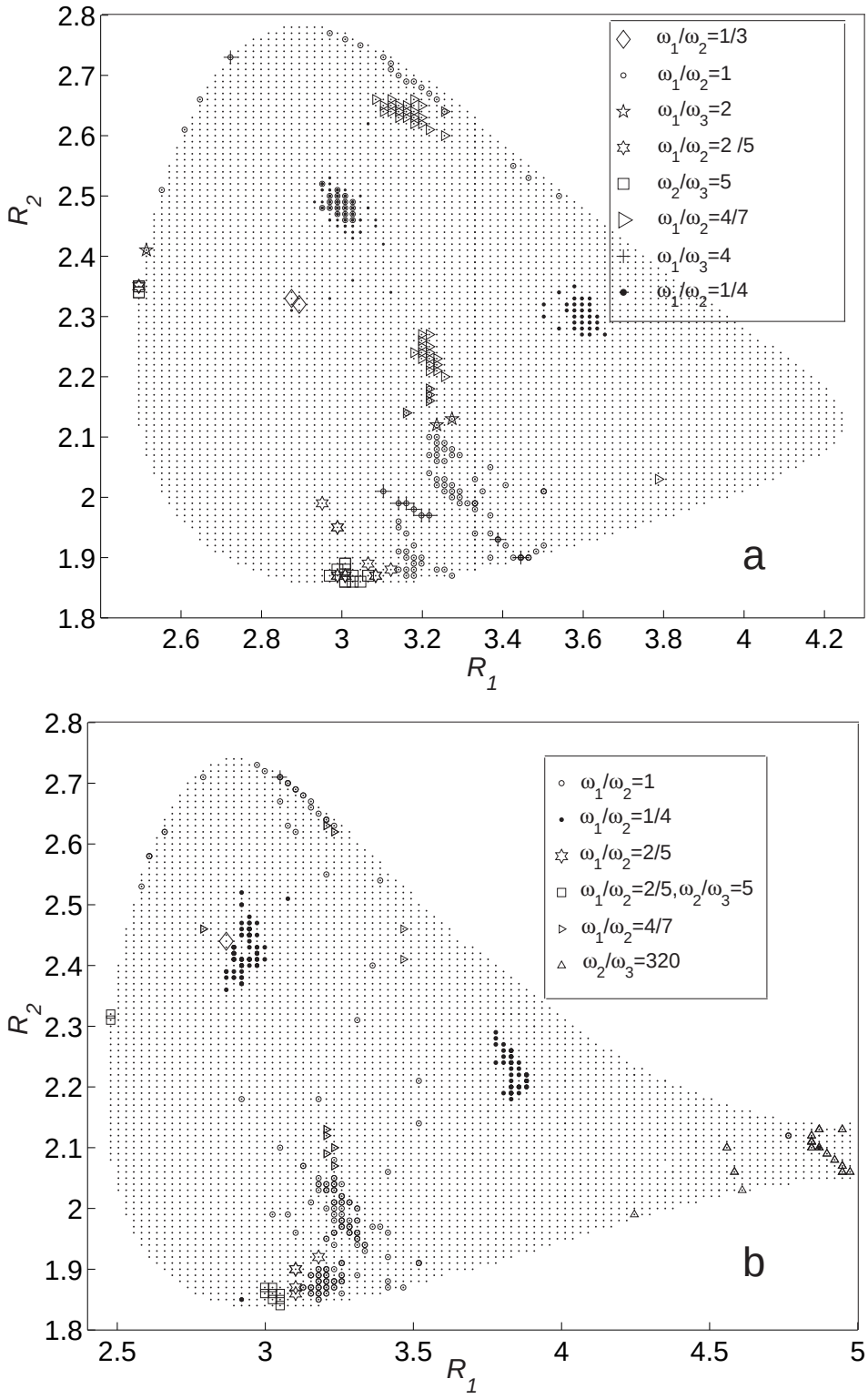

Figure 3.15: Atlases of resonances for two different energy regimes of the planar OCS molecule: a) $E = 0.09$, b) $E = 0.1$.

Figure 3.13 (a) matches the atlas of resonances in Figure 3.14 (a). The highlighted zones are associated with initial conditions for the quasiperiodic trajectories. In Figure 3.14 (a) not all the resonances are shown. We identified the most important resonant zones, which are relevant to the observed long–time trappings of chaotic trajectories. Some resonances observed for the low energy regime $E = 0.05$ remain stable for the high energy regimes as well. From Figures 3.14 (a) and 3.15 (a) it is seen that the resonant zone corresponding to $\omega_1 : \omega_2 = 1$ also exists for the energy $E = 0.09$. It is divided into two small islands, which occupy significantly smaller volumes in the phase space than the same resonance for the low energy $E = 0.05$. In the center of Figure 3.15 (a) two resonant zones are seen with the frequency ratios $\omega_1 : \omega_2 = 1/4$. The same resonant zones exist for the energy $E = 0.1$ (see Figure 3.15 (b)), the size of them becomes smaller. Few resonances still survive inside the large chaotic area on Figure 3.15 (b) for the energy $E = 0.1$. In addition, a number of subharmonic resonances appear in the vicinity of the transition to dissociation region. These resonances correspond to high–frequency vibrations in the CO mode. The frequency ratios for the CO stretch and α bending mode satisfy the relation: $\omega_2 : \omega_3 > 320$, and the motions originated inside this resonant zone eventually enter the dissociation channel on the right.

In order to provide a complete representation of frequency space, we plot frequency ratios for all initial conditions from the configuration space computed at fixed moment of time $t =$ 0.01 ps. In Figures 3.16 the frequency ratio spaces are shown on the $(\omega_1/\omega_2,\ \omega_1/\omega_3)$ plane. These plots resemble the structure of the Arnold web of resonances [1, 47]. However, these structures are not complete since we consider the subspace of initial conditions restricted to the zero–momentum surface ($P_1 = P_2 = P_\alpha = 0$). In Figure 3.16 (a) the frequency ratios shown are confined by the frequency conditions: $\omega_1 : \omega_3 = 11 : 5,\ \omega_1 : \omega_3 = 5 : 4,\ \omega_2 : \omega_3 = 3,\ \omega_2 : \omega_3 = 4 : 7$. It is evident that the resonances $\omega_1 : \omega_2 = 1,\ \omega_1 : \omega_3 = 2$ are isolated from the other resonances. As was pointed out above, with the increase of excitation in the system a large set of resonant motions loses stability. For example, some of the resonances observed in Figure 3.16 (a) along the line $\omega_2 : \omega_3 = 2$ do not exist for the higher energy $E = 0.09$ (c panel). However, since the configuration space is larger for

the higher energies we expect the new resonances to appear in the system. Indeed, for the energy $E = 0.09$ the set of resonances looks much larger than the set observed for the lower energy limit $E = 0.05$. This set is situated inside the region of the frequency space confined the lines: $\omega_1 : \omega_3 = 1,\ \omega_1 : \omega_3 = 11 : 5$ and $\omega_2 : \omega_3 = 3,\ \omega_2,\ \omega_3 = 5$. In Figure 3.16 (e) the frequency ratios for the energy $E = 0.1$ are plotted in logarithmic scale for convenience. The main difference of these data from the data for the lower energies ($E = 0.05,\ 0.08,\ 0.09$) is the appearance of various high order resonances that are typical for the orbits near to dissociation region. A magnification of central region on Figure 3.16 (e) is plotted on (d) panel. The frequency space structure given on (d) panel for energy $E = 0.1$ is similar to the one observed for lower energies. An exceptional feature is the presence of a few subharmonic resonances with frequency ratios: $\omega_1 : \omega_3 = 1 : 2,\ \omega_2 : \omega_3 = 1 : 2$ and $\omega_1 : \omega_2 = 1 : 12$.

From the results considered above we may conclude that a well–defined resonant structure governs intramolecular dynamics of the OCS system from near–to–integrable regime to the highly excited energy regime at dissociation threshold. Most of the phase space at energy $E = 0.05$ is filled with the low order resonant zones. With the increase of the energy the configuration space of the system gets larger and new resonant structures are born. It is part of our observation that secondary invariant structures around the main resonances loose stability and disappear for the high energies. With the increase of excitation in the system the area of each resonance decreases and only a thin layer of quasiperiodic orbits winding around the main periodic orbits remains. We might expect that at high–excitation regimes chaotic trajectories might be trapped only within the narrow layer of quasiperiodic motions around each periodic orbit.

3.5 Conclusions

We have applied fast Lyapunov indicator together with time–frequency analysis methods to study vibrational dynamics of the planar OCS molecule at energies below and at dissociation threshold. The FLI method provides a geometrical representation of the phase space in terms of the FLI contour plots that distinctly identify existing resonant zones and chaotic areas.

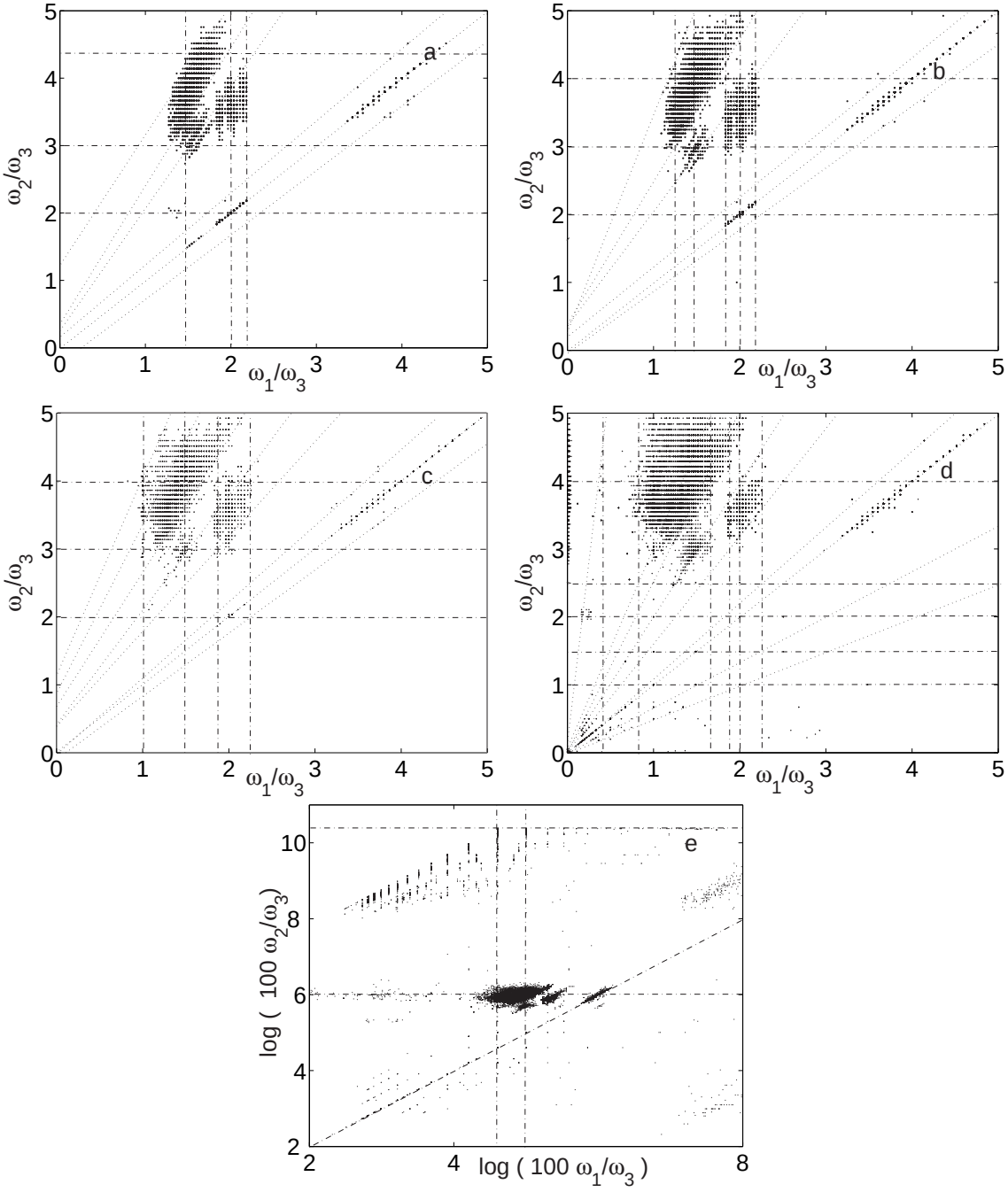

Figure 3.16: Frequency ratio spaces for the planar OCS at the energies: a) 0.05, b) 0.08, c) 0.09, d) 0.1, e) 0.1.

From the structures of FLI plots we observed the evolution in global dynamics of the planar OCS system. For energies much below the dissociation threshold the system is in a near–to–integrable regime, and phase space is mostly filled by periodic and quasiperiodic motions. When energy increases to the dissociation threshold a significant number of bifurcations occurs in the system, which leads to the break–up of some resonant zones. For the energies close to dissociation threshold the remaining stable zones occupy a small volume of the phase space and the phase space dynamics is predominantly chaotic. We identify the interval of energy, for which a large number of bifurcations happens, and transition from regular to chaotic dynamics of the OCS system occurs.

The FLI method is an effective and fast tool for identifying stable structures of multidimensional Hamiltonian systems. The results of the method simplify the problem of finding a good initial guess for the periodic orbit search; without knowing *a priori* the locations of regular regions inside the multidimensional phase space this task is far from trivial. We find a number of elliptic and hyperbolic periodic orbits for all the energies considered in the stability analysis calculations. Most of the elliptic periodic orbits are located in the center of the configuration space where the energy is well redistributed among all the vibrational modes. Most of the hyperbolic periodic points are the in–phase solutions: the bending mode is fixed and two stretching modes vibrate at the same frequency.

The time–frequency analysis was applied for the planar OCS for different energies below and at the dissociation. The analysis of instantaneous frequency curves computed for different types of trajectories give an accurate information about diffusion of trajectories and the character of transitions between different resonant zones inside the phase space of the system. We have listed the main features of transport of chaotic trajectories for different energy regimes of the system: from a near–to–integrable to a non–integrable regime near the dissociation. At the highly excited energy regimes close to dissociation threshold we have found the evidence of rapid transitions of chaotic trajectories between main resonant zones and the long–time trappings near to two–dimensional tori.

Our data obtained by the combination of FLI method and time–frequency analysis completed the results given in [49], where the Local Frequency Analysis was applied to

examine the resonances and various transitions between them. By using time–adjustable wavelets the method of time–frequency analysis accurately identifies rapid spectral changes for any chaotic solution of the OCS system in highly excited energy regimes. We have extended results of time–frequency analysis obtained in [50] from energy at 90% of dissociation threshold to a large interval of energies corresponding to different regimes of excitation of the molecular system.

CHAPTER IV

CLASSICAL IONIZATION DYNAMICS OF HYDROGEN ATOM INSIDE ELLIPTICALLY POLARIZED MICROWAVE FIELDS

4.1 Introduction

One of the most simple and at the same time challenging problems of atomic physics is hydrogen atom in electromagnetic field. Various application of this system are found in many branches of modern physics starting from atomic and plasma physics [53, 54] to celestial mechanics [55]. An enormous interest among experimentalists and theoreticians in this problem is based on the fact that the system is an example of a low–dimensional quantum system that manifests behaviors typical of classical nonlinear systems, such as chaos, stochastic ionization, and high sensitivity to the parameters of the electromagnetic field.

The first experiments on the multi–photon ionization of highly excited hydrogen atoms with principal quantum number $n \simeq 66$ using radio- and microwave frequencies of an external electromagnetic field was done by Bayfield and Koch in [56]. They observed a significant ionization above the critical microwave (with frequency $\omega/2\pi = 9.9$ GHz) amplitude of the electric field of $F \simeq 20$ V/cm. The strength of the field, for which considerable ionization occurred in this experiment, was much lower than the strength of the static electric field needed to ionize the atom. The ionization probabilities depend sensitively on the parameters of the field, such as frequency and amplitude. Since these experiments was done for the low–frequency regime the ionization mechanism was accounted for the Stark ionization effect. For the highly excited hydrogen atom states ($n \simeq 66$) the application of the classical treatment, which has been traditional in the subject, is very well justified [53, 57]. In Reference [58] Leopold and Percival did numerical integration of classical model of hydrogen

atom in a time–dependent field in the low–frequency regime $\omega < \omega_K$, where $\omega_K = n^{-3}$ is a Kepler frequency of a state with a principal quantum number n. It was shown that classical ionization of the electron happens at a field strength much lower than is required for a significant quantum tunneling. The ionization rates calculated classically agreed well with the experimental data in [56]. The subsequent classical studies on the ionization of hydrogen by linearly polarized (LP) field were done for the one–dimensional model [59, 60]:

$$H = \begin{cases} \frac{p^2}{2} - \frac{1}{z} + Fz\cos\omega t, & \text{for } z > 0, \\ \infty, & \text{for } z \leq 0\ , \end{cases} \tag{4.1}$$

were p and z are the momentum and position of the atomic electron in the z–direction. It was shown in [53] that one–dimensional dynamics approximates well the motion of an excited hydrogen atom. Indeed, for a large principal quantum number n the states of the hydrogen are elongated along direction of the applied field with negligible extension in the other directions [61] and such states are the approximate eigenstates of one–dimensional Hamiltonian. The external perturbation induces mainly transitions in the principal quantum number n and the atom stays one–dimensional in the presence of the time–dependent field. Outside of a given low–frequency range the quantal effects become more important and classical models are less successful [53].

Much more complex dynamics was discovered for the hydrogenic atoms in circularly polarized (CP) microwave fields. The first experiments for the circularly polarized fields were carried out by group of Gallagher [62]. They performed alkali–metal–atom experiments for a low–frequencies field. The ionization thresholds for the CP field were found to be much higher then those for the LP field. The results of the experiments have shown that ionization threshold follows classical scaling behavior over the range of the fields amplitude as in the static case (Stark effect). These results were explained by going to the frame rotating with the applied field frequency and showing that ionization dynamics in this frame described as for the static field case. Later it was shown by Nauenberg [63] that ionization mechanism in the CP problem is much more complicated, and the effect of the field rotation has to be taken into account. Subsequently, the CP problem was studied classically by Mostowski *et al* in [64] and by Meerson in [65] for special cases of a very high or very low eccentricity

orbits.

The first experiment [60, 66] on ionization of hydrogen atom by CP and EP microwaves was done for the range of frequencies $0.5 < \omega/\omega_K < 1.4$ and mixture of different initial angular momentum states corresponding to principal quantum numbers $n = 31 - 45$. The time–dependent expression of the microwave field used in this experiment is given as follows:

$$\mathbf{F}(\mathbf{t}) = \lambda(\mathbf{t})\mathbf{F}(\mathbf{x}\cos\omega\mathbf{t} + \alpha\mathbf{y}\sin\omega\mathbf{t}), \tag{4.2}$$

where $\lambda(t)$ is the field pulse shape and $0 \geq \alpha \leq 1$ is a polarization of the field. The main result of the experiment [60] is a possibility to provide an efficient and simple control of ionization of excited hydrogen atoms in microwave fields by adjusting experimentally the polarization of the driven field. The experiments [66, 60] on the ionization of the hydrogen atom in a strong elliptically polarized (EP) microwaves have demonstrated that the system dynamics for the EP field case is much more complex, exposing new effects that are not present for the circularly polarized (CP) and linearly polarized (LP) fields. The ionization dynamics was observed to be extremely sensitive to the polarization degree of the electric field. Moreover, the results of the three–dimensional classical calculations [59, 66] which model the dynamics of hydrogen in EP field reproduce very well the experimental results. It was shown in [60] that the ionization probability yields, calculated experimentally and numerically, interpolate unevenly between LP and CP limits and for the intermediate polarization follow a non–monotonic rise with the increase of the scaled field amplitude. The maxima and minima of the ionization yields were accounted for the classical resonant effects produced by the Stark states and the driving field frequencies [59]. The results of the experimental data were explained with the quantum approach based on the quasi–energy states formalism by Oks and Uzer [67]. By considering the system in the frame rotating with the time–dependent angular velocity of the electric field the authors have showed that the dynamics of the problem can be reduced to that of a Rydberg atom subject to two effective static fields: magnetic and electric fields. They discovered that the minima in the experimental ionization yield curves correspond to the maximum of the effective magnetic field interaction. The sensitivity of ionization thresholds to the ellipticity of the field was

accounted for the dependence of the effective magnetic interaction on the ellipticity degree. While the use of the quantum–mechanical approach for hydrogen in EP field provides an accurate predictions to the experimental data, one would look for a connection with the results given by the classical approach, which has been traditional in this subject. The question still remains open: why the available experimental data on ionization yield curves of hydrogen atom in EP microwave fields are in a strikingly good agreement with the corresponding classical calculations [60, 62].

The first classical calculations of the ionization rates for three–dimensional hydrogen inside EP field is due to Griffith and Farrelly [68], who reported enhanced ionization rates for the EP problem as opposed to the CP problem. This unusual behavior was accounted for the changes that occur in the phase space dynamics as the fields polarization varies from elliptical to circular. In fact, as the polarization departs from its CP limit invariant structures break–up and chaotic areas start to grow inside the subspace of the phase space. The presence of chaos opens up a possibility for diffusion of trajectories and can explain enhanced ionization rates observed experimentally and numerically for the EP field as opposed to the CP field [62, 68]. Most of the classical treatments for the EP problem considered in the literature used some simplifications of dynamics or reduction of a full high dimensional dynamics of the system to the lower–dimensional one [59, 68, 69]. To give an example, the adiabatic approximation used by Griffith and Farrelly [68] allows to reduce the dimension of the effective phase space and limits the dynamics to the circular Rydberg states only. The averaging of dynamics that is performed in [59] is valid only in the low frequency regime. Another challenge that study of classical dynamics of hydrogen atom in the EP field brings in is the presence of a time–dependent term in the expression of the Hamiltonian. In addition, the absence of conserved quantities, such as energy and angular momentum integrals, prevents one from reducing dynamics to the lower dimensional one. For the LP and CP problems the reduction is possible due to existence of additional constants of motion. For the CP problem the Hamiltonian can be transformed to the time–independent quantity by considering dynamics in the frame rotating with the frequency of the applied field [62, 70]. For the LP field case the reduction in the dimensionality of the system is possible due to the

angular momentum conservation. In contrast, for the EP field case the energy and angular momentum are not conserved. In this work we discuss the possibility to view a full dimensional system dynamics by means of fast Lyapunov indicator fields of stability. The FLI method is independent on the systems dimension. It brings the pictures of global stability structures for any given two–dimensional subspace of the multidimensional phase space of the system. Besides, the method is robust, for its application is permitted for regimes of the system that can not be studied by any existing analytical methods.

The complex features of ionization dynamics of hydrogen atom in EP microwave field reported in the experiments [60] are accounted for the higher dimensionality of the EP field problem as opposed to the CP and LP limits. Classically, for systems with more than three degrees of freedom the phase space dynamics is known to possess much richer features than the dynamics for the lower–dimensional systems. The principal feature that distinguishes phase space dynamics of Hamiltonian system of dimension three and higher from the lower–dimensional system is the possibility of the Arnold diffusion phenomenon (diffusion along the resonances) to occur [1]. This phenomenon is essential for examining all possible scenarios that lead to the classical ionization for the hydrogen in the EP field. It is well known, that the phase space invariant tori structures for systems of three or higher degrees of freedom can not divide the effective phase space into isolated parts; the dimensionality of tori is too low for constituting effective phase space barriers. Therefore, there are no barriers that can prevent stochastic diffusion of trajectories across the phase space. Moreover, in was shown in [71] for the three–dimensional classical model of hydrogen in crossed static fields that Arnold diffusion can accelerate the escape of chaotic trajectories. In an essence, resonance structures can serve as a mediator for stochastic diffusion of trajectories and their subsequent ionization.

The destruction of invariant tori and onset of stochastic ionization for the Hamiltonian systems has been traditionally investigated by means of resonance criterion introduced by Chirikov [30]. The Chirikov criterion predicts the low bound for the onset of the global stochasticity in the phase space of the system. KAM theory [27, 28, 29] guarantees that for a small perturbation of the Hamiltonian most of the invariant tori inside the phase

space survives and trajectories remain bounded by the invariant tori. When the field amplitude exceeds some critical value phase space of the system becomes interconnected by the stochastic web. Ionization in the hydrogen atom inside electromagnetic fields model results when the chaotic trajectories in the phase space escape into the continuum. The first application of the Chirikov resonance overlap criterion to a real quantum–mechanical system was carried out in [72]. Later, the Chirikov criterion was applied to study classical ionization dynamics for the hydrogen atom driven by LP and CP field in [8, 53, 65, 72, 73, 74, 75, 76]. Although most of the classical calculations based on the Chirikov overlap criterion successfully agreed with the results of the experiments, its application for the hydrogen in EP field is not feasible. The set of action–angle variables is not well–defined for the Hamiltonian of this system. Instead, we propose to study the onset of stochasticity in the phase space of the system by means of fast Lyapunov Indicator stability analysis. By evaluating the indicator of chaoticity for each integrated trajectory from an ensemble of trajectories we obtain underlying resonant structures for any given subspace of the system phase space.

The data of the experiment in Reference [60] does not provide an information about the character of the states that determines the ionization threshold, e. g., the states, which ionize for the lowest microwave amplitudes. Generally speaking, most of the initial states used in the experiment will be switched by the application of the field to completely different parts of the phase space and to different eccentricity values [77]. Some of the states switched by the field to the regions of the phase space corresponding to the classical ionization.

A lot of the theoretical results available now are devoted to the character of the states favorable to ionization. Investigations on the ionization for the CP case for the high-frequency regime was carried out by Howard [74] and later by Sacha *et al* in [78]. Using essentially the same technique, Chirikov overlap criterion, these two groups arrived at different conclusions regarding the type of the orbits that ionize first by the application of the CP microwave field. Howard claimed, that most of the orbits become elongated before they ionize and that core effects are very important in ionization mechanism. However, results in [78] contradict this point of view. The authors showed that ionization occurs first for the medium eccentricity orbits and generic type of this orbits never come close to the nucleus. In reference [77] it

was pointed out that orbits with different eccentricities can be switched to different parts of the phase space and to different energies in the rotating frame for CP field problem. In this section we describe in details the character of the states that undergo ionization and determine the behavior of ionization yields for the low amplitudes of the field. The principal difficulty is the interpretation of our results in connection with the actual experiment [60]. It is essential to point out, that our qualitative stability analysis is performed for the ensemble of states with the same initial energy, and different values of classical action and angular momentum, as opposed to the ensemble of states used in the experiment. Our choice is mainly dictated by the possibility to attribute underlying phase space structures to the ionization dynamics of the system.

This chapter is organized in six sections. In Section 4.2 we introduce the Hamiltonian and describe the concept of time–dependent zero–velocity surface (ZVS) in the frame rotating with frequency of applied field. In Section 4.3 we discuss the application of the FLI stability analysis to ensemble of states initiated at energy equal to the maximum of the ZVS. By mapping out the value of fast Lyapunov indicator for each trajectory from configuration space we obtain the FLI plots of stability. First, the structure of FLI stability plots is described for well–studied LP and CP problems. For the CP problem FLI stability plots perfectly match the Poincaré surfaces of section structure. Similarly to Poincaré surface stability structures the FLI plots picture chaotic versus regular dynamics in phase space of analyzed system. The FLI data allows prediction of the fate of initial ensemble of states after the turn–on of electric field. Second, we perform the FLI analysis for more complicated problem of hydrogen atom subjected to EP field (magnetic field is equal to zero). We found that for the EP problem the phase space structures at energy equal to maximum of the ZVS look similar to those for the LP and CP problems. Two sets of bounded states are distinguished by the FLI plots. One set corresponds to low eccentricities and positive angular momenta states located around maximum of the ZVS. Another set corresponds to states of various eccentricities and negative angular momenta located around the center of the ZVS. The size of stability zone around the ZVS maximum is used to estimate qualitatively the behavior of the ionization yields versus scaled amplitude of electric field. In Section 4.4 we

present stability results for ensemble of states with initial energy below the Stark saddle point energy. Section 4.5 is concluded with the detailed description of ensembles of initial states used in our calculations and its relevance to the FLI stability results. In Section 4.6 we discuss the main results.

4.2 Description of the Classical Model

4.2.1 Hamiltonian

In atomic units ($a_0 = \hbar = e = \mu = 1$) and assuming infinite nuclear mass the Hamiltonian for hydrogen atom subjected to EP electric field (of magnitude F and microwave frequency ω) simultaneously with the static magnetic field (of magnitude B) applied perpendicular to the plane of polarization is written as follows:

$$\begin{aligned} H &= \frac{1}{2}(p_x^2 + p_y^2 + p_z^2) - \frac{1}{2}B(xp_y - yp_x) \\ &\quad -\frac{1}{r} + \frac{1}{8}B^2(x^2 + y^2) + F(x\cos\omega t + \alpha y \sin\omega t) \ , \end{aligned} \tag{4.3}$$

where $\alpha \in [0, 1]$ is a polarization of electric field, $\alpha = 1$ for the circularly polarized field, and $\alpha = 0$ for the linearly polarized field. In this section we study the planar classical model of hydrogen restricted to the $x-y$ polarization plane. Most of previous classical and quantum calculations were performed in the planar limit [68, 69, 77, 79, 80]. The planar limit of a three–dimensional system gives a reliable approximation to the actual three–dimensional dynamics for the orbits with initial conditions initiated on the $z = 0, p_z = 0$ subspace. The subspace is invariant under dynamics. Moreover the classical phase space dynamics for the planar limit of hydrogen atom inside CP and LP fields can be studied by means of Poincaré surface of section, which in this case is two–dimensional. Because polarization of electric field is chosen on the $x - y$ plane the classical ionization of hydrogen is expected to occur along any direction on the plane as in the Stark effect.

An insightful view of dynamics can be obtained by considering the system in the rotational frame moving with frequency of electric field ω. By introducing canonical transformation

$$S(\bar{x}, \bar{y}, p_x, p_y) = -(\bar{x}\cos\omega t - \bar{y}\sin\omega t)p_x - (\bar{x}\sin\omega t + \bar{y}\cos\omega t)p_y \tag{4.4}$$

one gets Hamiltonian in the rotational frame (for convenience we omit the bars in the following expression and further on):

$$\begin{aligned} H &= \frac{1}{2}(p_x^2+p_y^2)-(1+\frac{1}{2}B)(xp_y-yp_x) \\ &\quad -\frac{1}{r}+\frac{1}{8}B^2(x^2+y^2)+Fx+F(\alpha-1)(x\sin^2\omega t+y\sin\omega t\cos\omega t)\ . \end{aligned} \tag{4.5}$$

It is more convenient to work with scaled frequencies and field strengths. We introduce the scaling of time, coordinates, momenta, and field amplitudes as follows: $t^{'}=\omega t, r^{'}=\omega^{2/3}r, p^{'}=\omega^{-1/3}p, K=\omega^{-2/3}H, F^{'}=\omega^{-4/3}F, B^{'}=\omega^{-1}B$. After dropping the primes this yields for the scaled Hamiltonian:

$$\begin{aligned} K &= \frac{1}{2}(p_x^2+p_y^2)-(1+\frac{1}{2}B)(xp_y-yp_x) \\ &\quad -\frac{1}{r}+\frac{1}{8}B^2(x^2+y^2)+Fx+F(\alpha-1)(x\sin^2 t+y\sin t\cos t)\ . \end{aligned} \tag{4.6}$$

For the CP field ($\alpha=1$) Hamiltonian is time–independent and the system has two effective degrees of freedom. The Jacobi constant introduced in celestial mechanics [81, 82] is equal to the energy of the system in the rotational frame. For the EP field ($0<\alpha<1$) Hamiltonian is a time–dependent quantity. For the EP problem, due to the absence of integrals of motion, the system can not be reduced to a low–dimensional one as for the CP problem. Instead, a time–dependent Hamiltonian in (4.6) can be made an autonomous by introducing a new set of coordinates (x,y,w,p_x,p_y,p_w), where $w=t$ is a time variable and $p_w=-K(t)$ is a generalized momentum. The expression for the effective autonomous Hamiltonian yields:

$$\begin{aligned} H_{eff} &= \frac{1}{2}(p_x^2+p_y^2)+p_w-(1+\frac{1}{2}B)(xp_y-yp_x) \\ &\quad -\frac{1}{r}+\frac{1}{8}B^2(x^2+y^2)+F(\alpha-1)(x\sin^2 w+y\cos w\sin w)\ . \end{aligned} \tag{4.7}$$

Equation (4.7) now describes a three degrees of freedom autonomous Hamiltonian system. In our numerical calculations the Hamiltonian equations of motion are regularized by changing coordinates to a set of semi–parabolic coordinates. This substitution is used in order to avoid the singularity near the origin $(x,y)=(0,0)$. The transformation to the semi-parabolic coordinates is

$$S(u,v,p_x,p_y)=-\frac{1}{2}(u^2-v^2)p_x-uvp_y\ . \tag{4.8}$$

Old coordinates in terms of the semi-parabolic coordinates are expressed as:

$$x = \frac{u^2 - v^2}{2}, \qquad y = uv, \qquad p_x = \frac{up_u - vp_v}{u^2 + v^2}, \qquad p_y = \frac{vp_u + up_v}{u^2 + v^2} \ . \tag{4.9}$$

Finally, the expression for Hamiltonian in terms of the semi–parabolic coordinates results:

$$\begin{aligned} H_{eff} \ &= \ \frac{p_u^2 + p_v^2}{2} + p_w(u^2 + v^2) - 2 - \frac{1}{2}(1 + \frac{1}{2}B)(u^2 + v^2)(up_v - vp_u) \\ &+ \frac{1}{2}F(u^4 - v^4) + (\alpha - 1)F(u^2 + v^2)\left[\frac{1}{2}(u^2 - v^2)\sin t + uv\cos t\right]\sin t \\ &+ \frac{1}{32}B^2(u^2 + v^2)^3 \ . \end{aligned} \tag{4.10}$$

4.2.2 Time–dependent Zero–velocity Surface

A striking confirmation of universality of laws of Nature can be found, when one investigates the quantum analog of the celestial mechanics three–body problem represented by Rydberg atom subjected to electromagnetic field radiation [83]. The discovery by Bialynicki–Birula *et al* [84] of stable Trojan wavepackets that are the coherent states that orbit the nucleus without spreading and are launched from the equilibria of the effective potential surface reminds one of the Trojan asteroids that exist in the Sun–Jupiter-Asteroid problems. In the restricted three–body problem one studies the motion in the frame that rotates with the Kepler frequency of the primaries, which are the Sun and Jupiter. The resulting Hamiltonian in the rotational frame contains the Coriolis term. The Coriolis term prevents one from separating energy into potential part, depending purely on coordinates, and kinetic part, depending exclusively on momenta. Instead of using potential surface, the idea of zero–velocity surface (ZVS) was adapted by Hill in [81] to study dynamics in a rotational frame. In the problem of hydrogen atom in CP microwave field a Hamiltonian expression contains the Coriolis term that mixes coordinates and momenta and prevents one to study stability of equilibria by directly using potential energy surface. Similarly to the restricted three–body problem the introduction of ZVS for hydrogen in EP field gains more insight into system dynamics. In particular, it allows to derive the stability conditions for the equilibria, that determined much of the system dynamics.

To define an expression for the ZVS we write Hamiltonian (4.5) in terms of velocities and coordinates alone:

$$\begin{aligned} K &= \frac{1}{2}(\dot{x}^2+\dot{y}^2) - \frac{(1+B)}{2}(x^2+y^2) - \frac{1}{r} + Fx \\ &\quad + F(\alpha-1)(x\sin^2 t + y\cos t \sin t). \end{aligned} \tag{4.11}$$

Setting velocities $\dot{x}, \dot{y}$ in the above expression to zero we arrive at the following form of an effective time–dependent potential surface:

$$\begin{aligned} V(x,y) &= -\frac{1}{r} - \frac{(1+B)}{2}(x^2+y^2) + Fx \\ &\quad + F(\alpha-1)(x\sin^2 t + y\cos t \sin t). \end{aligned} \tag{4.12}$$

In the circular polarized case ($\alpha = 1$) the ZVS is time–independent in the rotational frame. There are two equilibria $x_\pm$ along the x–axis that corresponds to the maximum (+) and saddle point (−) of the surface:

$$-(1+B)x_\pm^3 + F[1+(\alpha-1)\sin^2 t]x_\pm^2 \pm 1 = 0, \tag{4.13}$$

In Figure 4.1 zero–velocity contour plots and locations of equilibria $x_\pm(0)$ are pictured at time $t = 0$. The equilibria for hydrogen atom in EP microwave field are analogous to the Lagrange equilibria discovered by Lagrange as early as in 1770's [82] for the restricted three–body problem. In a time–honored fashion equilibria of the ZVS are called the Lagrange equilibria.

Unlike maxima of the potential surface that are always unstable, maxima of the ZVS need not be. For the CP field a stability analysis can be carried out by considering a local dynamics around the Lagrange equilibria and reducing it to harmonic oscillator dynamics [80]. Stability of equilibria of the ZVS is determined by parameters of a perturbed Coulomb Hamiltonian. For the three–body problem the amplitudes of the gravitational force and the Coriolis force play a major role in stabilization of trajectories near the Lagrange equilibria. For an atomic problem of hydrogen subjected to CP field the strength of electric and magnetic field determines local stability around maximum of the ZVS [80]. As can be seen from the expression (4.11) that for $\alpha < 1$ the ZVS is time–dependent in the rotational

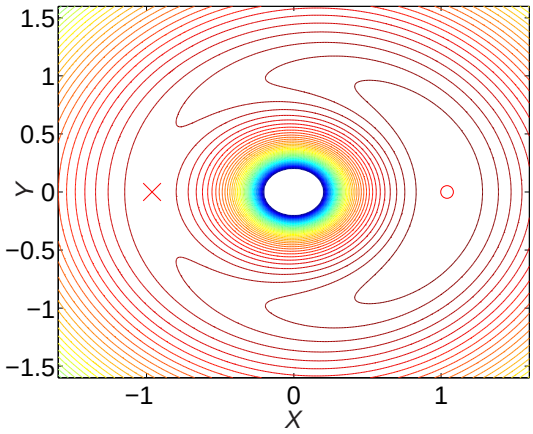

Figure 4.1: Zero velocity surface contour plot at time $t = 0$ for the hydrogen in the EP microwave electric field. $F = 0.117, B = 0$. The circle (cross) indicates the location of the maximum (saddle) point of the ZVS.

frame. In fact, it rotates around the origin with the frequency of applied field. For the time–dependent Hamiltonian of hydrogen in EP field the equilibria are not fixed in time, therefore, local stability analysis analogous to the one performed in [80] is not tractable. In the next section we describe the results of linear stability analysis rendered by the fast Lyapunov indicator method. This method is applied to study local dynamics around the Lagrange maximum for different polarizations and amplitudes of electric field.

4.3 Ionization dynamics at the Lagrange Maximum

4.3.1 Fast Lyapunov Indicator Curves

We have integrated Hamilton's equations of motions along with the variational equations (2.2) given in Section 2.1.1 for the initial conditions corresponding to two chaotic and one periodic trajectory for hydrogen in CP field. In Figure 4.2 we observe the evolution of the FLI with time for these trajectories. Up to time $t = 20$ all the curves are almost indistinguishable and show logarithmic behavior with time. At time $t = 20$ the FLI curve (b) for a strongly chaotic trajectory starts to deviate from the other two curves, which continue to demonstrate logarithmic growth with time. After a time $t = 60$ the (b) curve for a weakly chaotic trajectory starts to deviate from logarithmic behavior of the (c) curve. At the end of interval $t = [0,\ 90]$ the FLI curves for the chaotic trajectories reach value

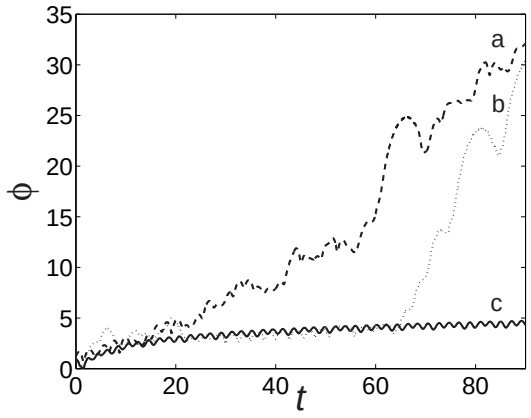

Figure 4.2: FLI versus time curves for two chaotic and one periodic trajectory of hydrogen atom in CP microwave field. The amplitude of the electric field is $F = 0.117$ and initial energy is $K_{max} = -1.3807, B = 0$. Initial conditions (x, y) for the corresponding trajectories are: a) (1.5, 0.01), b) (0.9,0.01), and c) (0.8, 0.01).

$\phi \sim 30$ whereas the curve for the periodic trajectory remains low at $\phi \sim 5$. Analyzing a large number of trajectories we have noticed that two types of FLI behaviors described in Figure 4.2 are characteristic for most of the trajectories from the phase space of the system. In fact, already at time $t = 100$ the FLI curves for chaotic trajectories can be clearly distinguished from the corresponding curves for periodic trajectories. These observations justify the use of integration interval $t = [0, 100]$ as a test interval for obtaining sufficient information about the characteristic dynamical behaviors of analyzed trajectories.

4.3.2 Choice of Initial Conditions Subspace

The ionization dynamics of hydrogen atom in elliptically polarized fields is studied by applying FLI stability analysis for trajectories from a mesh 200×200 initial conditions defined on the $x - y$ plane. In the case of a time–independent Hamiltonian system we view dynamics on a subspace of initial conditions previously used in [80]. Initial energy is fixed at maximum value of the ZVS $K(0) = K_{max}$. Initial momenta p_x, p_y are chosen to satisfy the constraint $p_x x + p_y y = 0$. By substituting $p_x = -p_y \frac{y}{x}$ into the expression for the effective Hamiltonian (4.10) one gets a quadratic equation for initial momentum p_y:

$$\frac{1}{2}\left(1 + \frac{y^2}{x^2}\right) p_y^2 + (1 + \frac{1}{2}B)\left(\frac{y^2}{x} + x\right) p_y - \frac{1}{r} + \frac{1}{8}B^2\left(x^2 + y^2\right) - K(0) = 0 \ , \qquad (4.14)$$

where (x, y) is an arbitrary point from the configuration space of the system satisfying the relation $x \neq 0$.

In the CP field case the subspace of initial conditions defined above is two–dimensional and coincide with two–dimensional Poincaré surface of section. In the EP field case the system has additional degrees of freedom due to time–dependence of Hamiltonian (4.10). In order to reduce the subspace of initial conditions to two–dimensional surface we introduce two additional constraints. The initial generalized coordinate w is taken to be zero and initial generalized momentum is $p_w = -K(0)$. Similarly to the CP problem the dynamics for the EP problem is visualized on the $x - y$ plane. For the semi–parabolic coordinates initial conditions can be defined in terms of coordinates (x, y) as follows:

$$u_0 = (\sqrt{x^2 + y^2} + x)^{\frac{1}{2}}, \qquad v_0 = (sgn\ y)(\sqrt{x^2 + y^2} - x)^{\frac{1}{2}} \tag{4.15}$$

The corresponding initial momenta are determined from the conditions $H_{eff} = 0$ and $u_0 p_{u0} + v_0 p_{v0} = 0$ as follows:

$$\begin{aligned} p_{u0} &= -\frac{1}{2} v[(1 + \frac{1}{2}B)(u_0^2 + v_0^2) - \delta(u_0, v_0)] \\ p_{v0} &= \frac{1}{2} u[(1 + \frac{1}{2}B)(u_0^2 + v_0^2) - \delta(u_0, v_0)] \ , \end{aligned} \tag{4.16}$$

where $\delta(u_0, v_0) = [(1 + B)(u_0^2 + v_0^2) - 8p_w - 4F(u_0^2 - v_0^2) + 16(u_0^2 + v_0^2)^{-1}]^{1/2}$.

4.3.3 Stability Analysis for Circularly and Linearly Polarized Fields

In this section, we present and explain the FLI stability results for the LP field case. For every initial condition the Hamiltonian equations of motions were integrated at the same time with the equations for tangent vector (2.2) over the interval of time $t = [0,\ 1]$ (in atomic units). The FLI $\phi(t)$ defined in (2.4) was evaluated at each moment of time. The maximum value of the FLI attained over the integration interval $[0, 100]$ was mapped onto the FLI plot. In Figure 4.3 the resulting FLI contour plots are shown for several distinct amplitudes of a scaled electric field. The polarization $\alpha = 0$ and the magnetic field $B = 0$. Color code is assigned according to the maximum value of the FLI evaluated for each trajectory. Blue color corresponds to the low values of the FLI and is attributed to regular behavior of trajectory meanwhile yellow and red color indicates high values of the FLI and

chaotic behavior of trajectory. All the trajectories that ionize quickly are discarded from the calculations. They are not marked on the plot. In addition, strongly chaotic trajectories with the value of the FLI greater than the critical value $\phi_c > 50$ were discarded. In most cases strongly chaotic trajectories with $\phi(100) > 50$ escape to infinity and ionize over the finite–time interval $0 < t < 100$.

In the FLI contour plots presented in Figure 4.3 two islands of regular motions can be clearly distinguished. In fact, we have observed that the similar structure of the FLI plots exists for electric field amplitudes in the interval $[0.117,\ 0.2]$. The central and the left islands are located at the center and at maximum of the ZVS correspondingly (see Figure 4.1). The structure of the central island does not change with the increase of the amplitude of the field. This island is constituted by the bounded states that remain stable for a given range of field's amplitude. A layer of chaotic motions is situated around the edges of the main stable islands. By comparing the FLI plots on Figure 4.3 with the zero–velocity contour plot in Figure 4.1 we observe that the stable island on the left is situated exactly in the vicinity of the Lagrange maximum. The area and the structure of the island changes with the increase of the amplitude. It remains almost the same for the field amplitudes $F = 0.117$ and $F = 0.13$. The size of the island visibly decreases at $F = 0.16$ and completely disappear at $F = 0.2$. These changes are the consequence of breaking–up of resonant tori within the island. With the increase of field's amplitude some of resonances within the island lose stability and vanish, in this way, opening the path for chaotic orbits to escape from the vicinity of the Lagrange maximum and to ionize.

In Figure 4.4 the FLI plots are shown for the CP problem. First, one observes that in all four plots the size of stability island around the Lagrange maximum is much smaller than the size of similar structure for the LP problem. Second, the size and structure of the central island looks exactly the same as for the LP case. Our calculations show that for the CP problem the bounded states inside the central island remains stable for all the field amplitudes from the interval $[0.117,\ 0.2]$. For the CP problem the field amplitude, for which all the trajectories from the left island ionize ($F = 0.15$) is lower than the threshold field ($F = 0.2$) for the LP case. As was mentioned before, for the CP field the system is

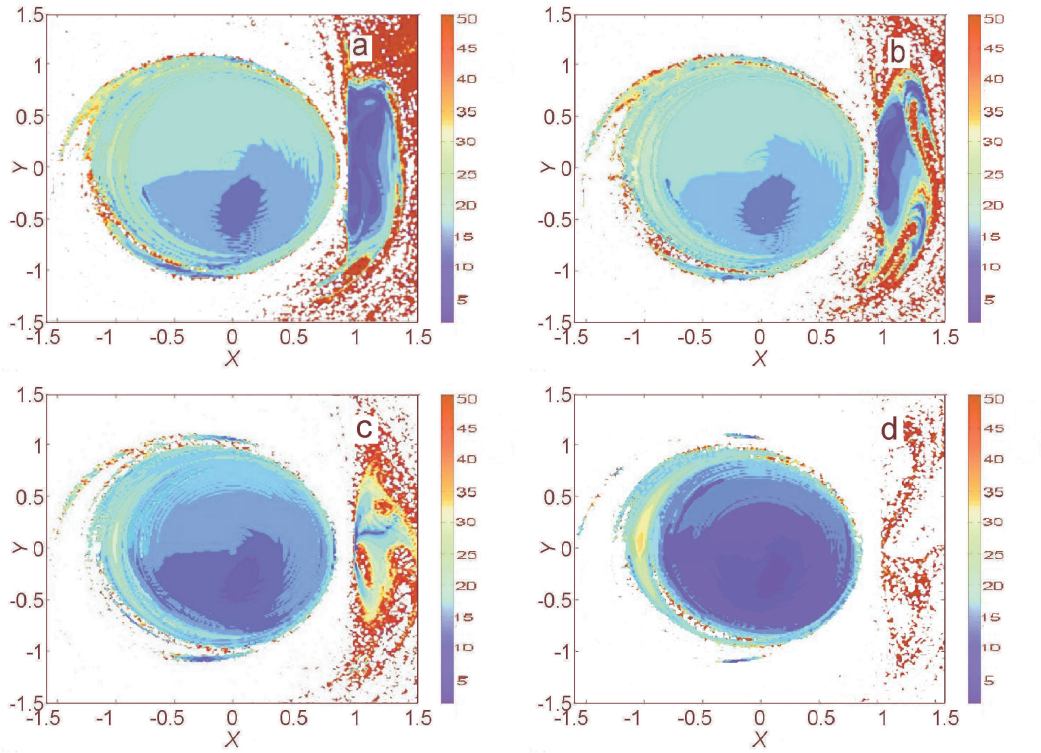

Figure 4.3: FLI stability plots for hydrogen in LP microwave field. The scaled amplitudes of the electric field F are: a) 0.117, b) 0.13, c) 0.16, and d) 0.2. $K_0 = -1.3807, B = 0$

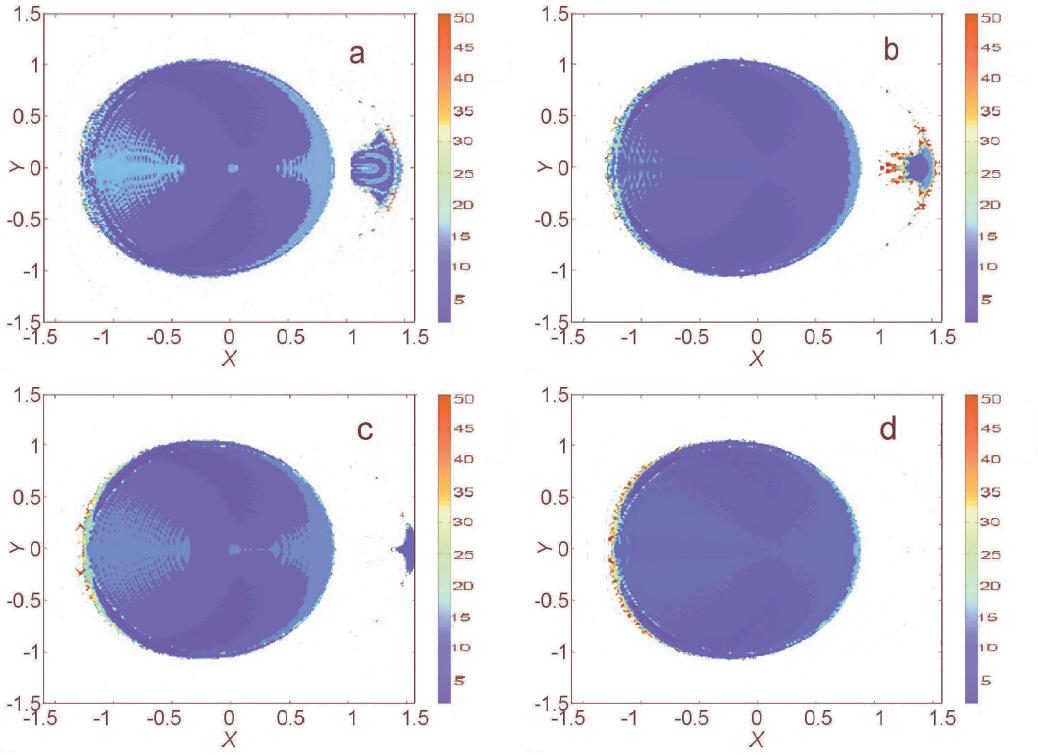

Figure 4.4: FLI stability plots for hydrogen in CP microwave field. The color code from blue to yellow and red is assigned according to the values of the FLI. The scaled amplitudes of the electric field F are: a) 0.117, b) 0.13, c) 0.14, and d) 0.15. $K_0 = -1.3807, B = 0$.

time–independent in the rotational frame, and the subspace of initial conditions corresponds to two–dimensional Poincaré surface of section. Moreover, the stability structure shown on contour plots for the CP field coincides with the Poincaré surface of section structure. As an example, in Figure 4.5 the Trojan bifurcation is shown on the SOS ((a) panel) and on the FLI contour plot ((b) panel). Figure 4.5 (b) is the magnification of the small stability island from Figure 4.4 (a).

A one–to–one correspondence of both plots is evident. On a close inspection, the symmetry about y axis is observed. The resonant zones on the SOS correspond to the blue color coded islands of stability on the FLI plot. The chaotic zones are marked around the edges of the stability islands.

It should be noted, that there are no strict criteria to define ionization for the classical trajectory of hydrogen in EP field. We use the conventional criteria for the classical ionization accepted in the literature [53] and consider that the ionization occur at the time when

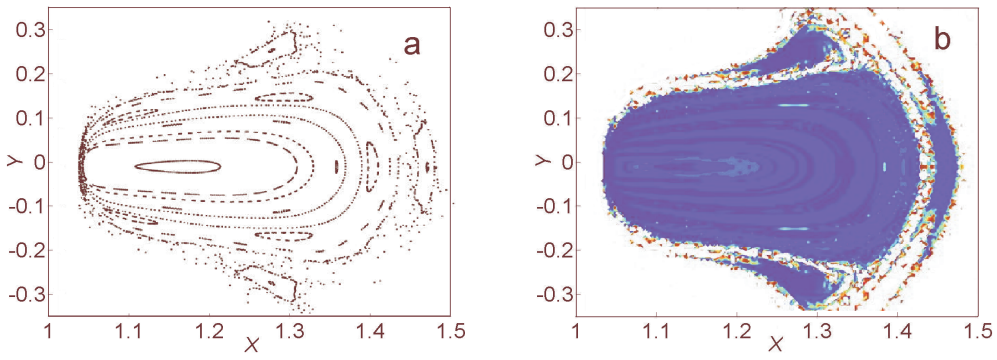

Figure 4.5: The Poincaré surface of section and magnification of the small island from Figure 4.4 are shown on panels (a) and (b) correspondingly.

phase space trajectory reaches high values of classical action. In the real experiment the ionization is defined by the cut-off quantum number $n = 100$. It was emphasized before that at maximum of the ZVS all chaotic trajectories are considered as possible candidates for ionization. Therefore, another criterium for ionization is defined by the FLI stability calculations that distinguish chaotic from regular trajectories.

To illustrate the FLI stability results, we show ionization dynamics for two trajectories with initial conditions inside stable regions on the FLI plot in Figure 4.4 (a) and one trajectory with initial condition inside chaotic region on the same plot. In Figure 4.6 the configurations of three trajectories versus the ZVS surface are shown in the rotational frame. Initial conditions are chosen from different regions in Figure 4.4: big stable island for orbit (a), small stable island for orbit (b), and chaotic region for orbit (c). The first two orbits corresponds to the low eccentricity bounded states and the last orbit is chaotic and ionizes after several close approaches with the nucleus.

4.3.4 Stability Analysis for Elliptically Polarized Field

In Figure 4.7 the FLI plots illustrate stability structures for hydrogen in EP field for the polarization $\alpha = 0.6$. The scaled amplitude of electric field is considered in the interval $F = [0.117,\ 0.17]$. In general, the structure of the FLI plots for the EP problem appear to be similar to the stability plots for the CP problem. Two islands of stability are apparent: a big island located at the center of the ZVS and a small island located at maximum of the

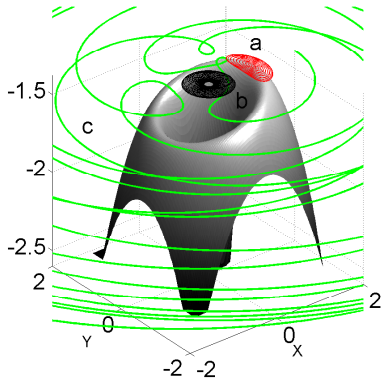

Figure 4.6: Two stable trajectories (a), (b), and one ionizing trajectory (c) versus zero–velocity surface. $K = K_{max},\ F = 0.117,\ B = 0,\ \alpha = 1.$

ZVS (see Figure 4.1). The ellipticity of the field destroys the symmetry in the dynamics that is present for the CP field case. It is evident that the left island structure in Figure 4.7 (c) is not symmetric around y axis as opposed to the structures of the stability island around the maximum in Figure 4.4. Trajectories with the values of the FLI higher than the critical value $\phi_c = 50$ are discarded. It can be observed that the area surrounding two stable islands consists of chaotic motions that quickly ionize. The central island of stability observed in Figure 4.7 remains essentially unchanged with increasing strength of the field. At the same time noticeable changes are seen in the size and structure of the small island on the left. The increase of the size of small island at certain amplitudes is accounted for the stabilization of some resonant motions within the island. For example, at the amplitude of the field $F = 0.13$ the size of the island is noticeably larger than at $F = 0.117$ (see contour plot in (a)). At $F = 0.17$ small island vanishes, and invariant tori within the island that existed at lower amplitudes of electric field lose stability. All regular trajectories found in the vicinity of the Lagrange maximum become chaotic and ionize at $F = 0.17$. For the EP problem the FLI stability plots provide pictures of dynamics that are seen to be more regular than for the same values of the field amplitude for the CP problem. For example, the size of the stability zone around the maximum point in Figure 4.7 appear to be visually larger than the size of the stable zone in Figure 4.4. On the other hand the size of the left island in Figure 4.7 for the EP field is much smaller than the size of the corresponding island in Figure 4.3 for

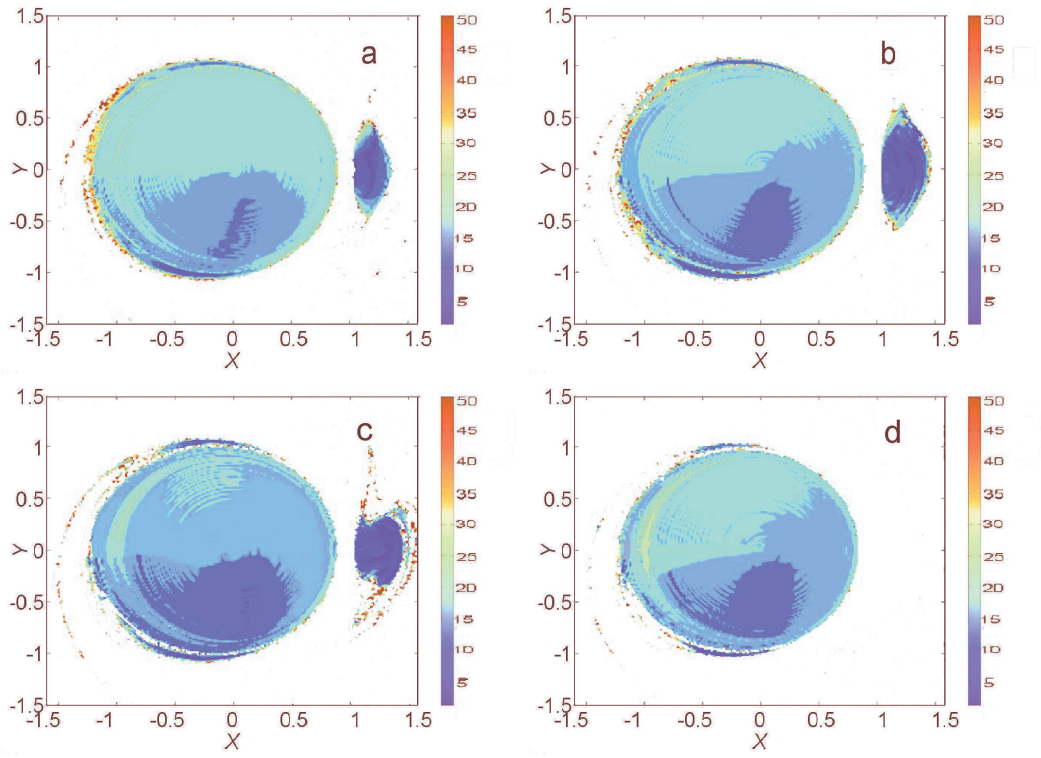

Figure 4.7: FLI stability plots for hydrogen in EP microwave field. The scaled amplitudes of the electric field F are: a) 0.117, b) 0.13, c) 0.15, and d) 0.17. $\alpha = 0.6$, $B = 0$, $K_0 = K_{max} = -1.3807$.

the LP field. From our detailed examination of the FLI results for initial energy equal to maximum of the ZVS we conclude that phase space dynamics is more regular for the LP problem than for the EP and CP problems cases. Moreover, for the EP problem the size of the stability region around the Lagrange maximum is observed to vary non–monotonically with the increase of electric field amplitude. These changes are ascribed to various nonlinear resonant effects that were studied classically by Richards in [59] and quantum mechanically using Floquet states approach by Oks and Uzer in [67].

4.3.5 Study of Ionization Probability Curves

It has been pointed out in [77] that the apparent ionization threshold for Rydberg atoms in the CP microwave fields must be determined by fraction of orbits that undergo first transition to chaos. Such orbits were found to be located outside of the ZVS and they represent atomic states that can be easily populated in the experiment [60]. In connection with these findings we found a set of bounded orbits in the vicinity of the Lagrange maximum. These are the orbits that undergo transition from regular to chaotic behavior for electric field in the interval $F = [0.12,\ 0.18]$. The FLI plots in Figures 4.3,4.4 and 4.7, which are calculated for the linear ($\alpha = 0$), the circular ($\alpha = 1$), and intermediate ($\alpha = 0.6$) polarizations, illustrate the changes in the stability of these orbits. While the dynamics in the central island remain intact by the increase of perturbation of the field, the orbits situated near the Lagrange maximum become chaotic and ionize with the increase of the field amplitude. For this reason, we determine apparent ionization threshold by measuring the fraction of chaotic orbits from the phase space volume enclosing the Lagrange maximum. The calculations of ionization probabilities are carried out for polarizations of the field from the circular to the linear limit ($0 < \alpha < 1$). The behavior of ionization yields versus scaled electric field amplitude $F = [0.12,\ 0.18]$ is estimated by FLI stability analysis.

In the calculations of ionization probabilities we use the classification of dynamics established by the FLI stability method. By monitoring the evolution of the FLI along each integrated trajectory we count the number of chaotic trajectories with the FLI value equal to or greater than the critical value $\phi_c = 50$. All the chaotic trajectories are considered

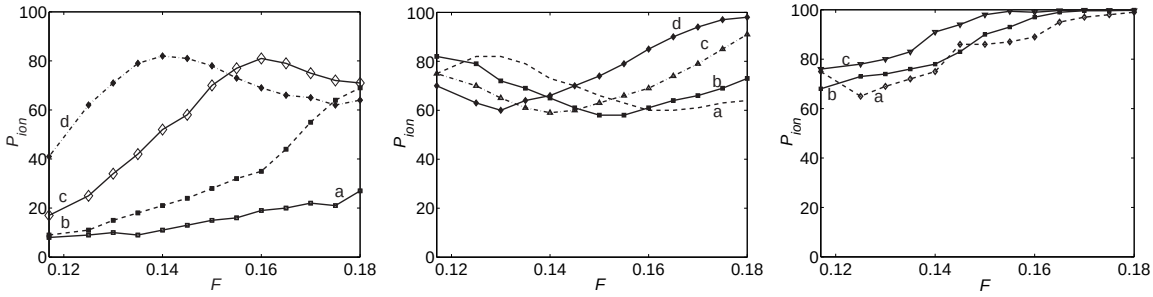

Figure 4.8: Ionization probability curves computed for the ensemble of trajectories of hydrogen in the EP microwave electric field. $B = 0, K(0) = K_{max} = -1.3807$. Left: ionization yields for the field polarizations close to the LP limit: a) 0, b) 0.1, c) 0.2, and d) 0.3. Center: Ionization yields for the intermediate values of the field polarization: a) 0.4, b) 0.5, c) 0.6, and d) 0.7. Right: Ionization yields for the field polarization close to the CP limit: a) 0.8, b) 0.9, and c) 1.

as possible candidates for the classical ionization. The FLI plots in Figures 4.3, 4.4 and 4.7 show that the phase space surrounding the stability island at the Lagrange maximum is chaotic. There are no stability structures (except the stability island at the center) that can prevent the escape of chaotic trajectories and their subsequent ionization. Indeed, the absence of invariant tori outside of two stable structures on the FLI plots demonstrates the possibility for chaotic trajectories to escape from the vicinity of the Lagrange maximum to a region of the phase space associated with high classical action values.

The probability of ionization is measured as the ratio of number of chaotic trajectories N_{chaot} to the total number of trajectories N_{total} from the volume of phase space surrounding the maximum point:

$$P_{ion} = \frac{N_{chaot}}{N_{total}}. \tag{4.17}$$

The resulting apparent ionization yields versus scaled field amplitude are shown in Figure 4.8. Each curve represents ionization probability for different field's polarization. On the left panel of Figure 4.8 the ionization yields are shown for the polarizations of the field close and equal to the LP limit. The (a) curve indicates the percentage of chaotic trajectories in the vicinity of the Lagrange maximum for the LP field. It is clearly seen that on the average the percentage of chaotic trajectories within the phase space volume around the Lagrange maximum point is below 20%. The ionization yield (a) increases slowly with the

increase of the electric field's amplitude. It is evident, that for the LP limit dynamics around the Lagrange maximum remains predominantly regular for the electric field amplitude in the interval $F = [0.12, 0.18]$. A qualitative illustration of changes in dynamics for the LP limit is given in Figure 4.3. From this figure one observes that transition from regular to chaotic dynamics around Lagrange maximum occurs at the field amplitude $F = 0.2$. On the left panel of Figure 4.8 sharp changes in the behavior of the (c) and (d) curves are observed for the polarizations $\alpha = 0.2$ and $\alpha = 0.3$ correspondingly. First, the (c) and (d) curves increase rapidly from 20% and 40% at $F = 0.117$ to 80% at higher field amplitudes. Second, ionization yields (c) and (d) exhibit non–monotonic rise with the increase of the field amplitude. Two pronounced local maxima of the ionization yields are observed for $F = 0.16,\ \alpha = 0.2$ and for $F = 0.14,\ \alpha = 0.3$. The main feature of the ionization yields for the polarizations close to $\alpha = 0$ is the sharp transition from almost monotonic behavior of the yields for $\alpha = 0$ and $\alpha = 0.1$ to the non–monotonic behavior of the yields for $\alpha = 0.2$ and $\alpha = 0.3$. This indicates strong dependence of dynamics around the Lagrange maximum on the changes of field's polarization.

On the central panel the ionization yields are shown for intermediate polarizations. The behavior of ionization yields is non–monotonic. For instance, there is a local maximum at $F = 0.13$ and local minimum at $F = 0.162$ along the (a) curve. On the average the percentage of chaotic trajectories in the vicinity of the Lagrange maximum is equal to 80%. In fact, for the field $F = 0.18$ and polarization $\alpha = 0.6$ the percentage of chaotic trajectories is almost 90%, which means that most of the orbits around the Lagrange maximum ionize at these parameters of the field. These results were demonstrated previously on the FLI stability plots in Figure 4.7. Close inspection of the left and central panels shows that the yields for the higher polarizations look shifted to the left with respect to the yields for the lower polarizations. For example, the maximum for the (a) curve on the central panel is at $F = 0.13$ and the maximum for the (d) curve from on the left panel occurs at $F = 0.14$.

On the right panel of Figure 4.8 the ionization yields are shown for polarizations of the field close to the CP limit. The fact that ionization yields remain close to each other for polarizations $\alpha \in [0.8,\ 1]$ demonstrates the lack of significant variations in local dynamics

around the Lagrange maximum. The probabilities change from 80% for $F = 0.12$ to 100% for $F = 0.18$. Moreover, the ionization curves increase monotonically with increasing field's amplitude. For the CP limit all the trajectories around the Lagrange maximum become chaotic and ionize at $F = 0.15$. This is the lowest ionization threshold observed from the ionization probability plots on Figure 4.8.

4.4 Phase Space Dynamics below the Lagrange Saddle

In this section we discuss FLI stability results for the ensemble of states with initial energy below the ZVS saddle point and non-zero constant magnetic field that is applied perpendicular to the plane of polarization.

Previously it has been shown in [8, 80] that for hydrogen in CP field the application of magnetic field perpendicular to the polarization plane leads to stabilization of some of phase space invariant tori. In turn, the invariant tori create barriers to diffusion of chaotic trajectories inside the phase space. Motivated by these findings we perform FLI stability analysis for hydrogen in EP microwave field and non–zero magnetic field. As a starting point, the FLI stability analysis is applied to hydrogen in CP field. The FLI calculations are carried out on a grid of points on the $x - y$ plane. Magnetic field is taken to be $B = 0.2$ and initial energy $K_0 = -2$ is below the saddle point energy (the saddle point value of the ZVS is $K_{sad} = -1.7022$). The resulting data from the FLI stability analysis are shown in Figure 4.9.

On (a) panel the structure of the phase space is shown for the CP field. One observes the island of stability (blue color code) around the nucleus. The same stability island was observed in Figures 4.3, 4.4 and 4.7 around the center of the ZVS. The island is surrounded by the classically inaccessible region. The phase space outside of the region is foliated by regular and chaotic regions. Chaotic dynamics is associated with high values of the FLI (yellow and red color code). The phase space appears to be mostly regular, except for a few thin chaotic layers winding around regions of stability. It is easy to notice, that the structure is symmetric with respect to y axis. On (b) panel the phase space dynamics is pictured for the polarization of the field $\alpha = 0.8$. The structure of the phase spaces resembles the one

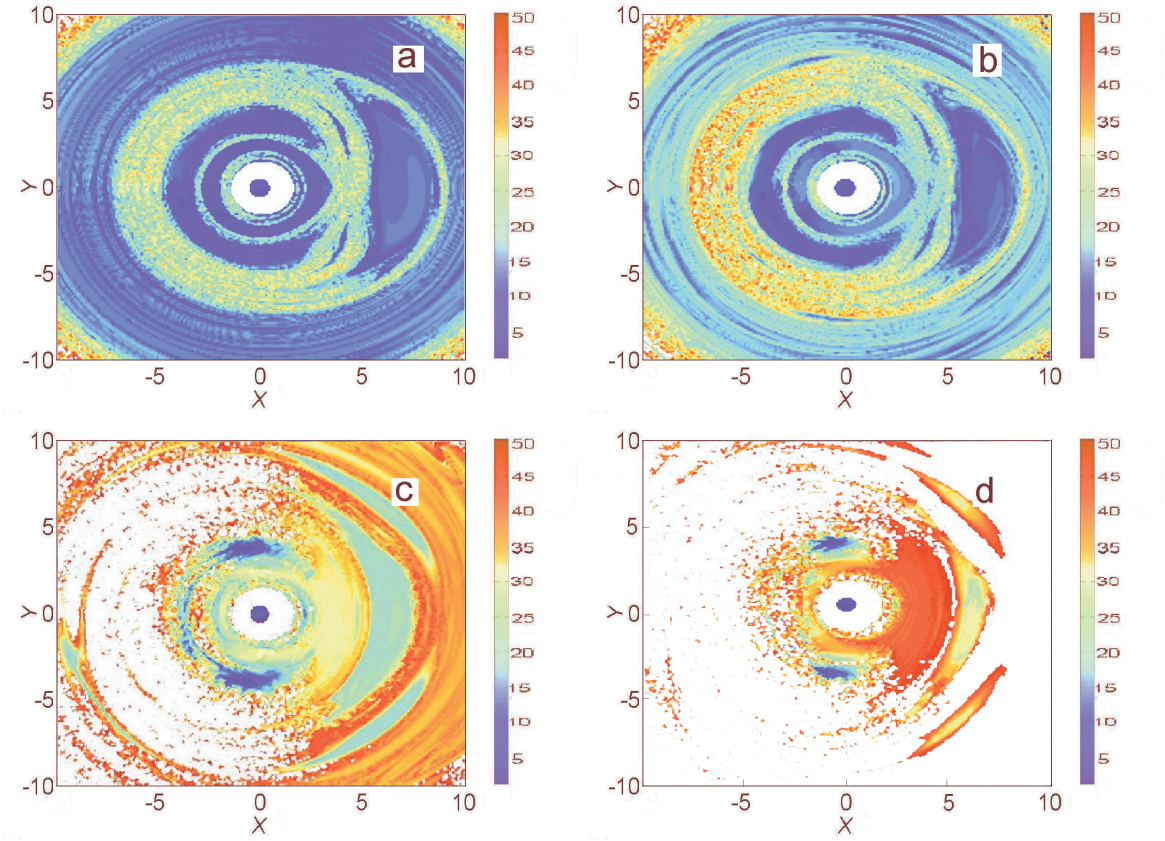

Figure 4.9: FLI stability plots for hydrogen in EP microwave field. $F = 0.117$, $B = 0.2$, $K = -2$. The field polarizations are: a) 1, b) 0.8, c) 0.5, and d) 0.3. The color code is assigned according to the maximum values of the FLI attained over the integration interval $t = 100$.

shown on (a) panel. However, the overall dynamics appears to be more chaotic than for the CP field case. The stability results for the intermediate polarizations $\alpha = 0.5$ and $\alpha = 0.3$ are shown on the (c) and (d) panels correspondingly. The phase space dynamics in both plots appears to be much more chaotic than the dynamics for the CP limit.

Our main observation from the FLI stability results described in this section is that the application of magnetic field leads to stabilization of resonant structures in phase space of the system. The FLI plots reflect the onset of stochasticity in phase space that occurs when polarization of the field is close to the LP limit. The phase space structure appears to be more regular for the field polarizations close to the CP limit as opposed to the polarizations close to the LP limit.

4.5 Configuration of the Initial Ensemble of States

In this section we provide a qualitative information about the character of states that determine the low bound for the ionization threshold. In addition, we discuss the relation between the configuration of initial states and data of FLI stability analysis presented in the previous sections.

In the actual experiment [60] the ensemble of initial states are prepared spanning a narrow range of Keplerian energy $E = -\frac{1}{2n^2}$ and a variety of high eccentricity orbits. As the field is turned on the states with the same action n will appear in different regions of the phase space having different values of energy and eccentricities $\epsilon = \sqrt{1 - l_z^2/n^2}$ in the rotating frame. While the Hamiltonian dynamics is traditionally studied by restricting the phase space to the constant energy manifold, one would ideally prefer to relate numerical results with the experiment and to study an ensemble of states with the same Keplerian energy. However, most of the numerical simulations based on the examining the structure of the Poincaré surfaces of section use trajectories with different values of Keplerian energy K. For the FLI stability analysis we use an ensemble of initial states with equal initial energies $K(0)$ and different values of initial action n and eccentricities ϵ. The reason for our choice of initial states is dictated by the possibility to compare the stability pictures given by the FLI method with the SOS.

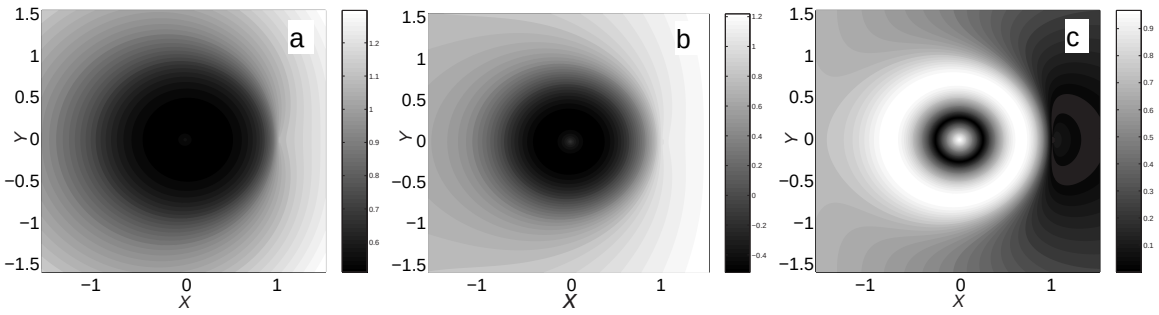

Figure 4.10: The action variable n, angular momentum L_z, and eccentricity ϵ of the initial states of hydrogen in the EP microwave field are shown on $(a), (b)$, and (c) panels correspondingly. $F = 0.117, K_{max} = -1.3807, B = 0$.

The interpretation of numerical results and their connection to the real experiment is much more complicated in the EP field case. The presence of the time–dependent term in the expression of the Hamiltonian in the rotational frame prevents the direct relation between the initial state (at time $t = 0$) and final state (obtained after the turn–on of the field). Therefore, it is instructive to relate the FLI stability results for the ensemble of states analyzed with their initial eccentricities, actions and angular momentum values. The importance of the initial ensemble state geometry in the ionization mechanism was realized by many authors [77, 85]. We found that our results agree in their key features with the conclusion stressed out in reference [85]: the fate of the initial states subjected to the application of the field cannot be predicted based only on the known initial action values and eccentricities of such states. In an essence, the states of the same initial action and eccentricity values can be switched by the application of the field to different parts of the phase space. We illustrate these conclusions by comparing FLI stability results given in Sections 4.3.3 and 4.3.4 with the configuration of initial states involved in the FLI calculations.

First, we analyze the ensemble of states with initial energy equal to the Lagrange maximum. In Figure 4.10 the action variables n, angular momenta l_z and eccentricities ϵ are calculated for the ensemble of initial states used for the FLI stability analysis in Section 4.3.4. The case of zero magnetic field is considered. The scaled amplitude of the electric field is $F = 0.117$, polarization is $\alpha = 1$, and the initial energy value is equal to the maximum

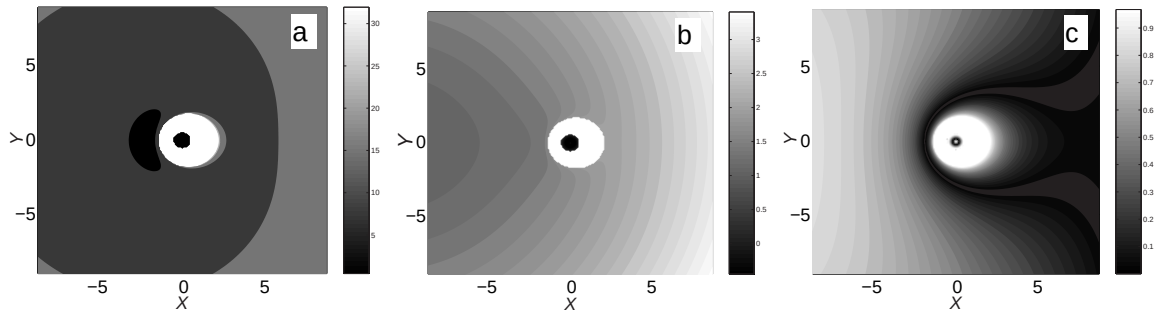

Figure 4.11: The action variable n, angular momentum L_z, and eccentricity ϵ of the initial states of hydrogen in the EP microwave field are shown on $(a), (b)$, and (c) panels correspondingly. $F = 0.117, K = -2, B = 0.2$. The initial energy of the states K is taken below the saddle point energy $K_{sad} = -1.7022$.

($K_{max} = -1.3807$) of the ZVS defined in equation (9). The (b) panel shows the values of initial angular momentum l_z. It can be seen from Figure 4.10 (b) and FLI plots in Figure 4.7 that the states inside the central island of stability correspond to negative angular momentum states. The rest of trajectories in the FLI plots in Figure 4.10 correspond to positive angular momentum initial states. Another important observation is that the central island of stability is associated with bounded states of different eccentricities. From the stability results given in Section 4.3.4 we know that these states remain bounded for the range of the scaled field amplitude $F \in [0.117, 0.2]$ and different polarizations of the field considered in our calculations. From Figure 4.10 (c) and FLI plots in Figure 4.7 it is apparent that initial states around Lagrange maximum are the low eccentricity states. In fact, these are the states that determine the low ionization threshold calculated in Section 4.3.5. Summarizing data given in Figures 4.7 and 4.10 we argue, that the ultimate fate of initial low eccentricity and positive angular momentum states is to be switched by the driving field to the chaotic region of the phase space and undergo fast ionization. At the same time, the initial states with negative value of angular momentum located around the center of the ZVS remain bounded.

Next, we classify the initial states with energy below saddle point of the ZVS. In Figure 4.11 the action, angular momentum and eccentricities together with the FLI plot are

presented for the initial states of hydrogen subjected to EP field $F = 0.117$ with polarization $\alpha = 0.9$ and magnetic field $B = 0.2$. The initial energy ($K(0) = -2$) is chosen below saddle point ($K_{sad} = -1.7022$) of the ZVS. The main conclusion from the data given in Figures 4.9 and 4.11 is that the initial states with low eccentricity tend to be more stable than the states with high eccentricity values. For example, from Figure 4.9 (d) one observes three small stable islands with the low values of the FLI: one island is around the center of the ZVS and the other two islands are symmetric with respect to y–axis. Two symmetric islands correspond to the low eccentricity states in Figure 4.11 (c).

A comparison of data presented in this section with the stability results given by FLI analysis in Sections 4.3 and 4.4 shows that, although, in some cases the fate of initial states can be determined from their eccentricities and angular momentum values, in general, this information is not sufficient for predicting dynamics of states after the turn–on of the field. Instead, the characterization of initial states should be carried out together with stability analysis.

4.6 Conclusions

We provide a qualitative description of the classical phase space of hydrogen atom in a strong EP microwave field and its relevance to ionization dynamics by means of the FLI stability analysis. The complex multidimensional dynamics is shown to depend sensitively on changes of parameters including polarization, amplitude of the electric and magnetic fields as well as energy of initial states used in the classical calculations. The FLI stability analysis pictures complex phase space structures, such as important resonant and chaotic zones. Unlike other analytical and numerical techniques used to study multidimensional dynamics of hydrogen in EP field, the FLI method provides stability estimates for different regimes of the system without making reduction to lower–dimensional dynamics.

The essential advantage of the technique versus other available analytical and numerical methods is its independence on dimension of system studied. Thus, the stability analysis can be carried out for any subspace of initial conditions in a full dimensional phase space of the hydrogen in EP problem. The application of the FLI technique can provide a useful

insight into the classical phase space dynamics. It gives estimates of the size of regular versus chaotic zones in the phase space of the system for almost any choice of parameters.

To answer a long standing controversy about the character of states that are more favorable to ionization by the low field amplitude we described ensembles of states used in FLI stability calculations in terms of their initial eccentricities, action and angular momentum values. We mapped out the FLI values for each trajectory originated on the zero–velocity subspace for two distinct sets of initial states: states with initial energy at the Lagrange maximum and below the saddle point of ZVS. Our FLI stability calculations carried out for LP and CP fields reveal two main resonant structures: small resonant island around the Lagrange maximum and large resonant island around the center of the ZVS. The small island corresponds to initial states with low eccentricity values. The big resonant island consists of initial states with different eccentricities and negative angular momentum values. These states remain bounded for the amplitudes of electric field studied. The remaining part of the phase space is attributed to chaotic motions that ionize over a short–time interval. The main feature observed from the FLI stability results is that phase space volume related to low eccentricity and positive angular momentum initial states decreases with the increasing amplitude of the field. Hence, these states are first to become chaotic and ionize for a given strength of electric field. Similar observations hold true for the EP problem. Although the ZVS for the EP problem is not fixed in the rotational frame, the stable structures, similar to those observed for the LP and CP problems, are present. The main difference from the LP and CP results is in behavior of stability island around the Lagrange maximum. The size of the island changes non–monotonically with increasing electric field amplitude. These changes have been attributed in the literature to the effect of resonances produced by driving field and Stark states for the EP problem. In the FLI stability results this effect manifests in breaking up and stabilization of resonant tori structures around the Lagrange maximum.

Our main conclusion is that stability of the Lagrange maximum is determined by parameters of the field, such as amplitude of electric field as well as polarization degree of the

field. The ionization yields versus amplitude of electric field for different polarization degrees were computed using fraction of regular trajectories around the Lagrange maximum. The main feature of ionization yields is their non–monotonic growth for intermediate ellipticities of electric field. These results confirm experimentally calculated ionization yields for the elliptically polarized field problem [60].

The FLI stability analysis was carried out for the ensemble of states with initial energy below saddle value of the ZVS. The FLI plots reflect the onset of stochasticity in phase space of the system that happens when the field polarization changes from circular to linear limit. The FLI simulations reveal the detailed structure of the phase space that is more regular for polarizations close to the circular limit as opposed to polarizations near to the linear limit.

In connection with the quantum wavepacket calculations and stabilization of Trojan states at the Lagrange equilibria points the method can be useful for estimating the size of stability zones around the Lagrange maximum. We argue that by varying polarization and amplitude of electric and magnetic fields one can achieve stabilization of the set of resonances around the maximum point that can possibly lead to stabilization of the quantum wavepackets at the Lagrange maximum.

CHAPTER V

GENERAL CONCLUSIONS

In this work we presented results of a qualitative analysis of phase space stability structures for two multidimensional non–integrable Hamiltonian systems: the highly excited planar OCS molecule and the hydrogen atom in elliptically polarized microwave fields. The structure of phase space determines character of dynamics of each system. This study is focused on the application of rigorous computational methods to treat the multidimensional systems in strongly perturbative regimes. The molecular system of planar OCS and atomic system of hydrogen in EP microwave fields are treated for different energy regimes. These includes highly excited regimes of classical ionization of hydrogen and dissociation of molecular system of OCS. We showed that for the Hamiltonian systems in a far–from–integrable regimes the application of fast Lyapunov indicator method together with time–frequency analysis provide a clear qualitative description of the dynamics.

The evidence that resonant structures and transitions between them determine dynamical behavior of low dimensional collinear OCS model is abundant in the literature. In this work we characterized the set of main resonances for the planar OCS model for energies below and at dissociation energy. By using time–frequency information obtained for periodic, quasiperiodic and chaotic trajectories the important features of chaotic transport in phase space of the system have been observed.

Despite considerable progress in understanding vibrational dynamics of the molecular system of OCS in strongly perturbed regimes, there are still open problems. One of them is to find exact topological structures of invariant tori that are responsible for a long–time energy relaxation in the planar OCS system. Another problem is to identify the structure of transition to the dissociation state that regulates the mechanism of molecular dissociation.

The results of classical stability analysis carried for hydrogen in EP microwave fields demonstrate a strong sensitivity of system's dynamics on the parameters of applied field,

such as polarization, amplitude of electric and magnetic field. A strong dependence of the dynamics on parameters of the field is accounted for effects of nonlinear resonance. The stabilization and break–up of resonant structures observed in the classical stability calculations are related to the multi–quanta resonances produced by Stark states and driving field frequencies for the quantum counterpart of the system. A qualitative analysis of initial ensemble of orbits used in the stability calculations shows that high eccentricity and positive angular momentum orbits will ionize at the lowest amplitudes of electric field. This leads to the conclusion that effect of collisions with the core is the most relevant to ionization scenario.

Our future investigation on hydrogen in electromagnetic fields problem is concentrated on extending stability analysis to classical regimes of the system, which were not studied in the scope of this work. The scenario of classical ionization via stochastic diffusion in phase space needs better understanding. To be specific, we expect that similarly to the role played by invariant phase space structures in intramolecular relaxation dynamics of the OCS model, for atomic system of hydrogen in EP fields high dimensional invariant tori are relevant to trappings of chaotic trajectories and slowing rates of ionization within multidimensional phase space of the system.

Apart from the importance of our stability analysis for undermining complex dynamics of a general high–dimensional Hamiltonian system, we hope that our results will prompt other researchers to explore structurally similar polyatomic and atomic systems in the classical regimes.

APPENDIX A

INSTANTANEOUS FREQUENCY EQUATION

In this section the detailed derivation of the instantaneous frequency equation for the special class of signals is presented. This is an important class of signals representing solutions of the Hamiltonian equations given in (2.12). Any signal from this class can be obtained from the linear combination of solutions of the Hamiltonian equations and can written in the form:

$$g(t) = \sum_k a_k(t) e^{i\phi_k}, \tag{A.1}$$

where $a_k(t)$ and $\phi_k(t)$ are, respectively, the time–dependent amplitude and the phase for every single k component.

Before considering results for the multi–component signal (A.1) the expression for the wavelet transform and instantaneous frequency equation is derived for a single component signal $f(t) = a(t)e^{i\phi(t)}$. The following theorem allows to obtain the Morlet–Grossman wavelet transform of signal $f(t)$ in a relatively simple form:

Theorem. *For a signal $f(t)$ the continuous wavelet transform at a point (u, s) is:*

$$Wf(u,s) = \sqrt{2s\sigma}\pi^{1/4} a(u) e^{i\phi(u)} \left[e^{-(\eta-\phi'(u)s)^2 s^2\sigma^2/2} + \epsilon \right]. \tag{A.2}$$

The ϵ term is small if the amplitude $a(t)$ and phase $\phi(t)$ vary slowly over the time interval corresponding to the temporal resolution of the wavelet. This interval is equal to $[-\delta/2, \delta/2]$, with $\delta = \sigma s/\sqrt{2}$ for a Morlet–Grossman wavelet.

Proof. Continuous wavelet transform for the signal $f(t)$ around a point (u, s) can be written as follows:

$$\begin{aligned} Wf(u,s) &= \frac{1}{\sqrt{s}(\sigma^2\pi)^{1/4}} \int_{-\infty}^{\infty} a(t) e^{i\phi(t)} e^{-i\eta(t-u)/s} e^{-(t-u)^2/2s^2\sigma^2} dt \\ &= \frac{1}{\sqrt{s}(\sigma^2\pi)^{1/4}} \int_{-\infty}^{\infty} a(t+u) e^{i\phi(t+u)} e^{-i\eta t/s} e^{-t^2/2s^2\sigma^2} dt. \end{aligned} \tag{A.3}$$

By expanding the amplitude $a(t+u)$ and the phase $\phi(t+u)$ of the signal $f(t)$ around the time u, the wavelet transform can be represented as the sum of the integrals:

$$Wf(u,s) = I_1 + I_2 + I_3, \tag{A.4}$$

where

$$\begin{aligned} I_1 &= \int_{-\infty}^{\infty} a(u) e^{i(\phi(u)+\phi'(u)t+\beta(t)t^2/2)} e^{-i\eta t/s} e^{-t^2/2s^2\sigma^2} dt, & \text{(A.5)} \\ I_2 &= \int_{-\infty}^{\infty} a'(u) t e^{i(\phi(u)+\phi'(u)t+\beta(t)t^2/2)} e^{-i\eta t/s} e^{-t^2/2s^2\sigma^2} dt, & \text{(A.6)} \\ I_3 &= \frac{1}{2}\int_{-\infty}^{\infty} \alpha(t) t^2 e^{i(\phi(u)+\phi'(u)t+\beta(t)t^2/2)} e^{-i\eta t/s} e^{-t^2/2s^2\sigma^2} dt, & \text{(A.7)} \end{aligned}$$

and

$$|\alpha(t)| \le \sup_{h\in[u_-,u_+]} |a''(h)|, \qquad |\beta(t)| \le \sup_{h\in[u_-,u_+]} |\phi''(h)|, \tag{A.8}$$

where $u_\pm = u \pm \delta/2$.

To simplify the calculations, the exponential term $e^{i\frac{t^2}{2}\beta(t)}$ can be expanded in a Taylor series:

$$e^{i\frac{t^2}{2}\beta(t)} = 1 + \frac{t^2}{2}\beta(t)\gamma(t), \qquad |\gamma(t)| \le 1. \tag{A.9}$$

Using this expansion and the integral formula

$$\int_0^\infty x^{2n} e^{-px^2} dx = \frac{(2n-1)!!}{2(2p)^n}\sqrt{\frac{\pi}{p}}, \tag{A.10}$$

it is possible to show that the following inequality holds true for the I_1 term in (A.5):

$$|I_1 - \sqrt{2s\sigma}\pi^{1/4} a(u) e^{i\phi(u)} e^{-(\eta - s\phi'(u))^2 s^2\sigma^2/2}| \le \frac{s\sigma^{5/2}\pi^{1/4}}{\sqrt{2}} \sup_{h\in[u_-,u_+]} |\phi''(h)||a(u)|.$$

Similarly, the third integral in the summation (A.4) can be evaluated:

$$|I_3| \le \frac{1}{2}(s\sigma)^{5/2}\pi^{1/4} \sup_{h\in[u_-,u_+]} |a''(h)|(1 + \frac{3}{2}(s\sigma)^2 \sup_{[u_-,u_+]} |\phi''(u)|). \tag{A.11}$$

To evaluate I_2 another integral formula is useful:

$$\int_0^\infty x^{2n+1} e^{-px^2} dx = \frac{n!}{2p^{n+1}}\sqrt{\frac{\pi}{p}}, \tag{A.12}$$

where n is an integer. The estimate for the second integral I_2 is:

$$|I_2| \leq 2\frac{(s\sigma)^{3/2}}{\pi^{1/4}}|a'(u)|(1+2(s\sigma)^2 \sup_{h\in[u_-,u_+]}|\phi''(h)|). \tag{A.13}$$

The expression for the wavelet transform in (A.4) can be now evaluated and written as the sum of two terms:

$$Wf(u,s) = \frac{\sqrt{s\sigma}}{\pi^{1/4}}a(u)e^{i\phi(u)}(\sqrt{2\pi}e^{-(\eta-\phi'(u)s)^2s^2\sigma^2/2}+\epsilon), \tag{A.14}$$

where

$$\epsilon \leq 2\epsilon_{a1} + \sqrt{\frac{\pi}{2}}\epsilon_{a2} + \sqrt{\frac{\pi}{2}}\epsilon_{\phi} + 4\epsilon_{a1}\epsilon_{\phi} + \frac{3}{2}\sqrt{\frac{\pi}{2}}\epsilon_{a2}\epsilon_{\phi}, \tag{A.15}$$

with

$$\begin{aligned}
\epsilon_{a1} &= s\sigma\frac{|a'(u)|}{|a(u)|}, \\
|\epsilon_{a2}| &\leq (s\sigma)^2 \sup_{h\in[u_-,u_+]}\frac{|a''(u)|}{|a(u)|}, \\
\epsilon_{\phi} &= (s\sigma)^2 \sup_{[u-\delta/2,u+\delta/2]}|\phi''(h)|.
\end{aligned}$$

The ϵ–term is small whenever ϵ_{a1}, ϵ_{a2}, ϵ_{ϕ} are small, and $a(t)$, $\phi(t)$ show a very small variations over the time support of the wavelet.

In the derivation of this result, I have followed the original approach introduced by Delprat in [45] and the proof given by Mallat in [14] for a general wavelet $\mathbf{L}^2(R)$ function.

From the expansion of the wavelet transform (A.14) the normalized scalogram can be written explicitly up to the small order ϵ–terms:

$$P_f(u,\xi=\eta/s) = \frac{1}{s}|Wf(u,s)|^2 = 2\sigma\sqrt{\pi}|a(u)|^2\left(e^{(\eta-\phi'(u)s)^2\sigma^2} + O(\epsilon)\right). \tag{A.16}$$

The ridge is located at:

$$\xi = \phi'(u) \tag{A.17}$$

The equation for instantaneous frequency for the multi–component signal can be obtained following essentially the same steps as in the derivation for the single frequency component signal. The wavelet transform defined in is linear. Therefore its expression for a multi–component signal is a sum of wavelet transforms for each single component. Under

the assumptions of the theorem the small order terms can be discarded if the amplitudes $a_k(t)$ and instantaneous frequencies $\phi_k(t)$ of and the expression for the normalized scalogram for signal is presented by the following low order approximation:

$$\begin{aligned}\frac{\sqrt{\pi}}{2\pi\sigma}P_f(u,s) &= \sum_{j=1,n}|a_j(u)|^2 e^{(\eta-\phi_j'(u)s)^2\sigma^2} \\ &\quad +2\sum_{j,k=1,n}|a_j(u)||a_k(u)|\cos(\phi_j(u)-\phi_k(u)) \\ &\quad \times e^{-\{[\eta-\phi_j'(u)s]^2\sigma^2\}/2}e^{-\{[\eta-\phi_k'(u)s]^2\sigma^2\}/2}. \end{aligned} \tag{A.18}$$

The expression for the ridge will be derived near the point $\xi=\eta/s=\phi_1'(u)$. To avoid the interference terms in the final expression for the ridge the remaining $n-1$ frequencies of the signal placed sufficiently far apart and satisfy the bandwidth condition at the point (u,ξ):

$$\frac{|\phi_1'(u)-\phi_j'(u)|}{|\phi_1'(u)|}\geq\frac{1}{\sigma\eta\sqrt{2}},\qquad j=1,\ldots,n. \tag{A.19}$$

By introducing new notation

$$\eta-\phi_j'(u)s=x+(\phi_1'(u)-\phi_j'(u))s,\qquad x=\eta-\phi_1'(u)s, \tag{A.20}$$

and rewriting the exponential terms in their low order Taylor expansions:

$$e^{-x^2\sigma^2}=1-x^2\sigma^2,\qquad e^{-2x\eta\sigma^2[1-\phi_j'(u)/\phi_1'(u)]}=1-2x\eta\sigma^2\left(1-\frac{\phi_j'(u)}{\phi_1'(u)}\right) \tag{A.21}$$

allows one to simplify the expression (A.18) for the normalized scalogram and to write its approximate expansion around the point (u,ξ) in terms of the small parameter x:

$$\frac{1}{2\sqrt{\pi}\sigma}P_f(u,s)=P_0+P_1x+P_2x^2+\mathcal{O}(x^3). \tag{A.22}$$

The coefficients in the expansion are:

$$\begin{aligned}P_0 &= |a_1|^2+\sum_{j>1}|a_j|^2e^{-\eta^2\sigma^2(1-\phi_j'/\phi_1')^2} \\ &\quad +2|a_1|\sum_{k>1}|a_k|\cos(\phi_1-\phi_k)e^{-\eta^2\sigma^2(1-\phi_k'/\phi_1')^2/2} \\ &\quad +\sum_{j\neq k}|a_k||a_j|\cos(\phi_j-\phi_k)e^{-\eta^2\sigma^2(1-\phi_k'/\phi_1')^2/2}e^{-\eta^2\sigma^2(1-\phi_j'/\phi_1')^2/2} \end{aligned} \tag{A.23}$$

$$P_1 = -2\eta\sigma^2\sum_{j>1}|a_j(u)|^2\left(1-\frac{\phi_j'}{\phi_1'}\right)e^{\eta^2\sigma^2(1-\phi_j'/\phi_1')}$$

$$
\begin{aligned}
&-2|a_1|\eta\sigma^2\sum_{k>1}|a_k|\cos(\phi_1-\phi_k)\left(1-\frac{\phi_k'}{\phi_1'}\right)e^{-\frac{(\eta\sigma)^2}{2}(1-\frac{\phi_k'}{\phi_1'})^2}\\
&-\eta\sigma^2\sum_{j\neq k,k,j\neq 1}|a_k(u)||a_j|\cos(\phi_j-phi_k)\left(2-\frac{\phi_k'+\phi_j'}{\phi_1}\right)\\
&\times e^{-\eta^2\sigma^2(1-\phi_k'/\phi_1')^2/2}e^{-\eta^2\sigma^2(1-\phi_j'/\phi_1')^2/2} \qquad \text{(A.24)}
\end{aligned}
$$

$$
\begin{aligned}
\sigma^{-2}P_2 \;=\;& -|a_1|^2-\sum_{j>1}|a_j|^2e^{-\eta^2\sigma^2(1-\phi_j'/\phi_1')^2}\\
&-2|a_1|\sum_{k>1}|a_k|\cos(\phi_1-\phi_k)e^{-\eta^2\sigma^2(1-\phi_k'/\phi_1')^2/2}\\
&-\sum_{k\neq j}|a_k||a_j|\cos(\phi_j-\phi_k)e^{-\eta^2\sigma^2(1-\phi_k'/\phi_1')^2/2}e^{-\eta^2\sigma^2(1-\phi_j'/\phi_1')^2/2}\\
&+\eta^2\sigma^2\sum_{k\neq j}|a_k||a_j|\cos(\phi_j-\phi_k)\left(1-\frac{\phi_k'}{\phi_1'}\right)\left(1-\frac{\phi_j'}{\phi_1'}\right)\\
&\times e^{-\eta^2\sigma^2(1-\phi_k'/\phi_1')^2/2}e^{-\eta^2\sigma^2(1-\phi_j'/\phi_1')^2/2}. \qquad \text{(A.25)}
\end{aligned}
$$

From the normalized scalogram expression one can obtain the equation for the instantaneous frequency at time u. The maximum of the normalized scalogram is defined from the equation:

$$x=\eta-\phi_1'(u)s=-\frac{P_1}{2P_2}. \qquad \text{(A.26)}$$

The main assumption in simplifying the expression for the scalogram is that the coefficients $\{a_j(u)\}_{j>1}$ for any u are much smaller than $a_1(u)$ and the frequencies $\phi_j'(u)$ satisfy the bandwidth condition (A.19). Retaining only significant order terms in the expansion for P_1 and P_2 allows one to write the equation for the instantaneous frequency in a simple form:

$$
\begin{aligned}
\xi(u) \;=\;& \phi_1'(u)+2\sum_{j>1}\frac{|a_j(u)|}{|a_1(u)|}\phi_j'(u)\left(\frac{\phi_1'(u)}{\phi_j'(u)}-1\right)\\
&\times\cos[\phi_1(u)-\phi_j(u)]e^{-\eta^2\sigma^2\left(1-\frac{\phi_j'(u)}{\phi_1'(u)}\right)^2/2}. \qquad \text{(A.27)}
\end{aligned}
$$

Since both the fraction $|a_j(u)|/|a_1(u)|$ and the exponential term inside the sum are small, the resulting instantaneous frequency $\xi(u)$ is a weakly modulated function around the main central frequency $\phi_1'(u)$ curve.

For a quasiperiodic signal the instantaneous frequency is itself a quasiperiodic function

[44]. In this case the expression (A.27) can be reduced to

$$\xi(u) = \omega_1 + 2\sum_{j>1} \frac{|a_j|}{|a_1|}\omega_j \left(\frac{\omega_1}{\omega_j} - 1\right) \cos(\omega_1 - \omega_j) e^{-\eta^2\sigma^2\left(1-\frac{\omega_j}{\omega_1}\right)^2/2}, \tag{A.28}$$

where $\omega_j = \phi_j'(u)$ for any time u.

REFERENCES

[1] Arnold, V. I., *Mathematical Methods of Classical Mechanics*. New York: Springer–Verlag, 1989.

[2] Komatsuzaki, T. and Berry, R. S., "Regularity in chaotic reaction path. I. Ar_6," *J. Chem. Phys.*, vol. 110, p. 9160, 1999.

[3] Li, C., Matsunaga, Y., Toda, M., and Komatsuzaki, T., "Phase-space reaction network on a multisaddle energy landspace: HCN isomerization," *J. Chem. Phys.*, vol. 123, p. 184301, 2005.

[4] Laskar, J., "A comment on 'Accurate spin axes and Solar system dynamics: Climatic variations for the Earth and Mars'," *A&A*, vol. 416, pp. 799–800, 2004.

[5] Vela-Arevalo, L. V. and Wiggins, S., "Time–frequency analysis of classical trajectories of polyatomic molecules," *Int. J. Bifurcat. Chaos*, vol. 11, pp. 1359–1380, 2001.

[6] Losada, J. C., Estebaranz, J. M., and Benito, R. M., "Local frequency analysis and the structure of classical phase space of the LiNC/LiCN molecular system," *J. Chem. Phys.*, vol. 108, pp. 63–71, 1998.

[7] Nadolski, L. and Laskar, J., "Review of single particle dynamics for a third generation light sources through frequency map analysis," *Phys. Rev. STAB*, vol. 6, p. 114801, 2003.

[8] Chandre, C., Farrelly, D., and Uzer, T., "Thresholds to chaos and ionization for the hydrogen atom in rotating fields," *Phys. Rev. A*, vol. 65, p. 053402, 2002.

[9] Froeschlé, C., Lega, E., and Gonczi, R., "Fast Lyapunov indicators. Application to asteroidal motion," *Celest. Mech. Dyn. Astron.*, vol. 67, p. 41, 1997.

[10] Liapunov, A. M., *Stability of Motion*. New York: Academic Press, 1966.

[11] Oseledec, V. I., "A multiplicative ergodic theorem: Ljapunov characteristic numbers for dynamical systems," *Trans, Moscow Math. Soc.*, vol. 19, p. 197, 1968.

[12] Carmona, R., Hwang, W. L., and Torrésani, B., *Practical Time–Frequency Analysis*. San Diego: Academic Press, 1998.

[13] Gabor, D., "Theory of communication," *J. Inst. Elec. Eng.*, vol. 903, p. 429, 1946.

[14] Mallat, S., *A Wavelet Tour of Signal Processing*. San Diego: Academic Press, 1999.

[15] Carter, D. and Brumer, P., "Intramolecular dynamics and nonlinear mechanics of model OCS," *J. Chem. Phys.*, vol. 77, p. 4208, 1982.

[16] Davis, M. J., "Bottlenecks to the intramolecular energy transfer and the calculation of relaxation rates," *J. Chem. Phys.*, vol. 83, p. 1016, 1985.

[17] Laskar, J., "Frequency analysis for multi–dimensional systems. Global dynamics and diffusion," *Physica D*, vol. 67, p. 257, 1993.

[18] Powell, G. E. and Percival, I. C., "A spectral entropy method for distinguishing regular and irregular motion of Hamiltonian systems," *J. Phys. A*, vol. 12, p. 2053, 1979.

[19] Cincotta, P. and Simó, S., "Simple tools to study global dynamics in non-axisymmetric galactic potentials," *A&AS*, vol. 147, p. 205, 2000.

[20] Bari, M. D. and Cipriani, P., "Geometry and chaos on Riemann and Finsler manifolds," *Planetary and Space Science*, vol. 46, p. 1543, 1998.

[21] Pierrehumbert, R. T., "Large–scale horizontal mixing in planetary atmospheres," *Phys. Fluids A*, vol. 3, 1991.

[22] Shadden, S. C., Lekien, F., and Marsden, J. E., "Definition and properties of Lagrangian coherent structures from finite-time Lyapunov exponents in two-dimensional aperiodic flows," *Physica D*, vol. 212, p. 271, 2005.

[23] Guzzo, M., Lega, E., and Froeschlé, C., "On the numerical detection of the effective stability of chaotic motions in quasi-integrable systems," *Physica D*, vol. 163, p. 1, 2002.

[24] c. Froeschlé, Lega, E., and Gonczi, R., "Fast Lyapunov indicators. Application to asteroidal motion," *Celest. Mech. Dyn. Astr.*, vol. 67, p. 41, 1997.

[25] Astakhov, S. A. and Farrelly, D., "Capture and escape in the elliptic restricted three–body problem," *Mon. Not. R. Astron. Soc.*, vol. 354, p. 971, 2004.

[26] Shchekinova, E., Chandre, C., Lan, Y., and Uzer, T., "Analyzing intramolecular dynamics by Fast Lyapunov Indicators," *J. Chem. Phys.*, vol. 121, p. 3471, 2004.

[27] Kolmogorov, A. N., "On the conservation of conditionally periodic motions under small perturbation of Hamiltonian," *Dokl. Akad. Nauk. SSSR*, vol. 98, p. 469, 1954.

[28] Arnold, V., "Proof of Kolmogorov's theorem on the preservation of quasi-periodic motions under small perturbation of the Hamiltonian," *Russian Math. Surv.*, vol. 18, pp. 9–36, 1963.

[29] Moser, J. K., "On invariant curves of area–preserving mappings of an annulus," *Nachr. Akad. Wiss. Gottingen, Math. Phys. Kl. II*, vol. 18, pp. 1–20, 1962.

[30] Chirikov, B. V., "A universal instability of many–dimensional oscillator systems," *Phys. Rep.*, vol. 52, p. 263, 1979.

[31] Daubechies, I., *Ten Lectures on Wavelets*. CBMS–NSF Series in Applied Mathematics, Philadelphia: SIAM, 1992.

[32] Ivanov, P. C., Rosenblum, M. G., Peng, C. K., Meitus, J., Havlin, S., Stanley, H. E., and Goldberger, A. L., "Scaling behavior of heartbeat intervals obtained by wavelet–based time–series analysis," *Nature*, vol. 383, pp. 323–327, 1996.

[33] Goupillaud, P., Grossmann, A., and Morlet, J., "Cycle–octave and related transforms in seismic signal analysis," *Geoexploration*, vol. 23, pp. 85–102, 1984.

[34] Appenzeller, P. C., Stocker, T. F., and Anklin, M., "North Atlantic oscillation dynamics recorded in Greenland ice cores," *Science*, vol. 282, pp. 446–449, 1998.

[35] Farge, M., Pellegrino, G., and Schneider, K., "Coherent vortex extraction in 3D turbulent flows using orthogonal wavelets," *Phys. Rev. Lett.*, vol. 87, p. 054501, 2001.

[36] Wei, G. W., Zhan, M., and Lai, C. H., "Tailoring wavelets for chaos control," *Phys. Rev. Lett.*, vol. 89, pp. 284103–1, 2002.

[37] Permann, D. and Hamilton, I., "Wavelet analysis of time series for the Duffing oscillator: the detection of order within chaos," *Phys. Rev. Lett.*, vol. 69, pp. 2607–2610, 1992.

[38] Schrödinger, E., "Der stetige Übergang von der Mikro- zur Makromechanik," *Naturalwiss*, vol. 14, pp. 664–666, 1926.

[39] Nekhoroshev, N. N., "An exponential estimates for the time of stability of nearly integrable Hamiltonian systems," *Russian Math. Surv.*, vol. 32, pp. 1–65, 1977.

[40] Laskar, J., "The chaotic motion of the Solar system. A numerical estimate of the size of the chaotic zones," *Icarus*, vol. 88, pp. 266–291, 1990.

[41] Laskar, J., *Hamiltonian Systems with Three or More Degrees of Freedom, NATO ASI Series.* edited by C. Simó, Dordrecht: Kluwer Academic, 1999.

[42] Laskar, J., "Large scale chaos and marginal stability in the Solar system.," in *Lecture given at Xith International Congress of Mathematical Physics*, 1994.

[43] Melita, M. D. and Brunini, A., "A possible long–lived asteroid population at the equilateral Lagrangian points of Saturn," *MNRAS*, vol. 322, p. L17, 2001.

[44] Chandre, C., Wiggins, S., and Uzer, T., "Time–frequency analysis of chaotic systems," *Physica D*, vol. 181, pp. 171–196, 2003.

[45] Delprat, D., Escudié, B., Guillemain, P., Kronland-Martinet, R., Thamitchian, P., and Torrésani, B., "Asymptotic wavelet and Gabor analysis: Extraction of instantaneous frequencies,"

[46] Truhlar, D. G., Hase, W. L., and Hynes, J. T., "Current status of transition–state theory," *J. Phys. Chem.*, vol. 87, p. 2664, 1983.

[47] Lichtenberg, A. J. and Lieberman, M. A., *Regular and Stochastic Motion.* New York: Springer–Verlag, 1983.

[48] Martens, C. C., Davis, M. J., and Ezra, G. S., "Local frequency analysis of chaotic systems in multidimensional systems : Energy transport and bottlenecks in planar OCS," *Chem. Phys. Lett.*, vol. 142, pp. 519–528, 1987.

[49] Martens, C. C. PhD dissertation, Cornell University, 1987.

[50] Vela-Arevalo, L. V. PhD dissertation, California Institute of Technology, 2002.

[51] Foord, A., Smith, J. G., and Whiffen, D. H. *Mol. Phys.*, vol. 29, p. 1685, 1975.

[52] Lan, Y. and Cvitanović, P., "Variational method for finding periodic orbits in a general flow," *Phys. Rev. E*, vol. 69, p. 016217, 2004.

[53] Koch, P. M. and van Leeuwen, K. A. H., "The importance of resonances in microwave "ionization" of excited hydrogen atoms," *Phys. Rep.*, vol. 255, pp. 289–403, 1995.

[54] Oks, E., *Plasma Spectroscopy: the Influence of Microwave and Laser Fields*, vol. 9 of *Springer Series on Atoms and Plasmas*. Berlin: Springer, 1995.

[55] Lee, E., Brunello, A. F., Cerjan, C., Uzer, T., and Farrelly, D., "From asteroids to atoms: Quantum wavepackets and the restricted three–body problem of celestial mechanics," in *Physics and Chemistry of Wave Packets* (Yeazell, J. A. and Uzer, T., eds.), pp. 95–130, New York: John Wiley, 2000.

[56] Bayfield, J. E. and Koch, P. M., "Multiphoton ionization of highly excited hydrogen atoms," *Phys. Rev. Lett.*, vol. 33, p. 258, 1974.

[57] Percival, I. C., *Atoms and Molecules in Astrophysics*. edited by T. R. Carson and M. J. Roberts, London and New York: Academic, 1972.

[58] Leopold, J. G. and Percival, I. C., "Microwave ionization and excitation of Rydberg atoms," *Phys. Rev. Lett.*, vol. 41, pp. 944–947, 1978.

[59] Richards, D., "Stark-state resonances induced by low-frequency elliptically polarized fields," *J. Phys. B: At. Mol. Opt. Phys.*, vol. 30, p. 4019, 1997.

[60] Bellermann, M. R. W., Koch, P. M., and Richards, D., "Resonant, elliptical–polarization control of microwave ionization of hydrogen atoms," *Phys. Rev. Lett.*, vol. 78, p. 3840, 1997.

[61] Landau, L. D. and Lifshitz, E. M., *Quantum Mechanics: Non-relativistic Theory*. New York, Oxford: Pergamon Press, 1965.

[62] Fu, P., Scholz, T. J., Hettema, J. M., and Gallagher, T. F., "Ionization of Rydberg atoms by a circularly polarized microwave field," *Phys. Rev. Lett.*, vol. 64, p. 511, 1990.

[63] Nauenberg, M., "Comment on 'Ionization of Rydberg atoms by a circularly polarized microwave field'," *Phys. Rev. Lett.*, vol. 64, p. 2731, 1990.

[64] Mostowski, J. and Sanchez-Mondragon, J. J., "Interaction of highly excited hydrogen atoms with a resonant oscillating field," *Opt. Commun.*, vol. 29, p. 293, 1979.

[65] Meerson, B. I., Oks, E. A., and Sasorov, P. V., "A highly excited atom in a field of intense resonant electromagnetic radiation. I. Classical motion," *J. Phys. B*, vol. 15, p. 3599, 1982.

[66] Bellermann, M. R. W., Koch, P. M., Mariani, D. R., and Richards, D., "Polarization independence of microwave "ionization" thresholds of excited hydrogen atoms near the principal resonance," *Phys. Rev. Lett.*, vol. 76, p. 892, 1996.

[67] Oks, E. and Uzer, T., "Ionization of hydrogen in elliptically polarized microwave fields," *J. Phys. B*, vol. 32, pp. 3601–3613, 1999.

[68] Griffiths, J. A. and Farrelly, D., "Ionization of Rydberg atoms by circularly and elliptically polarized microwave fields," *Phys. Rev. A*, vol. 45, p. R2678, 1992.

[69] Kappertz, P. and Nauenberg, M., "Circularly polarized microwave ionization of hydrogen," *Phys. Rev. A*, vol. 47, p. 4749, 1993.

[70] Salwen, H., "Resonance transitions in molecular beam experiments. I. General theory of transitions in a rotating magnetic field," *Phys. Rev.*, vol. 99, p. 1274, 1955.

[71] von Milczewski, J., Diercksen, G. H. F., and Uzer, T., "Computation of Arnol'd web for the hydrogen atom in crossed electric and magnetic fields," *Phys. Rev. Lett.*, vol. 76, p. 2890, 1996.

[72] Casati, G., Chirikov, B. V., Shepelyansky, D. L., and Guarneri, I., "Relevance of classical chaos in quantum mechanics: The hydrogen atom in a monochromatic field," *Phys. Rep.*, vol. 154, p. 77, 1987.

[73] Blümel, R., "Microwave ionization of hydrogen Rydberg atoms: Resonance analysis and critical fields," *Phys. Rev. A*, vol. 49, p. 4787, 1994.

[74] Howard, J. E., "Stochastic ionization of hydrogen atom in a circularly polarized microwave field," *Phys. Rev. A*, vol. 46, pp. 364–372, 1992.

[75] Jensen, R. V., "Stochastic ionization of surface–state electrons: Classical theory," *Phys. Rev. A*, vol. 30, p. 386, 1984.

[76] Leopold, J. G. and Richards, D., "The effect of a resonant electric field on a classical hydrogen atom," *J. Phys. B*, vol. 19, p. 1125, 1986.

[77] Farrelly, D. and Uzer, T., "Ionization mechanism of Rydberg atoms in a circularly polarized microwave field," *Phys. Rev. Lett.*, vol. 74, p. 1720, 1995.

[78] Sacha, K. and Zakrzewski, J., "Resonancs overlap criterion for H atom ionization by circularly polarized microwave fields," *Phys. Rev. A*, vol. 55, pp. 568–576, 1997.

[79] Brunello, A. F., Uzer, T., and Farrelly, D., "Hydrogen atom in circularly polarized microwaves: Chaotic ionization via core scattering," *Phys. Rev. A*, vol. 55, p. 3730, 1997.

[80] Lee, E., Brunello, A. F., and Farrelly, D., "Coherent states in a Rydberg atom: Classical mechanics," *Phys. Rev. A*, vol. 55, p. 2203, 1997.

[81] Hill, G. M., "Researches in the Lunar theory," *Am. J. Math.*, vol. 1, p. 5, 1878.

[82] Szebehely, V., *Theory of Orbits: The Restricted Problem of Three Bodies*. New York, London: Academic, 1967.

[83] Uzer, T., Lee, E. A., Farrelly, D., and Brunello, A. F., "Synthesis of a classical atom: Wavepacket analogues of the Trojan asteroids," *Contemporary Physics*, vol. 41, p. 1, 2000.

[84] Bialynicki-Birula, I., "Lagrange equilibrium points in celestial mechanics and nonspreading wave packets for strongly driven Rydberg electrons," *Phys. Rev. Lett.*, vol. 73, p. 1777, 1994.

[85] Brunello, A. F., Uzer, T., and Farrelly, D., "Nonstationary, nondispersive wavepackets in a Rydberg atom," *Phys. Rev. Lett.*, vol. 76, p. 2874, 1996.